Solid-boundary treatment for moment systems

by

Loc Huu Khieu

A dissertation submitted in partial fulfillment
of the requirements for the degree of
Doctor of Philosophy
(Aerospace Engineering)
in The University of Michigan
2012

Doctoral Committee:

Professor Bram van Leer, Chair
Professor Kenneth G. Powell
Assistant Professor Krzysztof J. Fidkowski
Assistant Professor Christiane Jablonowski

To my parents, Mam Khieu and Doan Bui.

To my little family, Van Luu, Little Elephant, and Big Mouse.

ACKNOWLEDGEMENTS

First and foremost, I am deeply indebted to my parents for their endless sacrifices. Their monumental support give me a chance to pursue my own dreams, of which doing doctoral study at a famous American university is one of the biggest.

With not less importance, I would also like to express my genuine appreciation of my wife's unconditional love and encouragement. She has been both mom and dad to our children for me to have total concentration on research. Her contribution to the completion of this thesis is immeasurable.

It must be mentioned that this thesis would not have existed if not for the skillful guidance and immense patience of my chairperson, Professor Bram van Leer. I owe him a great debt of gratitude, for all advices, lessons, support, and many more things.

For their valuable insights and critics, I would like to express my special thanks to other members in my committee: Professor Ken Powell, Professor Krzysztof Fidkowski, and Professor Christiane Jablonowski.

This is also a good occasion for expressing my sincere gratitude to my former mentors, Professor Tong Nguyen and Professor Nghia Le. My journey in the world of science started with their encouragement.

A special thanks to my former eccentric office-mate and comrade, Marcus Lo, for his friendship. We have so many interesting discussions about work, girlfriend(s), family, politics, and anything else popped into our minds. It must be mentioned that the idea of Kinetic Flux-Vector Splitting came from one of those seemingly-random chats.

Finally, I would like to acknowledge the important support that I have received from Vietnam Education Foundation, including full financial support for the first two years of graduate study.

TABLE OF CONTENTS

LIST OF FIGURES

Figure

LIST OF TABLES

Table

LIST OF APPENDICES

Appendix

ABSTRACT

Solid-boundary treatment for moment systems

by

Loc Huu Khieu

Chair: Bram van Leer

Hyperbolic-relaxation systems for describing fluid flow, such as Grad's 13-moment (13M) system, are an alternative to the systems generated by the Chapman-Enskog expansion, which include derivatives of increasing order. The former have a number of numerical advantages stemming from the compactness of their spatial operator. They have been demonstrated to be suited for subsonic and transonic flow.

In this dissertation we explore the solid-wall boundary conditions that have to supplement these moment systems. Starting from the boundary treatment proposed by Grad, we first remove an inconsistency in his theory that would lead to ambiguous results. We formulate two boundary conditions, 1–C and 2–C, containing one and two parameters, respectively; these are used to satisfy the non-penetration condition in 1–C and 2–C, and an additional normalization condition in 2–C. The boundary conditions are implemented in a computational code based on the 13M system.

In order to study the accuracy of the new boundary condition we also develop a benchmark code based on the Boltzmann equation with Bhatnagar–Gross–Krook collision model (BGK equation), and implement the same boundary conditions in

there. Both codes include a Finite-Volume (FV) and a Discontinuous Galerkin (DG) option (piecewise-linear discretization). These codes are used to solve three types of flow problems: low-speed Couette flow with zero difference in wall temperatures, zero-speed Couette flow with appreciable wall-temperature difference, and low-speed Poiseuille flow. The Knudsen number ranged from 0.01 to 10. For these problems, incompressible Navier–Stokes–Fourier (NSF) solutions are available for comparison (except for the temperature-driven flow); here the boundary condition used is a first- or second-order velocity-slip boundary condition.

The numerical experiments indicate that the 13M/1–C system consistently predicts a flow velocity at the wall that is closer to the BGK solution than NSF does. The 13M profiles of some quantities show a difficulty with relaxing toward the mid-channel value; the profiles are not monotone and become increasingly oscillatory with increasing Knudsen number. The use of the 1–C or 2–C condition with the 13M system makes little difference. A surprising finding is that using DG in velocity space with BGK was not superior to using FV. However, using a DG discretization in physical space is advantageous, as it removes an anomaly at the wall showing up in FV solutions due to one-sided reconstruction.

CHAPTER I

Introduction

This dissertation is another step towards our ambitious goal of "CFD by first-order PDEs." We aimed at modeling all flows, except free-molecular flow, by a system of first-order-only PDEs. It was first suggested by Grad in his seminal paper [23].

The three most basic issues of this approach are [8]:

1. *What is the appropriate system of PDEs to replace the Navier-Stokes equations?*
2. *What are the boundary conditions to be used with this system?*
3. *What numerical scheme should be used to efficiently solve the system and the accompanying boundary conditions?*

Research on the first and third issues was reported in previous theses [8, 28, 60]. Details about work on the second issue will be presented in this thesis. Numerical solutions for Couette and Poiseuille flows based on *monatomic* gas will be compared against solutions of the Boltzmann equation with Bhatnagar–Gross–Krook collision model [5] (BGK equation).

1.1 Motivation

1.1.1 Limitations of the Navier–Stokes–Fourier system in simulating rarefied gas flows

The Navier–Stokes–Fourier system, abbreviated to NSF, is one of the most widely used physical descriptions of gas flow. A great deal of time and effort has been invested in analyzing this system, both analytically and numerically. As a result, the practicality of the NSF system is quite mature.

The NSF system, however, has its limitations. In particular, it is assumed that the flow is in local equilibrium, or equivalently, the value of the Knudsen number (ratio of mean-free-path to characteristic length) is sufficiently small. Figure 1.1 shows the range of physical validity of the NSF system, with respect to the value of the Knudsen number. Around $Kn \approx 0.2$, the NSF system has to be replaced by other physical description [7].

In aerospace engineering, this situation will happen if the flow speed is in the highly supersonic or hypersonic regime. A typical example is flow around a re-entry space vehicle. The physical insufficiency of the NSF system leads to incorrect predictions of, among other quantities, heat fluxes. Due to the high speed, the temperature at the skin of this type of vehicle is extremely high, requiring adequate means of heat insulation. Therefore, accurate prediction of heat fluxes is critical to the design of space vehicles.

Another example is gas flow inside a very small device, e. g. a microelectromechanical system (or MEMS). In this type of device, the flow speed is normally not that high. However, due to the small size, the characteristic length of the flow is of the same magnitude as the mean-free-path. Thus, flow quantities change significantly while gas molecules experience very few collisions. The local-equilibrium assumption is no longer a good approximation.

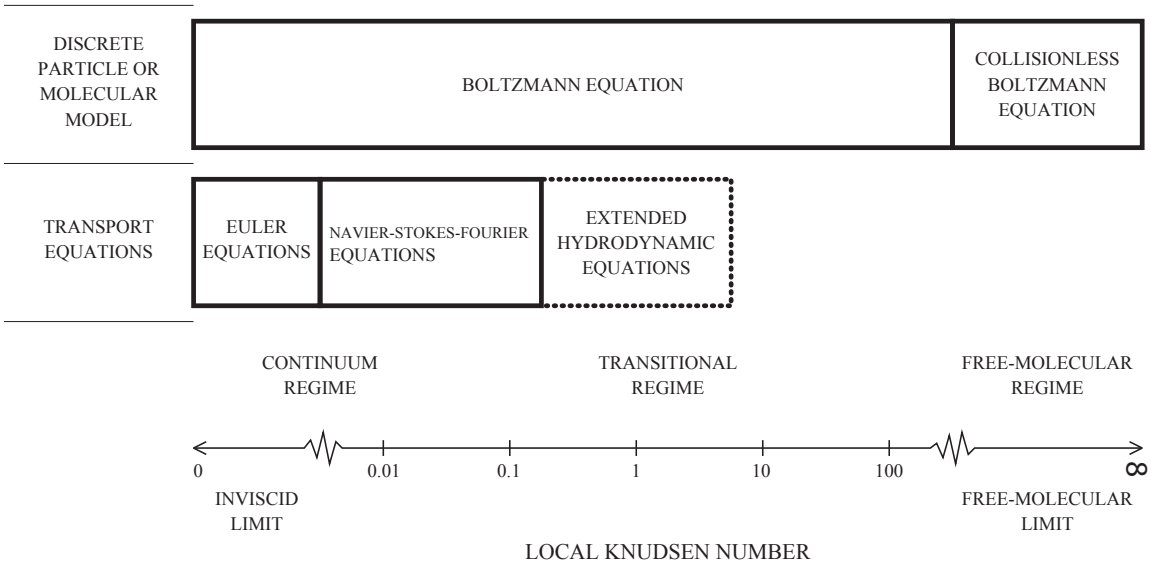

Figure 1.1: Knudsen-number limits on mathematical models, from [8, Fig. 1.2], which is a modification of Fig. 1.1 in [7].

1.1.2 Grad's moment system

Among many alternatives to the NSF system, we opt for Grad's moment system, of which a more detailed description will be presented in Chapter II. The system is derived by taking moments of the Boltzmann equation following the procedure described in [23]. Compared to the NSF system, this approach has many potential physical and numerical advantages. Regarding numerical issues: accuracy losses on arbitrarily distorted and/or adaptively refined grids can be avoided because there are no second or higher derivatives to be approximated. It has been shown in [17] that on an adaptively refined Cartesian grid the second derivatives in the NSF system prohibit achieving high accuracy and positivity combined in viscous reconstruction schemes. Furthermore, the parabolic nature of the equations requires a larger computational stencil, lowering the efficiency of parallelization, and making reconstruction at the domain boundaries more challenging. In addition, viscous terms cause the stable time-step to decrease with the square of the mesh width, which makes explicit codes inefficient. In contrast, the source terms in Grad's moment system, despite

their stiffness, are only local, allowing of compact stencils that facilitate code parallelization.

It must be mentioned that these above computational drawbacks of second-order terms in the NSF system can be alleviated to a certain degree by replacing the Finite-Volume (FV) discretization with, e. g., the Discontinuous Galerkin (DG) method. Because the DG method is currently gaining more ground, precisely because of its advantages on irregular grids and near boundaries, we have included it in our numerical experiments even though our equations do not contain second derivatives. However, there is no well-established DG approach for discretizing third or higher derivatives encountered in the Burnett and super-Burnett systems (see Section 1.1.3).

Regarding physical issues: more flow phenomena may potentially be captured owing to the larger set of independent flow variables in the system of governing equations. A typical example is that, in Grad's 13-moment system, stresses and heat fluxes are treated as independent quantities; in the NSF system, these are related back to velocity gradients and the temperature gradient by approximate constitutive equations such as the Stokes and Fourier laws.

It was shown in [60, 61] that the approach works remarkably well for subsonic and transonic flows. For higher-speed flows, however, it is unable to obtain an accurate representation of shock structures [25, p. 262][67][58, Section 6.2.3], thus rendering it unsuited for supersonic and hypersonic applications. The NSF system, despite its inaccuracy, is able to predict a smooth shock structure. At the moment, efforts are concentrated on making moment systems work up to their full potential for low-speed rarefied gas applications, in particular, flows through and around MEMS devices.

1.1.3 Other alternatives and why they are not chosen

Besides Grad's moment system, there are other approaches one could use to replace the NSF system, as shown in Fig. 1.2. The first option in *direct* approaches

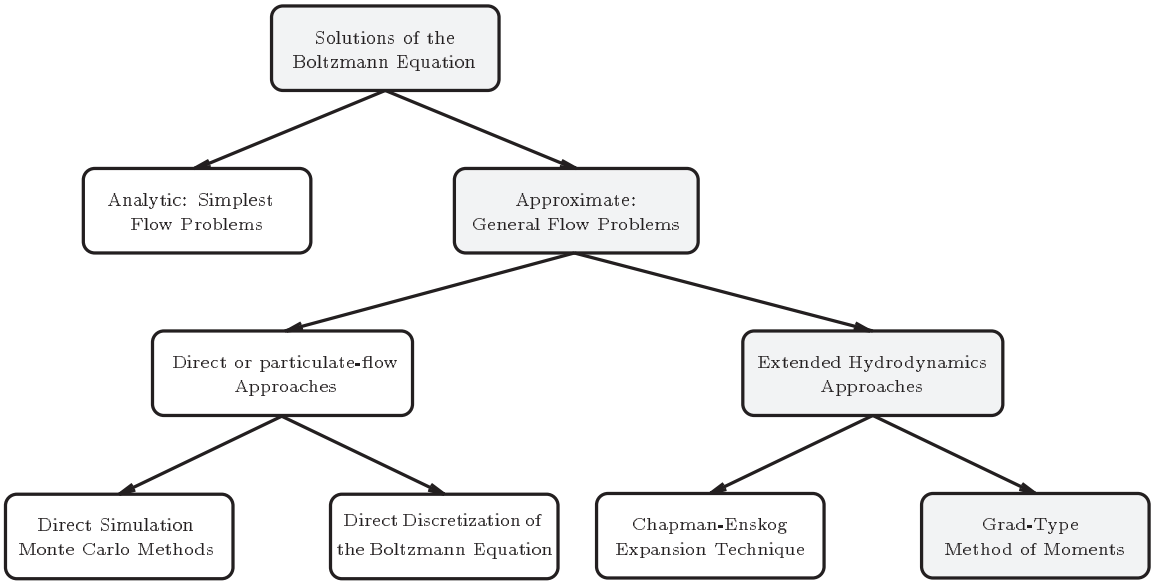

Figure 1.2: Alternatives to the NSF system, modified from Fig. 1.1 of [8].

is to use direct simulation Monte Carlo (or DSMC) particle-based simulation. This method is computationally expensive, especially in the transitional flow regime. The number of particles is quite large, in turn requiring a large amount of memory and a very long running time to achieve convergence. Due to the statistical nature of the simulation, the solutions are noisy, which asks for some kind of averaging mechanism. However, solutions from DSMC have a high degree of physical fidelity as fewer approximations are made.

The second option is to solve the Boltzmann equation numerically. This is physically as accurate as DSMC simulation, also equally computationally expensive. The Boltzmann equation is an *integro-differential* equation, in which there are only first-order derivatives. This single equation describes the evolutions in time and *phase* space of the molecular probabilistic velocity distribution function. Disregarding discretization, there is infinite amount of information about the flow status contained in the distribution function. All of the interesting gas-flow quantities are calculated as appropriate velocity moments of the distribution function. Such a powerful equation

is, understandably, extremely complex, from both the analytical and the numerical point of view. Also due to the large number of independent dimensions (seven for a time-dependent flow in three dimensions), numerical discretization of the Boltzmann equation is quite memory-intensive.

Returning to the diagram in Fig. 1.2, in *extended hydrodynamics* approaches, there is another choice besides Grad's method of moments, viz., the Chapman–Enskog expansion. This method is detailed in the seminal book by Chapman and Cowling [13]. We have chosen to avoid this approach for numerical reasons. In a nutshell, in order to account for more non-equilibrium physics, the system of PDEs is enriched with third and higher spatial derivatives. Following this procedure, one can derive the Euler system as a *zeroth-order expansion* and the Navier–Stokes system as *first-order expansion* in terms of the Knudsen number. The results of the *second-order expansion* and the *third-order expansion* are the Burnett system and super-Burnett system, respectively. Besides obvious numerical disadvantages due to the presence of third and higher spatial derivatives, these two systems also violate the entropy principle [59]. Until now, there is no evidence that Grad's moment system violates this principle.

1.2 Outline of thesis

This thesis is organized as follows. In Chapter II, we detail the derivation of Grad's moment systems from the Boltzmann equation. We first start by describing the Boltzmann equation and its collision integral. Formulation of Grad's approach is then introduced. It is used to derive the 10-moment and 13-moment system; the latter is the governing system we study in this thesis. We conclude the chapter by a discussion of moment-system limitations as well as available rectifications.

In Chapter III, the wall-boundary conditions for Grad's moment system are discussed. We show that the resulting set of boundary conditions are not consistent by applying it to the 10-moment and 13-moment systems. We study the root cause and

detail our two alternatives.

In Chapter IV, we describe the analytical Navier–Stokes–Fourier solutions for Couette and Poiseuille flows. The solid-boundary condition for the NSF system is the first-order velocity-slip condition for Couette flow, and the second-order condition in Poiseuille flow. After that, numerical methods for solving the moment system and the BGK equation are discussed. We will use both FV and DG discretizations in combination with the Runge–Kutta time integration.

In Chapter V, we present solutions for Couette and Poiseuille flows obtained from the NSF system, Grad's 13-moment system and the BGK equation.

The conclusions and suggestions for future work are shown in Chapter VI.

CHAPTER II

Grad's moment system

The Grad's moment system is derived from Maxwell's equations of transfer, which are velocity moments of the Boltzmann equation. Due to its importance as the foundation of the moment system, the Boltzmann equation is presented first in Section 2.1. Description of the systematic procedure to derive Grad's moment systems, up to arbitrary order of the moments, is shown in Section 2.2. The last section, Section 2.3, lists current limitations and their available rectifications.

2.1 The Boltzmann equation

The Boltzmann equation is the fundamental equation in the kinetic theory of gas [36]. It describes the evolution of the *velocity distribution function* in time t and *phase* space. The latter is comprised of *physical* space $\mathbf{x}$ and *velocity* space $\mathbf{v}$; in general, it has six dimensions. For a *monatomic* gas, the Boltzmann equation has following form:

$$\frac{\partial f}{\partial t} + v_j \frac{\partial f}{\partial x_j} + \frac{\partial}{\partial v_j}\left(a_j f\right) = \frac{\delta f}{\delta t}. \tag{2.1}$$

Tensor notation, or index notation, is utilized in Eq. (2.1); the three components of physical space $\mathbf{x}$ are $(x_1, x_2, x_3) \equiv (x, y, z)$, and similarly, the three components of velocity space $\mathbf{v}$ are $(v_1, v_2, v_3) \equiv (v_x, v_y, v_z)$. The function $f\left(t, \mathbf{x}, \mathbf{v}\right)$ is the velocity-distribution function, or *distribution function*, or simply just *distribution*. Further

information about this function will be presented in Section 2.1.1. The quantity a_j is the molecular acceleration due to external forces acting on the gas molecules, such as gravity. In general it may depend on the molecular velocity. In this thesis it is assumed that there is no external force in the system, $a_j = 0$. The last two terms of the left-hand-side describe the changing of f due to advection in phase space. The right-hand-side of the Boltzmann equation, $\delta f/\delta t$, is called *collision integral*. It shows how the distribution f evolves due to inter-molecular collisions. More details about the collision integral will be presented in Section 2.1.2.

It must be noted that the Boltzmann equation, despite being a satisfactory representation of a gas at the molecular level, is not the "last word." The more fundamental description is embodied in the Liouville equation, which is derived directly from the laws of mechanics [7, 66]. It has been shown that the Boltzmann equation can be obtained from the Liouville equation, under a few assumptions (see [66, Section 9.3] or [23, Section 3]):

- point molecules,
- complete collisions,
- slowly varying distribution function, and
- molecular chaos.

2.1.1 The velocity-distribution function

The velocity-distribution function is a statistical description of a gas at the molecular level [7]. The function $f(t, \mathbf{x}, \mathbf{v})\,\mathrm{d}\mathbf{v}$ is the mass density of all molecules having their velocity in the range of $\mathbf{v} \to \mathbf{v} + \mathrm{d}\mathbf{v}$ at the physical location $\mathbf{x}$ and time t. In the statistical sense, the distribution function contains information about location and velocity of all molecules in the flow at any given time. Moments in velocity space of the distribution function produce familiar average quantities that we can obtain

from experiments, such as density, average velocity, temperature, pressure, viscous stresses, etc.

From the definition it is obvious that integrating the distribution function over all possible molecular velocities produces the mass density, or density,

$$\rho\left(t,\mathbf{x}\right)=\int_{-\infty}^{+\infty}f\left(t,\mathbf{x},\mathbf{v}\right)\mathrm{d}\mathbf{v}. \tag{2.2}$$

The first-order moments of the distribution function will give us the bulk velocity of the flow:

$$u_j\left(t,\mathbf{x}\right)\equiv\begin{bmatrix}u_x\\u_y\\u_z\end{bmatrix}=\frac{1}{\rho\left(t,\mathbf{x}\right)}\int_{-\infty}^{+\infty}v_jf\left(t,\mathbf{x},\mathbf{v}\right)\mathrm{d}\mathbf{v}. \tag{2.3}$$

It is now convenient to introduce the molecular *thermal* or *peculiar* velocity $\mathbf{c}$, which is the molecular velocity in the frame-of-reference moving with the bulk velocity of the flow, $\mathbf{c}=\mathbf{v}-\mathbf{u}$. This velocity will be used interchangeably with $\mathbf{v}$ as independent variable of the distribution function. The $\mathbf{c}$-velocity-moment of the distribution function is called *central moment* to distinguish it from the $\mathbf{v}$-velocity-moment, which is simply called *moment* from now on. The first-order central moments are naught:

$$\rho\bar{c}_j=\int_{-\infty}^{+\infty}c_jf\left(t,\mathbf{x},\mathbf{v}\right)\mathrm{d}\mathbf{c}=\int_{-\infty}^{+\infty}\left(v_j-u_j\right)f\left(t,\mathbf{x},\mathbf{v}\right)\mathrm{d}\mathbf{v}=u_j-u_j=0. \tag{2.4}$$

The second-order central moments form the so-called pressure tensor:

$$P_{ij}\left(t,\mathbf{x}\right)\equiv\begin{bmatrix}P_{xx}&P_{xy}&P_{xz}\\P_{xy}&P_{yy}&P_{yz}\\P_{xz}&P_{yz}&P_{zz}\end{bmatrix}=\int_{-\infty}^{+\infty}c_ic_jf\left(t,\mathbf{x},\mathbf{c}\right)\mathrm{d}\mathbf{c}. \tag{2.5}$$

It is clear from (2.5) that the pressure tensor $\mathbf{P}$ is symmetrical. Therefore, it generally has only six independent components. Pressure p and temperature T are calculated

from components of the pressure tensor as follow

$$p = \frac{1}{3} P_{jj} = \frac{1}{3} \left(P_{xx} + P_{yy} + P_{zz} \right), \tag{2.6}$$

$$T = \frac{p}{\rho R}, \tag{2.7}$$

where R is the specific gas constant. There are many situations in which it is convenient to use, in stead of P_{ij}, the *traceless* tensor

$$p_{ij} = P_{ij} - p\delta_{ij} \tag{2.8}$$

where δ_{ij} is the Kronecker delta. This tensor is the opposite of the familiar viscous stress tensor τ_{ij}, $\tau_{ij} = -p_{ij}$. In the NSF system it is approximated by [69, Section 2-4]:

$$\tau_{ij} = \mu \left(\frac{\partial u_i}{\partial x_j} + \frac{\partial u_j}{\partial x_i} \right) + \left(\lambda \nabla \cdot \mathbf{u} \right) \delta_{ij}, \tag{2.9}$$

μ is the *viscosity* of the gas, and λ is the *second coefficient of viscosity*.

Third-order central moments form a three-dimensional symmetrical tensor, which generally has ten independent components,

$$S_{ijk} \left(t, \mathbf{x} \right) = \int_{-\infty}^{+\infty} c_i c_j c_k \, f \left(t, \mathbf{x}, \mathbf{c} \right) \mathrm{d}\mathbf{c}. \tag{2.10}$$

The familiar heat fluxes are calculated from traces of S_{ijk} in each dimension

$$q_j \equiv \begin{bmatrix} q_x \\ q_y \\ q_z \end{bmatrix} = \frac{1}{2} S_{jkk} = \frac{1}{2} \left(S_{jxx} + S_{jyy} + S_{jzz} \right). \tag{2.11}$$

It is approximately calculated from the gradient of temperature by Fourier's law in

the NSF system [69, Section 2-5]

$$q_j = -k\frac{\partial T}{\partial x_j}, \tag{2.12}$$

where k is the *coefficient of thermal conductivity*. Equations (2.9) and (2.12) are also called *constitutive equations*.

The highest-order central moments of the distribution function that will appear in this thesis are fourth-order ones. They are the components of a four-dimensional tensor, which generally has fifteen independent members, also due to symmetry:

$$Q_{ijkl}\left(t, \mathbf{x}\right) = \int_{-\infty}^{+\infty} c_i c_j c_k c_l \, f\left(t, \mathbf{x}, \mathbf{c}\right) \mathrm{d}\mathbf{c}. \tag{2.13}$$

2.1.2 Collision integral

Assume that we limit ourselves to *elastic collisions* between pairs of electrically neutral molecules, meaning that there will be no energy exchange; then the collision integral takes the following form [66]:

$$\frac{\delta f}{\delta t} = \frac{1}{m}\int_{-\infty}^{+\infty}\int_{0}^{4\pi}\left[f\left(\mathbf{v}'\right) f\left(\boldsymbol{\zeta}'\right) - f\left(\mathbf{v}\right) f\left(\boldsymbol{\zeta}\right)\right] g\sigma \, \mathrm{d}\Omega \, \mathrm{d}\boldsymbol{\zeta}; \tag{2.14}$$

where

- m is mass per molecule,
- $\mathbf{v}, \boldsymbol{\zeta}$ and $\mathbf{v}', \boldsymbol{\zeta}'$ are velocities of two colliding molecules before and after an intermolecular collision, respectively,
- g is the relative speed, given by $|\boldsymbol{\zeta} - \mathbf{v}|$,
- $\mathrm{d}\Omega$ is the differential solid angle, and
- $\sigma\left(g, \chi\right)$ is the *collision cross-section* representing the probability that a collision

with relative speed g will result in a deflection angle χ.

For an in-depth derivation and analysis of the collision integral, the reader may consult material presented in many gas-kinetic books, such as [36, 66] or the comprehensive book dedicated to the Boltzmann equation by Cercignani [12].

Equation (2.14) shows that the Boltzmann equation is a complicated *nonlinear integro-differential* equation. Its mathematical complexity is largely due to the nonlinear nature of the collision integral term [66, Section 10.2]. Thus it is desirable to substitute the latter by mathematically simpler approximations. These approximated models have to preserve many qualitative features of the true collision integral, such as:

- the equilibrium solution is the Maxwellian distribution function,

$$f_{\mathrm{M}}(t, \mathbf{x}, \mathbf{v}) = \frac{\rho}{(2\pi RT)^{3/2}} \exp\left[-\frac{(\mathbf{v}-\mathbf{u})^2}{2RT}\right], \tag{2.15}$$

- all *collisional invariants* are preserved:

$$\int_{-\infty}^{+\infty} \begin{bmatrix} 1 \\ v_j \\ \frac{1}{2}v^2 \end{bmatrix} \frac{\delta f}{\delta t}\, \mathrm{d}\mathbf{v} = 0. \tag{2.16}$$

One of the most popular collision-integral models is the B–G–K (BGK) model, named after Bhatnagar, Gross, and Krook [5]. In this model, the Boltzmann collision integral is approximated by relaxation of an initially nonequilibrium distribution function toward the equilibrium Maxwellian distribution:

$$\frac{\delta f}{\delta t} = -\frac{f - f_{\mathrm{M}}}{\tau}, \tag{2.17}$$

where the *relaxation time* τ is calculated from pressure and viscosity, $\tau = \mu/p$. The kinetic equation, resulting from inserting Eq. (2.17) into Eq. (2.1), is variously called the Krook equation, the "Krooked" Boltzmann equation, the model equation, or the BGK equation; the latter name is used in this writing. The BGK equation, despite being mathematically simpler, is still a *nonlinear integro-differential* equation. The reason is that the equilibrium distribution f_{M} needs information about local density, bulk velocity, and temperature as shown in Eq. (2.15). These are obtained from integrating the nonequilibrium distribution function f as shown in Eqs. (2.2), (2.3) and (2.7).

The BGK model has a serious limitation, among other ones, regarding simulating the correct value of the Prandtl number. For a monatomic gas the BGK equation shows $Pr = 1$ [12, 58, 66], while experimental measurements and analysis of the Boltzmann equation produce $Pr \approx \frac{2}{3}$. To account for a non-unity value of the Prandtl number, the BGK model has to be replaced by Prandtl-correction models. They still belong to the *relaxation-approximation*-type collisional models, just like BGK model. Three typical models are listed below:

- Model with two relaxation time-scales by Levermore [38, 8]

$$\frac{\delta f}{\delta t} = -\left(\frac{f - f_{\mathrm{M}}}{\tau} + \frac{f - f_{\mathrm{G}}}{\tau'}\right) = -\left[\frac{f - f_{\mathrm{M}}}{\tau} + (Pr - 1)\,\frac{f - f_{\mathrm{G}}}{\tau}\right], \tag{2.18}$$

  where f_{G} is the Gaussian distribution function

$$f_{\mathrm{G}}\,(t, \mathbf{x}, \mathbf{c}) = \frac{\rho}{(2\pi)^{3/2}\,\Delta^{1/2}} \exp\left[-\frac{1}{2}\,\mathbf{c}^{\mathrm{T}} \cdot \left(\frac{\mathbf{P}}{\rho}\right)^{-1} \cdot \mathbf{c}\right],\ \Delta = \left|\frac{\mathbf{P}}{\rho}\right|; \tag{2.19}$$

- *Ellipsoidal–Statistical* BGK model, or ES–BGK, by Holway [30]:

$$\frac{\delta f}{\delta t} = -\frac{f - f_{\mathrm{ES}}}{\tau/Pr}, \tag{2.20}$$

f_{ES} is similar to the Gaussian distribution (2.19), except that the pressure tensor $\mathbf{P}$ is replaced by ($\mathbf{I}$ is identity matrix)

$$\frac{p}{Pr}\mathbf{I} + \left(1 - \frac{1}{Pr}\right)\mathbf{P}; \tag{2.21}$$

- Shakov model [53], given by

$$\frac{\delta f}{\delta t} = -\frac{f - f_{\mathrm{S}}}{\tau} \tag{2.22}$$

with

$$f_{\mathrm{S}}\left(t, \mathbf{x}, \mathbf{c}\right) = f_{\mathrm{M}}\left[1 + \left(1 - Pr\right)\frac{q_j c_j}{pRT}\left(\frac{c^2}{5RT} - 1\right)\right]. \tag{2.23}$$

It should be noted that, when $\mathrm{Pr} = 1$, all three Prandtl-correction models are identical to the BGK model, as expected.

2.1.3 Maxwell's equations of transfer

It is extremely challenging to solve the Boltzmann equation, both analytically and numerically. Exact solutions are scant, even for relatively simple physical situations [66, Chapter X]. Mathematically speaking, the Boltzmann equation is complex due to being a nonlinear integro-differential equation, even when simpler models are used to approximate the collision integral. Numerically speaking, the addition of velocity space to the set of independent variables makes the grid orders of magnitude larger than one required for normal continuum gas-dynamics calculations, such as for solving the NSF system. Numerical simulations become highly expensive, requiring a large amount of memory and a long running time. Physically speaking, the description in the Boltzmann equation is unnecessarily complete. It has only one unknown, the distribution function f, but it contains everything we would ever want to know about the gas flow. For practical purposes, however, our interest lies only in a few averaged

quantities. Thus, it is desirable to reduce the microscopic description to a more manageable level; see [36, Chapter III] and [66, Chapter X] for a comprehensive list of available options.

One option is to replace the single Boltzmann equation by a *system* of partial differential equations (PDEs). The new unknowns are a set of familiar macroscopic quantities, introduced in Section 2.1.1. Their governing equations are derived from Maxwell's equations of transfer, which are obtained by taking velocity moments of the Boltzmann equation. The conservative form is derived by multiplying (2.1) (without acceleration terms, $a_j = 0$) with a weight $\mathbf{W}(\mathbf{v})$, then integrating over all possible values of molecular velocity. Because molecular velocity $\mathbf{v}$ is independent of time t and physical space $\mathbf{x}$, we can bring the temporal and spatial derivatives out of the integrals to obtain the following expression:

$$\frac{\partial}{\partial t}\int_{-\infty}^{+\infty}\mathbf{W}f\,\mathrm{d}\mathbf{v}+\frac{\partial}{\partial x_j}\int_{-\infty}^{+\infty}v_j\mathbf{W}f\,\mathrm{d}\mathbf{v}=\int_{-\infty}^{+\infty}\mathbf{W}\frac{\delta f}{\delta t}\,\mathrm{d}\mathbf{v}. \tag{2.24}$$

The system (2.24) is equivalent to the Boltzmann equation only if the weight vector $\mathbf{W}(\mathbf{v})$ is infinitely large, i. e. the dependent variables are an infinite set of macroscopic quantities.

To compute the source term $\int \mathbf{W}\,(\delta f/\delta t)\,\mathrm{d}\mathbf{v}$ without knowledge of the distribution function, we have to choose one of following options: ***a)*** using the BGK collision model; ***b)*** using a Prandtl-correction model, such as the three models mentioned in Section 2.1.2; and ***c)*** assuming a gas of Maxwell molecules, see [58, section 5.3] for details about that calculation.

The system derived from Eq. (2.24), however, is not closed, due to the flux-terms. Considering the order of $\mathbf{v}$-velocity polynomials in the system, the value in the flux-terms (factor $v_j\mathbf{W}(\mathbf{v})$) is always one higher than the value in the temporal derivative (factor$\mathbf{W}\,(\mathbf{v})$). As a result there are quantities in the flux-terms that are not in the

temporal derivatives. For example, if we derive a governing system for the evolution of only density and momentums, the weight vector is $\mathbf{W}(\mathbf{v}) = [1, v_x, v_y, v_z]$ and the LHS of Eq. (2.24) becomes

$$\frac{\partial}{\partial t}\int_{-\infty}^{+\infty}\begin{bmatrix}1\\ v_i\end{bmatrix} f\,\mathrm{d}\mathbf{v} + \frac{\partial}{\partial x_j}\int_{-\infty}^{+\infty} v_j\begin{bmatrix}1\\ v_i\end{bmatrix} f\,\mathrm{d}\mathbf{v} = \frac{\partial}{\partial t}\begin{bmatrix}\rho\\ \rho u_i\end{bmatrix} + \frac{\partial}{\partial x_j}\begin{bmatrix}\rho u_j\\ \rho u_i u_j + P_{ij}\end{bmatrix}.$$

The flux-terms contain the second-order central moments, P_{ij}, while the temporal derivatives include no higher than first-order moments, u_i. It is necessary to relate P_{ij} to ρ and u_i to achieve closure for the system.

To derive closure for (2.24), it is necessary to establish the dependence of f on the macroscopic quantities in the temporal derivative. There are two approaches to representing the distribution function in terms of macroscopic quantities and the molecular velocity $\mathbf{v}$, or molecular thermal velocity $\mathbf{c}$: ***a)*** Grad's approach [23] and ***b)*** the Chapman–Enskog expansion [13]. In this thesis we follow the Grad's approach.

2.2 Derivation of Grad's moment systems

Following Grad [23], the nonequilibrium distribution function f is a perturbation of the Maxwellian distribution (2.15), using Hermite polynomials H in the component of $\mathbf{c}$,

$$f = f_{\mathrm{M}}\left[a^{(0)}H^{(0)} + a_j^{(1)}H_j^{(1)} + \frac{1}{2!}a_{ij}^{(2)}H_{ij}^{(2)} + \frac{1}{3!}a_{ijk}^{(3)}H_{ijk}^{(3)} + \cdots\right]. \tag{2.25}$$

The number of terms in the perturbation depends on the number of moments of f one would like to simulate. Table 2.1 shows various options for moment systems including up to 35 moments, i.e., up to all 4^{th}-order central moments. The Hermite polynomials

H have the following forms [24]:

$$
\begin{aligned}
H^{(0)} &= 1, \\
H_j^{(1)} &= \frac{c_j}{\sqrt{RT}}, \\
H_{ij}^{(2)} &= \frac{c_i c_j}{RT} - \delta_{ij}, \\
H_{ijk}^{(3)} &= \frac{c_i c_j c_k}{(RT)^{3/2}} - \frac{c_i \delta_{jk} + c_j \delta_{ik} + c_k \delta_{ij}}{\sqrt{RT}}, \\
H_{ijkl}^{(4)} &= \frac{c_i c_j c_k c_l}{(RT)^2} - \frac{c_i c_j \delta_{kl} + c_i c_k \delta_{jl} + c_i c_l \delta_{jk} + c_j c_k \delta_{il} + c_j c_l \delta_{ik} + c_k c_l \delta_{ij}}{RT} \\
&\qquad + \left(\delta_{ij}\delta_{kl} + \delta_{ik}\delta_{jl} + \delta_{il}\delta_{jk}\right), \\
&\dots
\end{aligned}
\tag{2.26}
$$

where δ is Dirac's delta function; they are *orthogonal* with respect to the Maxwellian distribution, i. e.,

$$
\int_{-\infty}^{+\infty} H_{ij}^{(\alpha)} H_{kl}^{(\beta)} f_{\mathrm{M}} \, \mathrm{d}\mathbf{c} = 0 \text{ unless } H_{ij}^{(\alpha)} = H_{kl}^{(\beta)};
$$

Note that indices (i, j, k, l) in Eq. (2.26) each can take the values 1, 2, and 3. Values of the unknown coefficients a in Eq. (2.25) are determined based on central moments:

$$
\int_{-\infty}^{+\infty} \begin{bmatrix} H^{(0)} \\ H_j^{(1)} \\ H_{ij}^{(2)} \\ H_{ijk}^{(3)} \end{bmatrix} f \, \mathrm{d}\mathbf{c} = \begin{bmatrix} \rho \\ 0 \\ p_{ij}/RT \\ S_{ijk}/\left(RT\right)^{3/2} \end{bmatrix}
\tag{2.27}
$$

The first member in the hierarchy is a trivial case, in which Eq. (2.24) will be the Maxwellian distribution function. The obtained 5–moment system is the familiar Euler system of compressible gas dynamics. Detailed derivation of the 10–moment and 13–moment systems will be presented next; the latter one is the main system

Table 2.1: The Grad's moment hierarchy (up to 4^{th}-order moment)

No. moments	Primitive var.	$\mathbf{W}(\mathbf{v})$	$H^{(\alpha)}$
5	$[\rho, u_i, p]$	$\left[1, v_i, \frac{1}{2}v^2\right]$ [a]	$\left[H^{(0)}, H_i^{(1)}, H_{jj}^{(2)}\right]$
10	$[\rho, u_i, P_{ij}]$	$[1, v_i, v_i v_j]$	$\left[H^{(0)} \rightarrow H_{ij}^{(2)}\right]$
13	$[\rho, u_i, P_{ij}, q_i]$	$[1 \rightarrow v_i v_j, v_i v^2]$	$\left[H^{(0)} \rightarrow H_{ij}^{(2)}, H_{ijj}^{(3)}\right]$
20	$[\rho, u_i, P_{ij}, S_{ijk}]$	$[1 \rightarrow v_i v_j v_k]$	$\left[H^{(0)} \rightarrow H_{ijk}^{(3)}\right]$
26	$[\rho, u_i, P_{ij}, S_{ijk}, Q_{ij}]$	$[1 \rightarrow v_i v_j v_k, v_i v_j v^2]$	$\left[H^{(0)} \rightarrow H_{ijk}^{(3)}, H_{ijkk}^{(4)}\right]$
35	$[\rho, u_i, P_{ij}, S_{ijk}, Q_{ijkl}]$	$[1 \rightarrow v_i v_j v_k v_l]$ [b]	$\left[H^{(0)} \rightarrow H_{ijkl}^{(4)}\right]$ [c]
		...	

[a] $v^2 = \mathbf{v} \cdot \mathbf{v} = v_x^2 + v_y^2 + v_z^2$
[b] $[1 \rightarrow v_i v_j v_k v_l]$ implies $[1, v_i, v_i v_j, v_i v_j v_k, v_i v_j v_k v_l]$.
[c] $\left[H^{(0)} \rightarrow H_{ijkl}^{(4)}\right]$ implies $\left[H^{(0)}, H_i^{(1)}, H_{ij}^{(2)}, H_{ijk}^{(3)}, H_{ijkl}^{(4)}\right]$.

used in the numerical simulations of this thesis.

2.2.1 10–moment (10M) system

The 10–moment system simulates the evolution of ten macroscopic quantities: density ρ, average velocity vector u_j, and pressure tensor P_{ij}. It is a system of ten first-order PDEs, derived from (2.24) with $\mathbf{W}(\mathbf{v}) = [1, v_j, v_i v_j]$. All options to compute the source terms, mentioned in Section 2.1.2, produce the same results. The system, expressed in conservation form with tensor notation, is given as

$$\frac{\partial}{\partial t}\begin{bmatrix} \rho \\ \rho u_j \\ \rho u_i u_j + P_{ij} \end{bmatrix} + \frac{\partial}{\partial x_\alpha}\begin{bmatrix} \rho u_\alpha \\ \rho u_j u_\alpha + P_{j\alpha} \\ \rho u_i u_j u_\alpha + (u_i P_{j\alpha} + u_j P_{i\alpha} + u_\alpha P_{ij}) \end{bmatrix} = -\frac{1}{\tau}\begin{bmatrix} 0 \\ 0 \\ p_{ij} \end{bmatrix}. \quad (2.28)$$

This system illustrates one important property of the moment approach: it is possible to have the same set of closures, $S_{ijk} = 0$ in this case, but multiple forms of the distribution function f. The first option is to use Eq. (2.25), without the term $H^{(3)}_{ijk}$. Values of a are calculated from Eq. (2.27), yielding

$$\textit{Grad10M distribution: } f^{10}_{\text{Grad}} = f_{\text{M}} \left(1 + \frac{p_{ij}}{2pRT} c_i c_j \right) . \tag{2.29}$$

Due to the perturbation nature, there is no guarantee that f^{10}_{Grad} will always be non-negative and finite. The second option is to use the Gaussian distribution (2.19); which is not a perturbation but rather a generalization of the Maxwellian distribution. Just as Eq. (2.29), this distribution function has no nonzero third-order central moments, $S_{ijk} = 0$. Levermore [38] has proved that, with physically realistic values of density and pressure tensor, f_{G} will stay non-negative and finite.

We repeat that, the source term in Eq. (2.28) comes out the same. This is expected as neither 10M system can simulate the heat fluxes. Despite this shortcoming, it is still an attractive system for research purposes. The system is mathematically simpler than, e.g., Grad's 13-moment system, and physically adequate for flows with insignificant heat conduction, such as isothermal flows.

2.2.2 13–moment (13M) system

A physically meaningful and sufficient description of the flow, at the macroscopic level, involves thirteen quantities: the density ρ (1 var), the vector of bulk velocities u_j (3 vars.), the pressure tensor P_{ij} (6 vars.), and the vector of heat fluxes q_j (3 vars.). Since $q_j = S_{jkk}/2$ (Eq. (2.11)), the third-order Hermite terms in Eq. (2.25)

are simplified accordingly:

$$H^{(3)}_{ijk} \to H^{(3)}_{j} \equiv H^{(3)}_{jkk} = \frac{c_j}{\sqrt{RT}}\left(\frac{\mathbf{c}^2}{RT} - 5\right)$$
$$\Rightarrow f^{13}_{\text{Grad}} = f_{\text{M}}\left[a^{(0)}H^{(0)} + a^{(1)}_j H^{(1)}_j + \frac{1}{2!}a^{(2)}_{ij}H^{(2)}_{ij} + a^{(3)}_j H^{(3)}_j\right].$$

Condition (2.27) is used to calculate $a^{(0)}$ to $a^{(2)}$; values of $a^{(3)}_j$ are calculated from the revised condition $\int_{-\infty}^{+\infty} H^{(3)}_j f^{13}_{\text{Grad}}\,\mathrm{d}\mathbf{c} = 2q_j/(RT)^{3/2}$. Then, the distribution function has its final form:

$$\textit{Grad13M distribution: } f_{\text{Grad13M}} = f_{\text{M}}\left[1 + \frac{p_{ij}}{2pRT}c_i c_j + \frac{q_k c_k}{pRT}\left(\frac{\mathbf{c}^2}{5RT} - 1\right)\right]. \quad (2.30)$$

The following closures are obtained using Eqs. (2.10) and (2.13):

$$S_{ijk} = \frac{2}{5}\left(q_i\delta_{jk} + q_j\delta_{ik} + q_k\delta_{ij}\right), \quad (2.31)$$
$$Q_{ij} \equiv Q_{ijkk} = RT\left(7P_{ij} - 2p\delta_{ij}\right). \quad (2.32)$$

The 13M system for three-dimensional physical space is derived from (2.24), using $\mathbf{W}(\mathbf{v}) = [1, v_j, v_i v_j, v_j v^2]$. It is expressed in conservation form, with index notation, as

$$\frac{\partial}{\partial t}\begin{bmatrix}\rho\\ \rho u_j\\ \rho u_i u_j + P_{ij}\\ \rho u_j u^2 + 3u_j\, p + 2u_k P_{jk} + 2q_j\end{bmatrix} + \frac{\partial}{\partial x_\alpha}\left(\mathbf{F}^{(\alpha)}\right) = -\frac{1}{\tau}\begin{bmatrix}0\\ 0\\ p_{ij}\\ 2u_k\, p_{jk} + 2\,\mathrm{Pr}\, q_j\end{bmatrix}, \quad (2.33)$$

where the flux-functions are:

$$\mathbf{F}^{(\alpha)} = \begin{bmatrix} \rho u_\alpha \\ \rho u_j u_\alpha + P_{j\alpha} \\ \rho u_i u_j u_\alpha + (u_i P_{j\alpha} + u_j P_{i\alpha} + u_\alpha P_{ij}) + S_{ij\alpha} \\ \rho u_j u_\alpha u^2 + \left(3u_j u_\alpha p + u^2 P_{j\alpha} + 2u_j u_k P_{k\alpha} + 2u_k u_\alpha P_{jk}\right) \\ \qquad + (2u_j q_\alpha + 2u_\alpha q_j + 2u_k S_{jk\alpha}) + Q_{j\alpha} \end{bmatrix}.$$

The relaxation time τ depends implicitly on both $\mathbf{x}$ and time t

$$\tau = \frac{\mu}{p}. \tag{2.34}$$

It is surprising that the expressions for the source terms in Eq. (2.33) are the same, regardless of any Prandtl-correction model is used or these are direct computation assuming a Maxwell gas molecule. Using the BGK model for the collision integral is equivalent to setting $Pr = 1$ in Eq. (2.33).

In two-dimensional flows, which are the main focus of this thesis, the number of variables reduces from thirteen to nine. The primitive variables are

$$\mathbf{V} = [\rho, u_x, u_y, P_{xx}, P_{yy}, P_{zz}, P_{xy}, q_x, q_y]\,. \tag{2.35}$$

Equation (2.33) reduces to a system of first-order conservation laws of the form

$$\frac{\partial \mathbf{U}}{\partial t} + \frac{\partial \mathbf{F}}{\partial x} + \frac{\partial \mathbf{G}}{\partial y} = -\frac{1}{\tau}\mathbf{S}; \tag{2.36}$$

here the vector of conserved variables $\mathbf{U}$ and source terms $\mathbf{S}$ are

$$\mathbf{U} = \begin{bmatrix} \rho \\ \rho u_x \\ \rho u_y \\ \rho u_x^2 + P_{xx} \\ \rho u_y^2 + P_{yy} \\ P_{zz} \\ \rho u_x u_y + P_{xy} \\ \rho u_x u^2 + 3u_x p + 2u_x P_{xx} + 2u_y P_{xy} + 2q_x \\ \rho u_y u^2 + 3u_y p + 2u_x P_{xy} + 2u_y P_{yy} + 2q_y \end{bmatrix}, \quad \mathbf{S} = \begin{bmatrix} 0 \\ 0 \\ 0 \\ p_{xx} \\ p_{yy} \\ p_{zz} \\ p_{xy} \\ 2u_x p_{xx} + 2u_y p_{xy} + 2\mathrm{Pr} q_x \\ 2u_x p_{xy} + 2u_y p_{yy} + 2\mathrm{Pr} q_y \end{bmatrix};$$

the vector of x-fluxes are given by

$$\mathbf{F} = \begin{bmatrix} \rho u_x \\ \rho u_x^2 + P_{xx} \\ \rho u_x u_y + P_{xy} \\ \rho u_x^3 + 3u_x P_{xx} + \frac{6}{5} q_x \\ \rho u_x u_y^2 + u_x P_{yy} + 2u_y P_{xy} + \frac{2}{5} q_x \\ u_x P_{zz} + \frac{2}{5} q_x \\ \rho u_x^2 u_y + 2u_x P_{xy} + u_y P_{xx} + \frac{2}{5} q_y \\ \rho u_x^2 u^2 + \left(4u_x^2 P_{xx} + 4u_x u_y P_{xy} + 3u_x^2 p + u^2 P_{xx}\right) + \frac{4}{5}\left(8u_x q_x + u_y q_y\right) \\ \qquad + RT\left(7P_{xx} - 2p\right) \\ \rho u_x u_y u^2 + \left[2u_x u_y \left(P_{xx} + P_{yy}\right) + 3u_x u_y p + 3u^2 P_{xy}\right] + \frac{14}{5}\left(u_x q_y + u_y q_x\right) \\ \qquad + 7P_{xy} RT \end{bmatrix};$$

and the vector of y-fluxes by

$$\mathbf{G} = \begin{bmatrix} \rho u_y \\ \rho u_x u_y + P_{xy} \\ \rho u_y^2 + P_{yy} \\ \rho u_x^2 u_y + 2u_x P_{xy} + u_y P_{xx} + \frac{2}{5} q_y \\ \rho u_y^3 + 3u_y P_{yy} + \frac{6}{5} q_y \\ u_y P_{zz} + \frac{2}{5} q_y \\ \rho u_x u_y^2 + u_x P_{yy} + 2u_y P_{xy} + \frac{2}{5} q_x \\ \rho u_x u_y u^2 + \left[2u_x u_y \left(P_{xx} + P_{yy}\right) + 3u_x u_y p + 3u^2 P_{xy}\right] + \frac{14}{5}\left(u_x q_y + u_y q_x\right) \\ \qquad + 7P_{xy} RT \\ \rho u_y^2 u^2 + \left(4u_y^2 P_{yy} + 4u_x u_y P_{xy} + 3u_y^2 p + u^2 P_{yy}\right) + \frac{4}{5}\left(u_x q_x + 8u_y q_y\right) \\ \qquad + RT\left(7P_{yy} - 2p\right) \end{bmatrix}.$$

2.3 Limitations and modifications to Grad's moment systems

2.3.1 Adjustment for diatomic gas

The Grad's 13–moment system (2.33) is only applicable to *monatomic* gas, due to the same limitation on the Boltzmann equation (2.1). Since air is a mixture of, predominantly, diatomic gases (oxygen and nitrogen), it is necessary to modify the moment system for aerodynamic applications. Hittinger presented one such adjustment to the 10M system in his Ph.D. thesis [28]. (It will not be used in this thesis as our working fluid is the monatomic Argon gas.) To account for the rotational degrees of freedom, the collision terms are modified, and there is one additional equation governing the evolution of rotational energy. This modification is restricted to a moderate temperature range, about 200K to 600K, so that vibrational degrees of freedom can be safely ignored.

The first four equations are identical to those in Eq. (2.28). The next six equations

have identical LHSs, while the source terms are changed to

$$-\frac{3P_{ij}-P_{kk}\delta_{ij}}{3\tau_{\text{tran}}}-\frac{2\left(P_{kk}-3E_{\text{rot}}\right)}{15\tau_{\text{rot}}}\delta_{ij}.$$

The extra equation for the rotational energy E_{rot} is given as

$$\frac{\partial E_{\text{rot}}}{\partial t}+\frac{\partial\left(u_\alpha E_{\text{rot}}\right)}{\partial x_\alpha}=-\frac{3E_{\text{rot}}-P_{kk}}{5\tau_{\text{rot}}}.$$

The translational and rotational relaxation times are calculated from

$$\begin{aligned}\tau_{\text{trans}}&=\frac{\mu}{p}\\ \tau_{\text{rot}}&=\frac{15}{4p}\left(\lambda+\frac{2}{3}\mu\right);\end{aligned}$$

for diatomic gas the pressure is $p=\left(P_{jj}+E_{\text{rot}}\right)/5$. Generally, $\tau_{\text{rot}}\geq\tau_{\text{trans}}$ (rotational energy relaxes to equilibrium more slowly than translational energy), but these relaxation times are still of the same order of magnitude [28, p. 123].

2.3.2 The "embedded" inviscid shock problem

When examined at a length scale in the order of the mean free path, a normal shock is not a discontinuity connecting pre-shock state to post-shock state as depicted in solutions of the Euler system. Both experimental and numerical observations show that the structure of any macroscopic quantity in a normal shock is a smooth transition between two states, at any Mach number. We refer to [2, 52] for experimental data on (monatomic) argon; for numerical solutions from DSMC simulations, see chapter 12 in Bird's book [7] and his paper [6] for very strong shock waves with Mach numbers as large as 100. Solutions of the BGK equation are also smooth transitions [39].

Due to its hyperbolic nature, a moment system produces a shock structure in which a discontinuity similar to an inviscid shock appears, when the Mach number

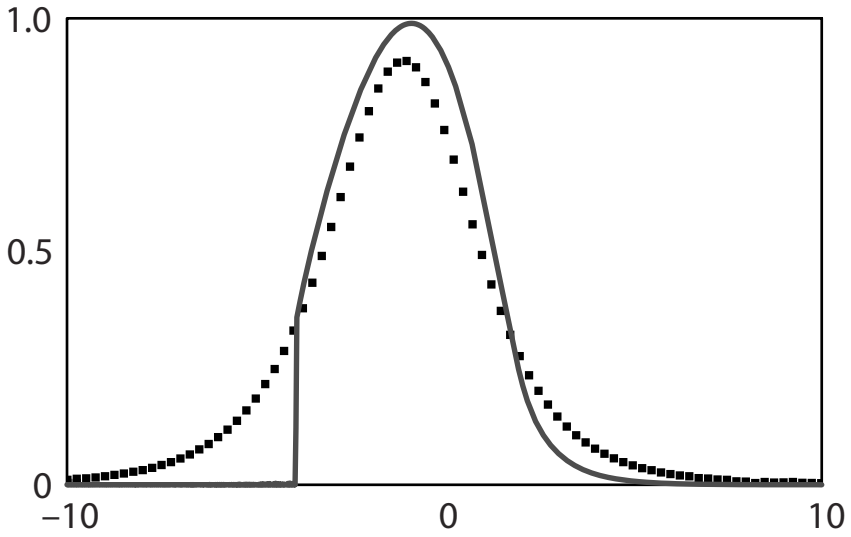

Figure 2.1: Shock structure for 13M system of *normalized* heat flux q_x at $M = 2$, using Maxwell gas molecules, presented in [64]. The solid line is the 13M solution; the symbols are the DSMC solution. The 13M's solution exhibits a discontinuity at the pre-shock state, followed by a smooth relaxation to the post-shock state.

is larger than a critical limit. This limit is $3/\sqrt{5} \approx 1.34$ for the 10M system [8, Chapter 10], while it is approximately 1.65 for the 13M system [25][58, Chapter 6]. A typical example, obtained with the 13M system, is presented in Fig. 2.1, taken from [64]. It is this inability to represent continuous shock structures, for which Grad-type moment systems are most criticized. It restricts the Grad-type moment system to only subsonic and transonic flows.

The first option to rectify the embedded inviscid shock is to increase the number of moments in the system in order to capture more of the physics described by the Boltzmann equation, thus raising the critical Mach number. However, Holway [29] and Ruggeri [49] casted doubt on this approach. Their argument was that there is an absolute upper bound for the value of the critical Mach number, which is ≈ 1.851 from the former study, or just around 1.0 from the latter one. Fortunately, Weiss proved that both of these conclusions were incorrect [67, 68]. It is indeed true that the value of the critical Mach number increases with the number of moments in the system, albeit quite slowly. The critical Mach number of the 13–moment system is

≈ 1.65; it increases to ≈ 1.808 for the 21–moment system [67], and to ≈ 2.2 for the 35–moment system [4]. From a practical standpoint, this rectification is not sustainable. The number of moments, thus the number of PDEs, required for a highly supersonic or hypersonic calculation will be enormous. Solving such a huge system is no longer attractive because computational resources and running time might be similar to those for directly solving the Boltzmann equation, which would be physically preferable.

The second option is to construct f as a perturbation of the Mott–Smith bimodal distribution [43], as suggested by Ohr [46]. The nonequilibrium distribution function f is defined by

$$f = f_{\mathrm{MS}} \left[a^{(0)} H^{(0)} + a_j^{(1)} H_j^{(1)} + \frac{1}{2!} a_{ij}^{(2)} H_{ij}^{(2)} + \frac{1}{3!} a_{ijk}^{(3)} H_{ijk}^{(3)} + \cdots \right],$$

where the bimodal Mott-Smith distribution function is

$$f_{\mathrm{MS}} = \frac{\rho_1}{(2\pi R T_{\mathrm{up}})^{3/2}} \exp\left[-\frac{(\mathbf{v} - \mathbf{u}_{\mathrm{up}})^2}{2RT_{\mathrm{up}}} \right] + \frac{\rho_2}{(2\pi R T_{\mathrm{down}})^{3/2}} \exp\left[-\frac{(\mathbf{v} - \mathbf{u}_{\mathrm{down}})^2}{2RT_{\mathrm{down}}} \right].$$

The subscripts "up" and "down" indicate the upstream and downstream states of a normal to the x-direction shock. Values of ρ_1 and ρ_2 are defined so that f_{MS} gives the values of local density and x-momentum. The rest is just Grad's procedure, resulting in a hyperbolic relaxation system. It is demonstrated in [46] that a 13–moment system, derived from this revised approach, produces a smooth shock structure for Mach numbers as high as 10.

Another option, which also results in a hyperbolic relaxation system, is suggested by Butler and Anderson in a conference paper [10]. Its concept is similar to the above remedy, but not as radical. The basis for the perturbation is still the Maxwellian distribution function, but the local temperature $T(t, \mathbf{x})$ is replaced by the average of the upstream and downstream temperatures. Smooth shock profile is obtained up to $M = 10$.

However, the usefulness of this remedy and the one right above is quite restricted. They are designed specifically for the shock-structure problem as they require a priori information about upstream and downstream states; this may not be available in a realistic problem.

The last option is to transform the moment system from the hyperbolic relaxation form to a parabolic relaxation form. One choice is to use the R13 (*regularized* 13–moment) system, presented in [57, 64, 58]. This system produces a smooth shock structure up to $M = 8$ shown in Chapter 11 of Struchtrup's book [58]. Another choice is the *generalized* hydrodynamic system invented by Eu [19, 20, 21] which is demonstrated in [1] to produce smooth shock structures up to M = 10. However, due to the numerical disadvantages associated with a parabolic system, described in Section 1.1.3, these two systems are not utilized in the current study.

CHAPTER III

Boundary Treatment for Grad's Moment System

To study flow around, or bounded by, solid bodies, the governing system has to be supplemented by boundary conditions. In this chapter, I first discuss boundary conditions for the Boltzmann equation. Secondly, Grad's approach to formulating boundary conditions for Grad-type moment systems, described fully in Section 2.2, is presented. It will be shown in Section 3.3 there is inconsistency in the resulting set of boundary equations. Lastly, the alternative formulations are described in detail.

3.1 Maxwell's boundary condition for the Boltzmann equation

3.1.1 Descriptions

A wall–boundary condition for the Boltzmann equation must determine a distribution function that describes gas molecules moving back into the flow field after colliding with the solid wall [36, Section 2.9]. Figure 3.1 describes such a gas-surface interaction at an arbitrary location $\mathbf{x}$ with wall-normal $\mathbf{n}$, which points into the flow field. Before the collision, molecule has velocity vector $\mathbf{v}'$ ($\mathbf{v}' \cdot \mathbf{n} \leq 0$) and distribution function $f^- (t, \mathbf{x}, \mathbf{v}')$, which is a solution of the Boltzmann equation. The velocity vector of the molecule reemerging from the wall is $\mathbf{v}$ ($\mathbf{v} \cdot \mathbf{n} \geq 0$) and its distribution

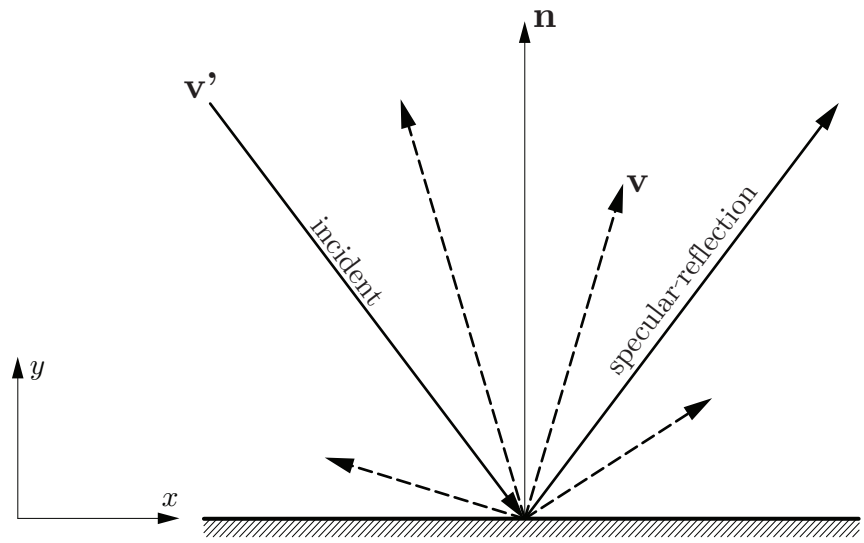

Figure 3.1: Illustration of gas-surface interaction. The velocity of re-emerging molecule cannot be determined solely based on its velocity before the collision, unless the molecule experiences a specular reflection.

function $f^{+}(t, \mathbf{x}, \mathbf{v})$ is described in the boundary conditions. Later on, for brevity, t and $\mathbf{x}$ will be dropped from the list of independent variables of distribution functions.

The velocity vectors $\mathbf{v}$ of re-emerging molecules are determinable only if they went through specular reflection at the wall. For this simplest case, the distribution function of a reflected molecule of velocity $\mathbf{v}$ is the same as that of an incident molecule having velocity $\mathbf{v}' = \mathbf{v} - 2\mathbf{n}(\mathbf{v} \cdot \mathbf{n})$; i.e., f^{+}_{specular} is the mirrored image of f^{-} with respect to the plane $(\mathbf{v} \cdot \mathbf{n} = 0)$:

$$f^{+}_{\text{specular}}(\mathbf{v}) = f^{-}(\mathbf{v}') = f^{-}(\mathbf{v} - 2\mathbf{n}(\mathbf{v} \cdot \mathbf{n})) \text{ where } \mathbf{v} \cdot \mathbf{n} \geq 0. \tag{3.1}$$

In Cartesian velocity space, the velocity vectors $\mathbf{v}$ and $\mathbf{v}'$ have the same tangential components, while their normal components are opposite:

$$\mathbf{v}' = (v_x, -v_y, v_z). \tag{3.2}$$

Thus,

$$f^{+}_{\text{specular}}\left(v_x, v_y, v_z\right) = f^{-}\left(v_x, -v_y, v_z\right) \text{ where } v_y \geq 0.$$

However, this type of reflection is extremely unrealistic [12, section 3.1]. Even a smooth surface is generally *microscopically* non-smooth; molecules are more likely to collide multiple times within the wall due to those *valleys* before moving back to the flow field. The velocity $\mathbf{v}$ can only be certainly determined when the movements of molecules "within" the wall are precisely known. Calculating these trajectories is *impossible* as it requires a huge amount of information, e. g. velocities and locations of molecules comprising the solid wall. This absence of knowledge about the structure of the surface layers is the *primary* cause for difficulties in theoretical investigation [12, 36].

Due to difficulties in deriving precise theoretical models and scantness of reliable experimental data, we may opt to use the simplest theoretical models of the gas-surface interaction (see [36, p. 89] for more details). Another option is to use plausible approximate models to prescribe the distribution function f^{+} of reflected molecules.

One of the oldest and most popular of approximate models was invented by Maxwell and published in 1879 [40]. In this model, the distribution function of reflected molecules f^{+} is a linear combination of two extreme cases, the description for *specular reflection* and the description for *diffuse reflection*. The former case has already been explained above; the latter however requires further explanation. Unlike specularly reflected molecules, diffusely reflected molecules have no "memory" of their state before the collisions. They are assumed to experience enough collisions to achieve equilibrium with the solid wall due to its microscopic roughness. Therefore, they are described by the equilibrium *Maxwellian* distribution function (Eq. (2.15) in Section 2.1.2):

$$f^{+}_{\text{diffuse}}\left(\mathbf{v}\right) = f^{\text{w}}_{\text{M}}\left(\mathbf{v}\right) \equiv \frac{\rho}{\left(2\pi R T^{\text{w}}\right)^{3/2}} \exp\left[-\frac{\mathbf{v}^2}{2RT^{\text{w}}}\right]. \tag{3.3}$$

T^{w} is the temperature of the solid wall.

The overall distribution function at the wall is expressed as:

$$\begin{aligned} f(\mathbf{v}) = f^{-}(\mathbf{v}) + f^{+}(\mathbf{v}) &= f^{-}(\mathbf{v}) + \left[\sigma C f^{+}_{\text{diffuse}}(\mathbf{v}) + (1-\sigma) f^{+}_{\text{specular}}(\mathbf{v})\right] \\ &= f^{-}(\mathbf{v}) + \left[\sigma C f^{\mathrm{w}}_{\mathrm{M}}(\mathbf{v}) + (1-\sigma) f^{-}(\mathbf{v}')\right] \end{aligned} \tag{3.4}$$

The *accommodation factor* $\sigma \in [0,1]$ is the fraction of diffusely reflected molecules. It indicates the tendency for the incident gas molecules to accommodate the surface's state. For entirely specular reflection, $\sigma = 0$; conversely, $\sigma = 1$ indicates totally diffuse reflection. The value of σ is calculated from experiments or from using the aforementioned simple approximate models of gas-surface interaction. The other not-yet-defined free parameter in expression (3.4) is the coefficient C. Its value is determined by the condition of *non-penetration*, or zero normal mass-flux, which demands the mass-fluxes of incident molecules and re-emerging molecules are the same:

$$\int_{\mathbf{v}\cdot\mathbf{n}\leq 0} (\mathbf{v}\cdot\mathbf{n})\ f^{-}(\mathbf{v})\,\mathrm{d}\mathbf{v} = -\int_{\mathbf{v}\cdot\mathbf{n}\geq 0} (\mathbf{v}\cdot\mathbf{n})\ f^{+}(\mathbf{v})\,\mathrm{d}\mathbf{v}. \tag{3.5}$$

The velocity-coordinate system used in all of these investigation is fixed with respect to the boundary. If the boundary is moving at velocity $\mathbf{u}^{\mathrm{w}}$, the velocity $\mathbf{v}$ is replaced by $\mathbf{v} - \mathbf{u}^{\mathrm{w}}$.

3.1.2 Accommodation of momentum and energy in Maxwell's boundary condition

It is known that the accommodation of momentum is different from that of energy in a gas-surface interaction. For general physical interactions, momentum is lost or gained faster than energy [12, Section 3.5], which means the accommodation factor of momentum is usually larger than the accommodation factor of energy. However, Maxwell's boundary condition is limited in this aspect because it implies the

accommodation of momentum and energy are *indistinguishable*, as shown later.

The accommodation factor of any function of molecular velocity $\mathcal{F}(\mathbf{v})$ is calculated by [12, Section 3.5]:

$$\sigma(\mathcal{F}) = \frac{\int_{\mathbf{v}\cdot\mathbf{n}\leq 0} \mathcal{F}(\mathbf{v}) |\mathbf{v}\cdot\mathbf{n}| \; f^{-}(\mathbf{v}) \, \mathrm{d}\mathbf{v} - \int_{\mathbf{v}\cdot\mathbf{n}\geq 0} \mathcal{F}(\mathbf{v}) |\mathbf{v}\cdot\mathbf{n}| \; f^{+}(\mathbf{v}) \, \mathrm{d}\mathbf{v}}{\int_{\mathbf{v}\cdot\mathbf{n}\leq 0} \mathcal{F}(\mathbf{v}) |\mathbf{v}\cdot\mathbf{n}| \; f^{-}(\mathbf{v}) \, \mathrm{d}\mathbf{v} - \int_{\mathbf{v}\cdot\mathbf{n}\geq 0} \mathcal{F}(\mathbf{v}) |\mathbf{v}\cdot\mathbf{n}| \, C' \, f_{\mathrm{M}}^{\mathrm{w}}(\mathbf{v}) \, \mathrm{d}\mathbf{v}}. \tag{3.6}$$

The numerator of Eq. (3.6) is the difference between the incident and reflected fluxes of the quantity $\mathcal{F}(\mathbf{v})$, while the denominator is the same quantity assuming that all of the incident molecules accommodate completely, in both tangential momentum and energy, to the state of the wall. The distribution of the reflected molecules in the numerator is defined in Eq. (3.4), $f^{+} = \sigma C f_{\mathrm{M}}^{\mathrm{w}} + (1-\sigma) f_{\mathrm{specular}}^{+}$, while the distribution $f_{\mathrm{M}}^{\mathrm{w}}$ in the denominator is given in Eq. (3.3). The values of parameters C and C' are calculated from the non-penetration condition (3.5).

For illustrative purposes we consider a static solid boundary occupying space $y \leq 0$, similar to the configuration in Fig. 3.1; the velocity space is Cartesian: $\mathbf{v} = (v_x, v_y, v_z)$. Because of their frequent usage, the following shortcuts are used to indicate the integrations over the full or *half-*v_y velocity space:

$$\langle \mathcal{F}(\mathbf{v}) f(\mathbf{v}) \rangle = \iiint_{-\infty}^{+\infty} \mathcal{F}(\mathbf{v}) f(\mathbf{v}) \, \mathrm{d}v_y \, \mathrm{d}v_x \, \mathrm{d}v_z, \tag{3.7a}$$

$$\langle \mathcal{F}(\mathbf{v}) f(\mathbf{v}) \rangle^{-} = \iint_{-\infty}^{+\infty} \left(\int_{-\infty}^{0} \mathcal{F}(\mathbf{v}) f(\mathbf{v}) \, \mathrm{d}v_y \right) \mathrm{d}v_x \, \mathrm{d}v_z, \tag{3.7b}$$

$$\langle \mathcal{F}(\mathbf{v}) f(\mathbf{v}) \rangle^{+} = \iint_{-\infty}^{+\infty} \left(\int_{0}^{+\infty} \mathcal{F}(\mathbf{v}) f(\mathbf{v}) \, \mathrm{d}v_y \right) \mathrm{d}v_x \, \mathrm{d}v_z. \tag{3.7c}$$

The accommodation factors of tangential momentum and energy are calculated from Eq. (3.6) with $\mathcal{F}(\mathbf{v}) = v_x$ and $\mathcal{F}(\mathbf{v}) = \mathbf{v}^2/2$, respectively. But first we have to

compute the values of C and C' from the non-penetration condition:

$$-\left\langle v_y f^- (\mathbf{v})\right\rangle^- = \sigma C \langle v_y f_{\mathrm{M}}^{\mathrm{w}} (\mathbf{v})\rangle^+ + (1-\sigma)\left\langle v_y f^- (\mathbf{v}')\right\rangle^+,$$
$$-\left\langle v_y f^- (\mathbf{v})\right\rangle^- = C' \langle v_y f_{\mathrm{M}}^{\mathrm{w}} (\mathbf{v})\rangle^+,$$

where $\mathbf{v}'$ is given by Eq. (3.2). Because $\left\langle v_y f^- (\mathbf{v}')\right\rangle^+ = -\left\langle v_y f^- (\mathbf{v})\right\rangle^-$, the values of C and C' derived from above equations are identical:

$$C = C' = -\frac{\left\langle v_y f^- (\mathbf{v})\right\rangle^-}{\langle v_y f_{\mathrm{M}}^{\mathrm{w}} (\mathbf{v})\rangle^+}.$$

Then, the accommodation factors of tangential momentum and energy are given by

$$\sigma_{\mathrm{m}} \equiv \sigma (v_x) = \frac{-\left\langle v_x v_y f^- (\mathbf{v})\right\rangle^- - \left\langle v_x v_y \left[\sigma C f_{\mathrm{M}}^{\mathrm{w}} (\mathbf{v}) + (1-\sigma) f^- (\mathbf{v}')\right]\right\rangle^+}{-\left\langle v_x v_y f^- (\mathbf{v})\right\rangle^- - C\langle v_x v_y f_{\mathrm{M}}^{\mathrm{w}} (\mathbf{v})\rangle^+}, \tag{3.8}$$

$$\sigma_{\mathrm{e}} \equiv \sigma \left(\frac{\mathbf{v}^2}{2}\right) = \frac{-\left\langle v_y \frac{\mathbf{v}^2}{2} f^- (\mathbf{v})\right\rangle^- - \left\langle v_y \frac{\mathbf{v}^2}{2}\left[\sigma C f_{\mathrm{M}}^{\mathrm{w}} (\mathbf{v}) + (1-\sigma) f^- (\mathbf{v}')\right]\right\rangle^+}{-\left\langle v_y \frac{\mathbf{v}^2}{2} f^- (\mathbf{v})\right\rangle^- - C\left\langle v_y \frac{\mathbf{v}^2}{2} f_{\mathrm{M}}^{\mathrm{w}} (\mathbf{v})\right\rangle^+}. \tag{3.9}$$

The specular-reflection terms are related to the incident terms as follows:

$$\left\langle v_x v_y f^- (\mathbf{v}')\right\rangle^+ = -\left\langle v_x v_y f^- (\mathbf{v})\right\rangle^-, \tag{3.10a}$$
$$\left\langle v_y \mathbf{v}^2/2 f^- (\mathbf{v}')\right\rangle^+ = -\left\langle v_y \mathbf{v}^2/2 f^- (\mathbf{v})\right\rangle^-, \tag{3.10b}$$

and, because of the static solid boundary,

$$\langle v_x v_y f_{\mathrm{M}}^{\mathrm{w}} (\mathbf{v})\rangle^+ = 0.$$

Inserting those into Eq. (3.8) and Eq. (3.9), we obtain the proof that tangential

momentum and energy have *identical* accommodation factors:

$$\sigma_{\mathrm{m}} = \sigma_{\mathrm{e}} = \sigma.$$

This inability to simulate the energy accommodation differently from the momentum accommodation is the basic inaccuracy of Maxwell's boundary condition. However, with a small modification shown in Section 3.1.3, the deficiency is rectifiable.

3.1.3 Modification for the accommodation of energy

In Maxwell's boundary condition, the accommodation processes of momentum and energy are indistinguishable because there exists only one accommodation factor σ in formulation (3.4). Thus, it is generally unfeasible to correctly simulate two accommodation processes simultaneously. It is necessary to add one more parameter into the formulation.

The questions are where to put the parameter and how to calculate its value. The answers are shown in the gas-kinetic books by Bird [7, Section 5.8] and Kogan [36, Section 2.10]: the wall's temperature T^{w} in the diffuse distribution (3.3) will be replaced by a new temperature called *diffuse* temperature T^{d}. The distribution function for the diffuse reflections retains its Maxwellian form, but its notation is changed from $f_{\mathrm{M}}^{\mathrm{w}}$ to $f_{\mathrm{M}}^{\mathrm{d}}$:

$$f_{\mathrm{diffuse}}^{+}(\mathbf{v}) = f_{\mathrm{M}}^{\mathrm{d}}(\mathbf{v}) \equiv \frac{\rho}{\left(2\pi R T^{\mathrm{d}}\right)^{3/2}} \exp\left[-\frac{\mathbf{v}^2}{2RT^{\mathrm{d}}}\right]; \tag{3.11}$$

and the overall distribution function at the wall (3.4) becomes

$$\begin{aligned} f(\mathbf{v}) &= f^{-}(\mathbf{v}) + \left[\sigma C f_{\mathrm{diffuse}}^{+}(\mathbf{v}) + (1-\sigma) f_{\mathrm{specular}}^{+}(\mathbf{v})\right] \\ &= f^{-}(\mathbf{v}) + \left[\sigma C f_{\mathrm{M}}^{\mathrm{d}}(\mathbf{v}) + (1-\sigma) f^{-}(\mathbf{v}')\right]. \end{aligned} \tag{3.12}$$

The values of σ and T^{d} will be calculated from the tangential-momentum and energy accommodation factors.

The expression for the accommodation factor of tangential momentum is given by

$$\sigma_{\mathrm{m}} = \frac{-\left\langle v_x v_y f^{-}(\mathbf{v})\right\rangle^{-} - \left\langle v_x v_y \left[\sigma C f_{\mathrm{M}}^{\mathrm{d}}(\mathbf{v}) + (1-\sigma) f^{-}(\mathbf{v}')\right]\right\rangle^{+}}{-\left\langle v_x v_y f^{-}(\mathbf{v})\right\rangle^{-} - C'\left\langle v_x v_y f_{\mathrm{M}}^{\mathrm{w}}(\mathbf{v})\right\rangle^{+}}; \tag{3.13}$$

by using

$$\left\langle v_x v_y f_{\mathrm{M}}^{\mathrm{d}}(\mathbf{v})\right\rangle^{+} = 0, \tag{3.14a}$$

$$\left\langle v_x v_y f_{\mathrm{M}}^{\mathrm{w}}(\mathbf{v})\right\rangle^{+} = 0, \tag{3.14b}$$

this is simplified to

$$\sigma_{\mathrm{m}} = \frac{-\left\langle v_x v_y f^{-}(\mathbf{v})\right\rangle^{-} + (1-\sigma)\left\langle v_x v_y f^{-}(\mathbf{v})\right\rangle^{-}}{-\left\langle v_x v_y f^{-}(\mathbf{v})\right\rangle^{-}} = \sigma,$$

which is identical to the previous one calculated from the original Maxwell's boundary condition. This result, owing to identities (3.14), shows that, as long as the diffuse distribution is represented by a Maxwellian form similar to (3.3), the diffuse-reflection term has no effect on the accommodation of tangential momentum.

The energy accommodation factor, derived from (3.6) with $\mathcal{F}(\mathbf{v}) = \mathbf{v}^2/2$, is given by:

$$\begin{aligned}\sigma_{\mathrm{e}} &= \frac{-\left\langle v_y \frac{\mathbf{v}^2}{2} f^{-}(\mathbf{v})\right\rangle^{-} - \left\langle v_y \frac{\mathbf{v}^2}{2}\left[\sigma C f_{\mathrm{M}}^{\mathrm{d}}(\mathbf{v}) + (1-\sigma) f^{-}(\mathbf{v}')\right]\right\rangle^{+}}{-\left\langle v_y \frac{\mathbf{v}^2}{2} f^{-}(\mathbf{v})\right\rangle^{-} - C'\left\langle v_y \frac{\mathbf{v}^2}{2} f_{\mathrm{M}}^{\mathrm{w}}(\mathbf{v})\right\rangle^{+}} \\ &= \frac{-\sigma_{\mathrm{m}}\left\langle v_y \frac{\mathbf{v}^2}{2} f^{-}(\mathbf{v})\right\rangle^{-} - \sigma_{\mathrm{m}} C\left\langle v_y \frac{\mathbf{v}^2}{2} f_{\mathrm{M}}^{\mathrm{d}}(\mathbf{v})\right\rangle^{+}}{-\left\langle v_y \frac{\mathbf{v}^2}{2} f^{-}(\mathbf{v})\right\rangle^{-} - C'\left\langle v_y \frac{\mathbf{v}^2}{2} f_{\mathrm{M}}^{\mathrm{w}}(\mathbf{v})\right\rangle^{+}};\end{aligned} \tag{3.15}$$

relation (3.10b) has been used to simplify the numerator. The values of C and C', as before, are calculated from the non-penetration condition (3.5):

$$C = -\frac{\left\langle v_y f^-(\mathbf{v})\right\rangle^-}{\left\langle v_y f_{\mathrm{M}}^{\mathrm{d}}(\mathbf{v})\right\rangle^+} = -\left\langle v_y f^-(\mathbf{v})\right\rangle^- \Big/ \rho\sqrt{\frac{RT^{\mathrm{d}}}{2\pi}}\,, \tag{3.16a}$$

$$C' = -\frac{\left\langle v_y f^-(\mathbf{v})\right\rangle^-}{\left\langle v_y f_{\mathrm{M}}^{\mathrm{w}}(\mathbf{v})\right\rangle^+} = -\left\langle v_y f^-(\mathbf{v})\right\rangle^- \Big/ \rho\sqrt{\frac{RT^{\mathrm{w}}}{2\pi}}\,. \tag{3.16b}$$

The *half-v_y-space* integrals of $f_{\mathrm{M}}^{\mathrm{d}}$ and $f_{\mathrm{M}}^{\mathrm{w}}$ have the following values:

$$\left\langle v_y \frac{\mathbf{v}^2}{2} f_{\mathrm{M}}^{\mathrm{d/w}}(\mathbf{v})\right\rangle^+ = 2\rho RT^{\mathrm{d/w}}\sqrt{\frac{RT^{\mathrm{d/w}}}{2\pi}} \tag{3.17}$$

Inserting Eq. (3.16) and Eq. (3.17) into Eq. (3.15), we obtain the following equation for the diffuse temperature T^{d}:

$$\begin{aligned}\frac{\sigma_{\mathrm{e}}}{\sigma_{\mathrm{m}}} &= \frac{\left\langle v_y \frac{\mathbf{v}^2}{2} f^-(\mathbf{v})\right\rangle^- - \frac{\left\langle v_y f^-(\mathbf{v})\right\rangle^-}{\left\langle v_y f_{\mathrm{M}}^{\mathrm{d}}(\mathbf{v})\right\rangle^+}\left\langle v_y \frac{\mathbf{v}^2}{2} f_{\mathrm{M}}^{\mathrm{d}}(\mathbf{v})\right\rangle^+}{\left\langle v_y \frac{\mathbf{v}^2}{2} f^-(\mathbf{v})\right\rangle^- - \frac{\left\langle v_y f^-(\mathbf{v})\right\rangle^-}{\left\langle v_y f_{\mathrm{M}}^{\mathrm{w}}(\mathbf{v})\right\rangle^+}\left\langle v_y \frac{\mathbf{v}^2}{2} f_{\mathrm{M}}^{\mathrm{w}}(\mathbf{v})\right\rangle^+} \\ &= \frac{\left\langle v_y \frac{\mathbf{v}^2}{2} f^-(\mathbf{v})\right\rangle^- - 2RT^{\mathrm{d}}\left\langle v_y f^-(\mathbf{v})\right\rangle^-}{\left\langle v_y \frac{\mathbf{v}^2}{2} f^-(\mathbf{v})\right\rangle^- - 2RT^{\mathrm{w}}\left\langle v_y f^-(\mathbf{v})\right\rangle^-};\end{aligned} \tag{3.18}$$

and its solution is:

$$T^{\mathrm{d}} = \frac{\sigma_{\mathrm{e}}}{\sigma_{\mathrm{m}}}T^{\mathrm{w}} + \left(1 - \frac{\sigma_{\mathrm{e}}}{\sigma_{\mathrm{m}}}\right)\frac{\left\langle v_y \frac{\mathbf{v}^2}{2} f^-(\mathbf{v})\right\rangle^-}{2R\left\langle v_y f^-(\mathbf{v})\right\rangle^-}. \tag{3.19}$$

Equation (3.19) shows that, if the accommodation factors of tangential momentum and energy are considered identical ($\sigma_{\mathrm{e}}/\sigma_{\mathrm{m}} = 1$), the diffuse temperature is always the wall's temperature $T^{\mathrm{d}} = T^{\mathrm{w}}$, which means we recover the original boundary condition by Maxwell. The other special case is that, when all of the reflected molecules

fully adjust to the wall's state, i. e. $\sigma_\mathrm{m} = \sigma_\mathrm{e} = 1$, we also obtain $T^\mathrm{d} = T^\mathrm{w}$ from (3.19); the general distribution function for diffuse reflections f_M^d becomes the wall's Maxwellian distribution f_M^w as expected. Equation (3.19) actually is the practical recipe for computing T^d. The accommodation factors σ_m and σ_e must be known from experiments or a model of gas-surface interaction.

It must be noted that the definition for the energy accommodation factor in Kogan's book differs a little bit from the one used in this section. It is given by

$$\begin{aligned}\sigma_\mathrm{e}|_\mathrm{Kogan} &= \frac{-\left\langle v_y \frac{\mathbf{v}^2}{2} f^-(\mathbf{v}) \right\rangle^- - \left\langle v_y \frac{\mathbf{v}^2}{2} \left[\sigma_\mathrm{m} C f_\mathrm{M}^\mathrm{d}(\mathbf{v}) + (1-\sigma_\mathrm{m}) f^-(\mathbf{v}')\right] \right\rangle^+}{-\left\langle v_y \frac{\mathbf{v}^2}{2} f^-(\mathbf{v}) \right\rangle^- - \left\langle v_y \frac{\mathbf{v}^2}{2} \left[\sigma_\mathrm{m} C' f_\mathrm{M}^\mathrm{w}(\mathbf{v}) + (1-\sigma_\mathrm{m}) f^-(\mathbf{v}')\right] \right\rangle^+} \\ &= \frac{-\sigma_\mathrm{m}\left\langle v_y \frac{\mathbf{v}^2}{2} f^-(\mathbf{v}) \right\rangle^- - \sigma_\mathrm{m} C \left\langle v_y \frac{\mathbf{v}^2}{2} f_\mathrm{M}^\mathrm{d}(\mathbf{v}) \right\rangle^+}{-\sigma_\mathrm{m}\left\langle v_y \frac{\mathbf{v}^2}{2} f^-(\mathbf{v}) \right\rangle^- - \sigma_\mathrm{m} C' \left\langle v_y \frac{\mathbf{v}^2}{2} f_\mathrm{M}^\mathrm{w}(\mathbf{v}) \right\rangle^+}\end{aligned} \tag{3.20}$$

The numerator is identical to the one of Eq. (3.15), while the denominator is different. The reflected molecules in the denominator are assumed to fully accommodate to the wall's state in terms of energy, but not tangential momentum, which means the reflected distribution still contains σ_m and $T^\mathrm{d} = T^\mathrm{w}$: $f^+(\mathbf{v}) = \sigma_\mathrm{m} C f_\mathrm{M}^\mathrm{w}(\mathbf{v}) + (1-\sigma_\mathrm{m}) f^-(\mathbf{v}')$.

The decoupling between momentum and energy accommodation is physically unsettling. In general, if the incident molecules accommodate completely with respect to energy, they are also fully adjusted in terms of momentum as the latter is gained or lost much faster than the former. In fact, definition (3.20) can be found only in the aforementioned reference [36], while the other definition, formula (3.15), is used in many other references, such as [7, 12, 54]. Therefore, the latter definition is used in this thesis.

3.1.4 Nocilla's model

Nocilla [44, 45] suggested another model for the gas-surface interaction that approximates experimental data better than Maxwell's model [36, p. 95]. All reflected molecules, regardless of whether they are diffusely or specularly reflected, are represented by a *single* distribution function in Maxwellian form:

$$f^{+}(\mathbf{v}) = \frac{C\rho}{(2\pi RT)^{3/2}} \exp\left[-\frac{(\mathbf{v}-\mathbf{u})^2}{2RT}\right]. \tag{3.21}$$

The value of the parameter C is again calculated from the non-penetration condition (3.5). The macroscopic velocity $\mathbf{u}$ and temperature T are calculated from the given values of the accommodation factors σ_{m} and σ_{e}. In general, their values are different from those of the wall; only when the reflections are fully diffuse they assume the wall's values, and Nicolla's model becomes identical to Maxwell's model.

3.2 Grad's approach to formulating boundary conditions

Harold Grad [23, Section 6] proposed a now classical method of formulating solid-boundary conditions for Grad-type moment systems. It is an adaptation of the original boundary condition by Maxwell presented in Section 3.1.1, which was derived originally for the Boltzmann equation.

In this approach, the expression for the distribution function $f(\mathbf{v})$ at the wall is similar to Eq. (3.4), with one fundamental difference. In the Boltzmann equation, there is no explicit expression describing the relation between distribution function f^{-} and velocity vector $\mathbf{v}$. However, for any moment system there is such a relation, which also contains bulk quantities acting as parameters. For example, there is the Gaussian distribution function for the Gaussian 10-moment system described in Section 2.2.1, and the 13-moment distribution function for Grad's 13-moment system described in Section 2.2.2, etc.

Boundary conditions for flow variables are then derived from corresponding moments of $f(\mathbf{v})$ as in (3.4):

$$\langle w(\mathbf{v}) f \rangle = \int_{\mathbf{v}\cdot\mathbf{n}<0} w(\mathbf{v}) f^{-}(\mathbf{v}) \, \mathrm{d}\mathbf{v} + \int_{\mathbf{v}\cdot\mathbf{n}>0} w(\mathbf{v}) f^{+}(\mathbf{v}) \, \mathrm{d}\mathbf{v}. \tag{3.22}$$

They are also required to have the correct behavior when reflections are purely specular ($\sigma = 0$), which means:

$$\textit{tangential} \text{ or } \textit{shear stress} = 0, \tag{3.23a}$$

$$\textit{normal heat flux} = 0. \tag{3.23b}$$

These boundary conditions inherit from those for the Boltzmann equation the limitation of equal accommodation of momentum and energy. In addition, the set of boundary conditions obtained from this procedure is also inconsistent. For most flow variables of interest, there are multiple *incompatible* expressions to describe their behavior at the boundary, and there are not enough constraints to identify the correct one, as reported in [34, 35, 62].

3.3 Inconsistencies in Grad's Approach

In this section, inconsistencies in Grad's boundary-condition formulation will be demonstrated on two moment systems in two dimensions: the 10-moment system formed by Gaussian closure and Grad's 13-moment system, described in Sections 2.2.1 and 2.2.2, respectively. Without loss of generality it is assumed that a *stationary* solid boundary ($\mathbf{u}^{\mathrm{w}} = 0$) occupies the space $y \leq 0$; x is the tangential direction as shown in Fig. 3.1. The distribution function of specularly reflected molecules $f^{+}_{\mathrm{specular}}(\mathbf{v})$ is the mirror image of the incident molecules' distribution function with respect to the

plane $v_y = 0$:

$$f^+_{\text{specular}}\left(v_x, v_y, v_z\right) = f^-\left(v_x, -v_y, v_z\right).$$

Equation (3.22) becomes:

$$\begin{aligned}\left\langle w\left(\mathbf{v}\right) f\right\rangle &= \iint_{-\infty}^{+\infty}\left(\int_{-\infty}^{0} w\left(\mathbf{v}\right) f^-\left(\mathbf{v}\right) \mathrm{d}v_y + \int_{0}^{+\infty} w\left(\mathbf{v}\right) f^+\left(\mathbf{v}\right) \mathrm{d}v_y\right) \mathrm{d}v_x\, \mathrm{d}v_z \\ &= \sigma C\left\langle w\left(\mathbf{v}\right) f^{\mathrm{w}}_{\mathrm{M}}\left(\mathbf{v}\right)\right\rangle^+ + \Big[1 \pm (1-\sigma)\Big]\left\langle w\left(\mathbf{v}\right) f^-\left(\mathbf{v}\right)\right\rangle^-; \end{aligned} \tag{3.24}$$

here "+" is applied when $w\left(\mathbf{v}\right)$ is an *even* function with respect to v_y, and "−" is used when $w\left(\mathbf{v}\right)$ is an *odd* function. The bracket shortcuts are defined in (3.7).

3.3.1 Inconsistency in 10-moment system using Gaussian closure

For this moment system, the distribution function representing incident molecules is the Gaussian distribution function (2.19):

$$f^-\left(\mathbf{c}\right) = \frac{\rho}{\left(2\pi\right)^{3/2}\Delta^{1/2}} \exp\left[-\frac{1}{2}\,\mathbf{c}^{\mathrm{T}}\cdot\left(\frac{\mathbf{P}}{\rho}\right)^{-1}\cdot\mathbf{c}\right].$$

In two dimensional space, the 10M system (2.28) reduces to a system of seven equations; its set of primitive variables is $[\rho, u_x, u_y, P_{xx}, P_{yy}, P_{zz}, P_{xy}]$. The non-penetration condition (3.5) produces $\rho u_y = 0$ or $u_y = 0$. Using Eq. (3.24) with

$$w\left(\mathbf{v}\right) = \left[1, v_x, v_y, c_x c_x, c_y c_y, c_z c_z, c_x c_y\right],$$

we derive the following algebraic system of nonlinear equations:

$$\langle f \rangle \equiv \rho \qquad = \frac{\sigma}{2} C\rho + \frac{2-\sigma}{2}\rho, \tag{3.25a}$$

$$\langle v_x f \rangle \equiv \rho u_x \qquad = (2-\sigma)\left(\frac{\rho u_x}{2} - \rho\frac{P_{xy}}{P_{yy}}\sqrt{\frac{P_{yy}}{2\pi\rho}}\right), \tag{3.25b}$$

$$\langle v_y f \rangle \equiv \rho u_y\,(=0) = \sigma C\rho\sqrt{\frac{RT^{\mathrm{w}}}{2\pi}} - \sigma\rho\sqrt{\frac{P_{yy}}{2\pi\rho}}, \tag{3.25c}$$

$$\langle c_x c_x f \rangle \equiv P_{xx} \qquad = \frac{\sigma}{2}\left(C\rho RT^{\mathrm{w}} + C\rho u_x^2\right) + \frac{2-\sigma}{2}P_{xx}, \tag{3.25d}$$

$$\langle c_y c_y f \rangle \equiv P_{yy} \qquad = \frac{\sigma}{2} C\rho RT^{\mathrm{w}} + \frac{2-\sigma}{2}P_{yy}, \tag{3.25e}$$

$$\langle c_z c_z f \rangle \equiv P_{zz} \qquad = \frac{\sigma}{2} C\rho RT^{\mathrm{w}} + \frac{2-\sigma}{2}P_{zz}, \tag{3.25f}$$

$$\langle c_x c_y f \rangle \equiv P_{xy} \qquad = -\sigma C\rho u_x\sqrt{\frac{RT^{\mathrm{w}}}{2\pi}} + \frac{\sigma}{2}P_{xy}. \tag{3.25g}$$

Boundary conditions for $[\rho, u_x, P_{xx}, P_{yy}, P_{zz}, P_{xy}]$ are the unique solution of (3.25), if it exists at all.

A close examination of the system reveals that it does not have a solution. From (3.25b), we obtain one expression for the shear stress P_{xy}. Inserting C obtained from (3.25c) into (3.25g), another expression for shear stress appears. They are nearly identical, except for a factor of $\pi/2$, as shown below:

$$\text{from (3.25b):}\ P_{xy}^{1st} = -\boxed{\frac{\pi}{2}}\frac{2\sigma}{2-\sigma}\sqrt{\frac{P_{yy}}{2\pi\rho}}\rho u_x, \tag{3.26a}$$

$$\text{from (3.25c) \& (3.25g):}\ P_{xy}^{2nd} = -\quad\frac{2\sigma}{2-\sigma}\sqrt{\frac{P_{yy}}{2\pi\rho}}\rho u_x. \tag{3.26b}$$

Obviously, $\pi/2 \neq 1.0$, thus no boundary conditions can be derived from system (3.25).

This situation was anticipated by the original author in [23, p. 380]. Grad suggested that, since the boundary conditions produced by the aforementioned procedure are "*generally incompatible*," we should use the ones derived from *odd-order* moments with respect to v_y. In this specific example it means boundary conditions will be

derived from (3.25c) and (3.25g). The former one is the essential non-penetration condition; the latter one is to guarantee shear stress P_{xy} fulfilling condition (3.23a). Evidently, (3.25g) shows that $\lim_{\sigma\to 0} P_{xy} = 0$. However, P_{xy} in (3.26a), which is not derived from an *odd-v_y-order* moment, also meets this condition. It is clear now that Grad's remedy for inconsistency does not yield a unique answer.

3.3.2 Inconsistency in Grad's 13-moment system

For this system, the distribution function representing incident molecules is Grad's 13-moment distribution function (2.30):

$$f^{13}_{\text{Grad}}(\mathbf{c}) = f_{\text{M}}(\mathbf{c})\left[1 + \frac{p_{ij}}{2pRT}c_i c_j + \frac{q_i c_i}{pRT}\left(\frac{\mathbf{c}^2}{5RT} - 1\right)\right].$$

In two dimensions, the 13M system (2.33) becomes (2.36), a system of nine equations for $[\rho, u_x, u_y, P_{xx}, P_{yy}, P_{zz}, P_{xy}, q_x, q_y]$. We follow the same procedure as in the previous section, with

$$w(\mathbf{v}) = \left[1, v_x, v_y, c_x^2, c_y^2, c_z^2, c_x c_y, 1/2 c_x \mathbf{c}^2, 1/2 c_y \mathbf{c}^2\right].$$

The boundary conditions are the solution of the following system:

$$\langle f\rangle \equiv \rho \quad = -\frac{2\,(2-\sigma)}{\sigma\,(1-C)}\sqrt{\frac{RT}{2\pi}}\frac{q_y}{5\,(RT)^2}, \tag{3.27a}$$

$$\langle v_x f\rangle \equiv \rho u_x = -\frac{10\,(2-\sigma)\,pP_{xy}}{5\sigma p\sqrt{2\pi RT}-2\,(2-\sigma)\,q_y}, \tag{3.27b}$$

$$\langle v_y f\rangle \equiv \rho u_y \equiv 0 \quad = C\sqrt{\frac{RT^{\mathrm{w}}}{2\pi}}-\frac{1}{2}\sqrt{\frac{RT}{2\pi}}\left(1+\frac{P_{yy}}{p}\right), \tag{3.27c}$$

$$\langle c_x c_x f\rangle \equiv P_{xx} = C\rho\left(u_x^2+RT^{\mathrm{w}}\right)-\frac{2\,(2-\sigma)\,q_y}{5\sigma\sqrt{2\pi RT}}, \tag{3.27d}$$

$$\langle c_y c_y f\rangle \equiv P_{yy} = C\rho RT^{\mathrm{w}}-\frac{4\,(2-\sigma)\,q_y}{5\sigma\sqrt{2\pi RT}}, \tag{3.27e}$$

$$\langle c_z c_z f\rangle \equiv P_{zz} = C\rho RT^{\mathrm{w}}-\frac{2\,(2-\sigma)\,q_y}{5\sigma\sqrt{2\pi RT}}, \tag{3.27f}$$

$$\langle c_x c_y f\rangle \equiv P_{xy} = -\frac{2\sigma}{2-\sigma}\left(\sqrt{\frac{RT^{\mathrm{w}}}{2\pi}}C\rho u_x+\frac{q_x}{5\sqrt{2\pi RT}}\right), \tag{3.27g}$$

$$\left\langle \frac{1}{2}c_x\mathbf{c}^2 f\right\rangle \equiv q_x \quad = -\frac{C\rho u_x}{2}\left(u_x^2+5RT^{\mathrm{w}}\right)-\frac{2-\sigma}{\sigma}\sqrt{\frac{RT}{2\pi}}6P_{xy}, \tag{3.27h}$$

$$\left\langle \frac{1}{2}c_y\mathbf{c}^2 f\right\rangle \equiv q_y \quad = \frac{\sigma}{2-\sigma}\sqrt{\frac{RT^{\mathrm{w}}}{2\pi}}\left[C\rho\left(u_x^2+4RT^{\mathrm{w}}\right)-\sqrt{\frac{RT}{RT^{\mathrm{w}}}}\left(p+3P_{yy}\right)\right]. \tag{3.27i}$$

This system is also "*incompatible*" as predicted, because it has either no solution or, at the very least, two solutions:

$$\left[\rho_0, \pm u_{x0}, 0, P_{xx0}, P_{yy_0}, P_{zz0}, \pm P_{xy_0}, \pm q_{x0}, q_{y_0}\right].$$

It is obvious that P_{xy} derived either from the *odd-v_y-order* moment (3.27g) or the *even-v_y-order* moments (3.27b) and (3.27h), satisfies condition (3.23a). Similarly, the normal heat flux q_y satisfies condition (3.23b), regardless of whether it is derived from the *odd-v_y-order* moment (3.27i) or *even-v_y-order* moments Eqs. (3.27a), (3.27b) and (3.27d) to (3.27f).

3.4 Alternative Approaches

The inconsistency described in Section 3.3 is caused by a discrepancy between the number of constraints, implicit and explicit, acting on (3.4) and the number of useful *degrees-of-freedom* it possesses. Local average quantities at the wall are utilized in the distribution function f^- of incident molecules. This makes that local average quantities will appear on the right-hand side of (3.22), while its left-hand side, by definition, is also one local average quantity. When (3.22) is used to compute average quantities at the wall for boundary conditions, the expressions obtained are interconnected because one local quantity can appear in multiple expressions. This is technically equivalent to imposing additional conditions on the distribution function (3.4). However, there is no available freedom to satisfy these new conditions; the only *degree-of-freedom* in Grad's formulation has already been used to satisfy the *non-penetration* condition.

Next are our attempts to circumvent this inconsistency. We will also include the distinct energy accommodation factor allowed by the modification presented in Section 3.1.3. Thus, the overall distribution function at the boundary is represented by Eq. (3.12), instead of Eq. (3.4).

3.4.1 1−C solid-boundary condition model

Technically, there are two ways to remedy the inconsistency problem. Either we add more *degrees of freedom—dofs*, or eliminate all those extra implicit constraints. The former option is a complex procedure. The first step is to find out how many more constraints are imposed implicitly, which strongly depends on the moment system being studied. It is known that, for fluid dynamics, a useful moment system has at least ten variables. We might have to add that many *dofs* to Eq. (3.12) to satisfy additional constraints. Two *dofs* can be added in front of f^- and f^+_{specular}, other ones would have to be included inside of the expressions for the components

of the distribution function. To derive those expressions from physical principle is complicated; clearly, adding additional *dofs* is not to be taken lightly.

The second option, in contrast to the first one, produces a common procedure for all moment systems. To eliminate all additional constraints, distribution functions of incident molecules and specularly reflected molecules should be constituted from known macroscopic quantities, denoted by superscript "$\sim$," instead of unknown local ones as in the original approach. The former is a physically plausible assumption. The Knudsen layer has a thickness only in the order of only one mean free path [32, p. 70], or only a few mean free paths [58, p. 12]. Molecules are likely to travel without collisions within this layer; the dominant collisions are molecule-surface interactions. Thus, there is good chance that incident molecules do not adapt instantly to the local condition; their prior properties are unchanged until they collide with the solid boundary.

The overall distribution function at the boundary is distribution (3.12):

$$f\left(\mathbf{v}\right) = f^{-}\left(\mathbf{v}\right) + \left[\sigma C f_{\mathrm{M}}^{\mathrm{d}}\left(\mathbf{v}\right) + \left(1-\sigma\right) f^{-}\left(\mathbf{v}'\right)\right];$$

here $\sigma = \sigma_{\mathrm{m}}$, and the diffuse temperature for $f_{\mathrm{M}}^{\mathrm{d}}$ is again given by formula (3.19) for the static wall:

$$T^{\mathrm{d}} = \frac{\sigma_{\mathrm{e}}}{\sigma_{\mathrm{m}}} T^{\mathrm{w}} + \left(1 - \frac{\sigma_{\mathrm{e}}}{\sigma_{\mathrm{m}}}\right) \frac{\left\langle v_y \dfrac{\mathbf{v}^2}{2} f^{-}\left(\mathbf{v}\right)\right\rangle^{-}}{2R\left\langle v_y f^{-}\left(\mathbf{v}\right)\right\rangle^{-}}.$$

All subsequent steps are similar to those in Grad's original formulation. The notable change is that Eq. (3.22) becomes a recipe for computing flow quantities at the solid boundary in terms of known quantities of incident molecules, and parameters of the solid boundary. The previous couplings are removed. This formulation is a straightforward adaptation of the modified Maxwell's boundary condition presented in Section 3.1.3. We call this the "1–*Coefficient*", or "1–C" boundary model from

now on for a reason that will become obvious later.

3.4.2 2–C solid-boundary condition model

The second alternative treatment is an extension of the 1–C model. We suggest to impose a new condition on $f(\mathbf{v})$ formed in (3.12) besides *non-penetration*; it is a *normalization* condition:

$$\langle f/\rho \rangle \equiv \left\langle \widehat{f} \right\rangle = 1. \tag{3.28}$$

This requires further explanation. The distribution function $f(\mathbf{v})\,\mathrm{d}\mathbf{v}$ expresses the mass density of molecules having a total velocity in the range of $\mathbf{v} \to \mathbf{v} + \mathrm{d}\mathbf{v}$, at an arbitrary space-time location. On the other hand, the distribution function $\widehat{f} = f/\rho$ carries *no information* about the mass density; $\widehat{f}(v_x, v_y, v_z)\,d\mathbf{v}$ expresses the *probability* to find a molecule having its velocity in the range $\mathbf{v} \to \mathbf{v} + d\mathbf{v}$, at an arbitrary space-time location. All molecules in the flow field have a real velocity vector; thus there is 100% certainty to find a molecule with its velocity in the range of $\mathbf{v}$ from $-\infty$ to $+\infty$. This leads to making the *normalization* condition (3.28) a fundamental requirement.

To satisfy the normalization condition, an additional *dof* in the form of a coefficient C_1 is introduced into the representation for incident molecules; the coefficient C in the diffuse-reflection term is renamed C_2. This creates the 2-C model; the one with one *dof* is called the 1–C model. The coefficient C_1 must also appear in the expression for specular reflection as this type of reflection does not change anything but the sign of the normal component of momentum. The expression for the overall distribution function changes from Eq. (3.12) to Eq. (3.29). It contains *four* parameters: C_1, C_2, σ, and T^{d}; their values are determined from *non-penetration* condition (3.5), *normalization* condition (3.28), and the accommodation factors of tangential-momentum σ_{m}

and energy σ_e.

$$f(\mathbf{v}) = C_1 f^-(\mathbf{v}) + \left[\sigma C_2 f_M^d(\mathbf{v}) + (1-\sigma) C_1 f^-(\mathbf{v}')\right]. \tag{3.29}$$

Parameters C_1 and C_2 satisfy the following conditions:

$$C_1\langle v_y f^-(\mathbf{v})\rangle^- + \sigma C_2\langle v_y f_M^d(\mathbf{v})\rangle^+ + (1-\sigma) C_1\langle v_y f^-(\mathbf{v}')\rangle^+ = 0, \tag{3.30a}$$

$$C_1\left\langle \widehat{f}^-(\mathbf{v})\right\rangle^- + \sigma C_2\left\langle \widehat{f}_M^d(\mathbf{v})\right\rangle^+ + (1-\sigma) C_1\left\langle \widehat{f}^-(\mathbf{v}')\right\rangle^+ = 1. \tag{3.30b}$$

Using the following relations

$$\langle v_y f^-(\mathbf{v}')\rangle^+ = -\langle v_y f^-(\mathbf{v})\rangle^-, \text{ and } \left\langle \widehat{f}^-(\mathbf{v}')\right\rangle^+ = \left\langle \widehat{f}^-(\mathbf{v})\right\rangle^-,$$

system (3.30) is simplified to

$$C_1\langle v_y f^-(\mathbf{v})\rangle^- + C_2\langle v_y f_M^d(\mathbf{v})\rangle^+ = 0, \tag{3.31a}$$

$$(2-\sigma) C_1\left\langle \widehat{f}^-(\mathbf{v})\right\rangle^- + \sigma C_2\left\langle \widehat{f}_M^d(\mathbf{v})\right\rangle^+ = 1; \tag{3.31b}$$

of which the solution is

$$\begin{bmatrix} C_1 \\ C_2 \end{bmatrix} = \frac{1}{\Delta}\begin{bmatrix} -\langle v_y f_M^d(\mathbf{v})\rangle^+ \\ \langle v_y f^-(\mathbf{v})\rangle^+ \end{bmatrix}, \tag{3.32}$$

where

$$\Delta = \sigma\langle v_y f^-(\mathbf{v})\rangle^-\left\langle \widehat{f}_M^d(\mathbf{v})\right\rangle^+ - (2-\sigma)\left\langle \widehat{f}^-(\mathbf{v})\right\rangle^-\langle v_y f_M^d(\mathbf{v})\rangle^+.$$

The accommodation factors for tangential momentum and energy are expressed

by

$$\sigma_{\mathrm{m}} = \frac{-C_1\left\langle v_x v_y f^-(\mathbf{v})\right\rangle^- - \left\langle v_x v_y\left[\sigma C_2 f_{\mathrm{M}}^{\mathrm{d}}(\mathbf{v}) + (1-\sigma) C_1 f^-(\mathbf{v}')\right]\right\rangle^+}{-C_1'\left\langle v_x v_y f^-(\mathbf{v})\right\rangle^- - C_2'\langle v_x v_y f_{\mathrm{M}}^{\mathrm{w}}(\mathbf{v})\rangle^+}$$
$$= \frac{\sigma C_1\left\langle v_x v_y f^-(\mathbf{v})\right\rangle^- + \sigma C_2\left\langle v_x v_y f_{\mathrm{M}}^{\mathrm{d}}(\mathbf{v})\right\rangle^+}{C_1'\left\langle v_x v_y f^-(\mathbf{v})\right\rangle^- + C_2'\langle v_x v_y f_{\mathrm{M}}^{\mathrm{w}}(\mathbf{v})\rangle^+} = \sigma\frac{C_1}{C_1'}, \quad (3.33a)$$

$$\sigma_{\mathrm{e}} = \frac{-C_1\left\langle v_y\frac{\mathbf{v}^2}{2} f^-(\mathbf{v})\right\rangle^- - \left\langle v_y\frac{\mathbf{v}^2}{2}\left[\sigma C_2 f_{\mathrm{M}}^{\mathrm{d}}(\mathbf{v}) + (1-\sigma) C_1 f^-(\mathbf{v}')\right]\right\rangle^+}{-C_1'\left\langle v_y\frac{\mathbf{v}^2}{2} f^-(\mathbf{v})\right\rangle^- - C_2'\left\langle v_y\frac{\mathbf{v}^2}{2} f_{\mathrm{M}}^{\mathrm{w}}(\mathbf{v})\right\rangle^+}$$
$$= \frac{\sigma C_1\left\langle v_y\frac{\mathbf{v}^2}{2} f^-(\mathbf{v})\right\rangle^- + \sigma C_2\left\langle v_y\frac{\mathbf{v}^2}{2} f_{\mathrm{M}}^{\mathrm{d}}(\mathbf{v})\right\rangle^+}{C_1'\left\langle v_y\frac{\mathbf{v}^2}{2} f^-(\mathbf{v})\right\rangle^- + C_2'\left\langle v_y\frac{\mathbf{v}^2}{2} f_{\mathrm{M}}^{\mathrm{w}}(\mathbf{v})\right\rangle^+}$$
$$= \underbrace{\sigma\frac{C_1}{C_1'}}_{\sigma_{\mathrm{m}}} \frac{\left\langle v_y\frac{\mathbf{v}^2}{2} f^-(\mathbf{v})\right\rangle^- + \frac{C_2}{C_1}\left\langle v_y\frac{\mathbf{v}^2}{2} f_{\mathrm{M}}^{\mathrm{d}}(\mathbf{v})\right\rangle^+}{\left\langle v_y\frac{\mathbf{v}^2}{2} f^-(\mathbf{v})\right\rangle^- + \frac{C_2'}{C_1'}\left\langle v_y\frac{\mathbf{v}^2}{2} f_{\mathrm{M}}^{\mathrm{w}}(\mathbf{v})\right\rangle^+}. \quad (3.33b)$$

The parameters C_1' and C_2' also have to satisfy conditions (3.5) and (3.28), which results in a system similar to system (3.31):

$$C_1'\left\langle v_y f^-(\mathbf{v})\right\rangle^- + C_2'\langle v_y f_{\mathrm{M}}^{\mathrm{w}}(\mathbf{v})\rangle^+ = 0,$$
$$C_1'\left\langle \widehat{f}^-(\mathbf{v})\right\rangle^- + C_2'\left\langle \widehat{f}_{\mathrm{M}}^{\mathrm{w}}(\mathbf{v})\right\rangle^+ = 1;$$

its solution is

$$\begin{bmatrix} C_1' \\ C_2' \end{bmatrix} = \frac{1}{\Delta'}\begin{bmatrix} -\langle v_y f_{\mathrm{M}}^{\mathrm{w}}(\mathbf{v})\rangle^+ \\ \left\langle v_y f^-(\mathbf{v})\right\rangle^+ \end{bmatrix}, \quad (3.34)$$

where

$$\Delta' = \left\langle v_y f^-(\mathbf{v})\right\rangle^-\left\langle \widehat{f}_{\mathrm{M}}^{\mathrm{w}}(\mathbf{v})\right\rangle^+ - \left\langle \widehat{f}^-(\mathbf{v})\right\rangle^-\langle v_y f_{\mathrm{M}}^{\mathrm{w}}(\mathbf{v})\rangle^+.$$

Substituting from Eq. (3.32) and Eq. (3.34) for the ratios C_2/C_1 and C_2'/C_1' in Eq. (3.33b) we obtain:

$$\frac{\sigma_e}{\sigma_m} = \frac{\left\langle v_y \frac{\mathbf{v}^2}{2} f^- (\mathbf{v}) \right\rangle^- - \frac{\langle v_y f^- (\mathbf{v}) \rangle^-}{\langle v_y f_M^d (\mathbf{v}) \rangle^+} \left\langle v_y \frac{\mathbf{v}^2}{2} f_M^d (\mathbf{v}) \right\rangle^+}{\left\langle v_y \frac{\mathbf{v}^2}{2} f^- (\mathbf{v}) \right\rangle^- - \frac{\langle v_y f^- (\mathbf{v}) \rangle^-}{\langle v_y f_M^w (\mathbf{v}) \rangle^+} \left\langle v_y \frac{\mathbf{v}^2}{2} f_M^w (\mathbf{v}) \right\rangle^+}. \tag{3.35}$$

Expression for this σ_e/σ_m is identical to Eq. (3.18); thus, for the case of the static wall, the diffuse temperature of the 2–C model is given by the same formula (3.19) as for the 1–C model. The formula for the parameter σ is derived from Eq. (3.33a), in combination with the solutions (3.32) and (3.34):

$$\begin{aligned} \sigma &= \frac{-2\sigma_m}{\frac{\left\langle \widehat{f}_M^w (\mathbf{v}) \right\rangle^+}{\left\langle \widehat{f}^- (\mathbf{v}) \right\rangle^-} \frac{\langle v_y f^- (\mathbf{v}) \rangle^-}{\langle v_y f_M^w (\mathbf{v}) \rangle^+} \left[1 - \sigma_m \frac{\left\langle \widehat{f}_M^d (\mathbf{v}) \right\rangle^+}{\left\langle \widehat{f}_M^w (\mathbf{v}) \right\rangle^+} \frac{\langle v_y f_M^w (\mathbf{v}) \rangle^+}{\langle v_y f_M^d (\mathbf{v}) \rangle^+} \right] - (1 + \sigma_m)} \\ &= \frac{-2\sigma_m}{\left(1 - \sigma_m \sqrt{\frac{T^w}{T^d}} \right) \frac{\left\langle \widehat{f}_M^w (\mathbf{v}) \right\rangle^+}{\left\langle \widehat{f}^- (\mathbf{v}) \right\rangle^-} \frac{\langle v_y f^- (\mathbf{v}) \rangle^-}{\langle v_y f_M^w (\mathbf{v}) \rangle^+} - (1 + \sigma_m)}, \end{aligned} \tag{3.36}$$

where, for static wall, $\left\langle \widehat{f}_M^{d(w)} (\mathbf{v}) \right\rangle^+ = 1/2$ and $\left\langle v_y f_M^{d(w)} (\mathbf{v}) \right\rangle^+ = \sqrt{RT^{d(w)}/2\pi}$.

Equation (3.35) shows that, when the original boundary condition of Maxwell is used ($f_M^d = f_M^w$), then $\sigma_e/\sigma_m = 1$, and the 2–C formulation can not differentiate between the momentum and energy accommodation, just as the 1–C formulation couldn't. When the reflections are diffuse, with respect to both tangential momentum and energy, Eq. (3.36) will gives $\sigma = 1$.

CHAPTER IV

Solution methods

4.1 Analytical Navier–Stokes–Fourier solutions for Couette and Poiseuille flows

The configurations of Couette and Poiseuille flows are shown in Figure 4.1. They are the simplest flows that are still physically adequate for studying velocity-slip and temperature-jump phenomena at a solid boundary. The flow-fields are bound by two parallel flat plates infinitely extending in the z-direction. The temperature of the top and bottom plates is held constant at the same value T^{w}.

Owing to the simple geometry and the relatively straightforward physics of *laminar incompressible* flow, the *steady-state* solutions for these flows can be derived as a complete set of analytical expressions. Turbulent flow is not considered because ***a***) turbulence model for the moment systems is not available; and ***b***) direct simulations similarly to DNS for the NSF system are expensive. The effects of compressibility is also not studied because of the relative difficulties in computing the NSF solutions. At this limit, the system of ODEs simulating steady state has to be solved numerically.

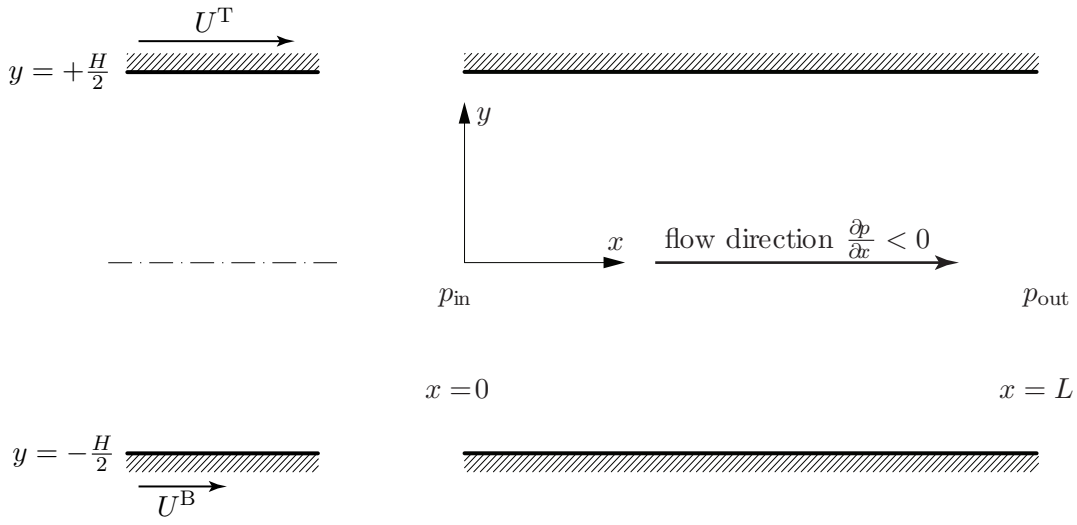

(a) Couette flow (Quasi-1D) **(b)** Poiseuille flow (2D)

Figure 4.1: The configurations of flows between two parallel plates.

For 2D flows, the steady-state NSF system is given by

$$\frac{\partial}{\partial x}\begin{bmatrix} \rho u_x \\ \rho u_x^2 + P_{xx} \\ \rho u_x u_y + P_{xy} \\ \rho u_x \left(\dfrac{u^2}{2} + \dfrac{3}{2}\dfrac{p}{\rho}\right) + u_x P_{xx} + u_y P_{xy} + q_x \end{bmatrix} + \frac{\partial}{\partial y}\begin{bmatrix} \rho u_y \\ \rho u_x u_y + P_{xy} \\ \rho u_y^2 + P_{yy} \\ \rho u_y \left(\dfrac{u^2}{2} + \dfrac{3}{2}\dfrac{p}{\rho}\right) + u_x P_{xy} + u_y P_{yy} + q_y \end{bmatrix} = \begin{bmatrix} 0 \\ 0 \\ 0 \\ 0 \end{bmatrix}. \quad (4.1)$$

The components of the pressure tensor P_{ij} are related to the velocity-derivatives by Eq. (2.8) and Eq. (2.9); while the relation between the heat flux q_i and the derivatives of temperature is described by Eq. (2.12). The system will be solved with the second-order velocity-slip and temperature-jump boundary conditions. The former is given

by

$$u_x|_{\pm\frac{H}{2}} = U^{\mathrm{T,B}} + \frac{2-\sigma_{\mathrm{m}}}{\sigma_m}\left[\mp\lambda D_1 \left.\frac{\partial u_x}{\partial y}\right|_{\pm\frac{H}{2}} - \lambda^2 D_2 \left.\frac{\partial^2 u_x}{\partial y^2}\right|_{\pm\frac{H}{2}}\right], \tag{4.2}$$

which is a combination of Eqn. (2.29) and Eqn. (2.42) in [32]; the latter has the following form

$$T|_{\pm\frac{H}{2}} = T^{\mathrm{w}} + \frac{1}{Pr}\frac{2\gamma}{\gamma+1}\frac{2-\sigma_{\mathrm{e}}}{\sigma_{\mathrm{e}}}\left[\mp\lambda E_1 \left.\frac{\partial T}{\partial y}\right|_{\pm\frac{H}{2}} + \lambda^2 E_2 \left.\frac{\partial^2 T}{\partial y^2}\right|_{\pm\frac{H}{2}}\right]. \tag{4.3}$$

The values of the parameters (D_1, D_2) and (E_1, E_2) are shown in Table 4.1. The mean-free-path λ is defined by:

$$\lambda = \sqrt{\frac{\pi}{2RT^{\mathrm{w}}}}\frac{\mu}{\rho}, \tag{4.4}$$

which is only 1.8% different from the hard-sphere mean-free-path λ_{HS}

$$\lambda_{\mathrm{HS}} = \frac{16}{5}\frac{\mu}{\rho\sqrt{2\pi RT^{\mathrm{w}}}}. \tag{4.5}$$

4.1.1 Couette flow

In Couette flow, the top and bottom plates travel horizontally at the constant velocities U^{T} and U^{B}. Due to the viscous effect, the motion of the plates will propagate into the initially static flow field, therefore Couette flow is also called *shear-driven* flow. Because the plates' x-dimension is also considered infinite and their velocities are constant, the flow is considered quasi-one-dimensional, in which the flow quantities vary only in the y-direction. The steady-state NSF system (4.1) is simplified

Table 4.1: Values of (D_1, D_2) in the velocity-slip (from Table 2.2 in [32]) and (E_1, E_2) in the temperature-jump boundary conditions for the NSF system.

Authors		D_1	D_2	E_1	E_2
No-slip		0.0	0.0	0.0	0.0
1^{st}-order	Maxwell [33]	1.0	0.0		
	Von Smoluchowski [33]			1.0	0.0
2^{nd}-order	Cercignani [11]	1.1466	0.9756		
	Cercignani [26]	1.1466	0.647		
	Sreekanth [56]	1.1466	0.14		
	Deissler [18]	1.0	9/8		
	Schamberg [51]	1.0	$5\pi/12$		
	Hsia and Domoto [31]	1.0	1/2		
	Karniadakis et al. [32, Eqn. (2.29)]	1.0	-1/2		
	Karniadakis et al. [32, Eqn. (2.30)]			1.0	1/2

to

$$\frac{\mathrm{d}}{\mathrm{d}y}\begin{bmatrix} \rho u_y \\ \rho u_x u_y + P_{xy} \\ \rho u_y^2 + P_{yy} \\ \rho u_y\left(\dfrac{u^2}{2} + \dfrac{3}{2}\dfrac{p}{\rho}\right) + u_x P_{xy} + u_y P_{yy} + q_y \end{bmatrix} = \begin{bmatrix} 0 \\ 0 \\ 0 \\ 0 \end{bmatrix}. \tag{4.6}$$

For incompressible flow, the variation of density in the flow field is negligible, so that it can be considered as a constant quantity. The first equation of system (4.6) shows that $u_y(y)$ will be a constant; because the boundary plates do not move in the y-direction, its solution has to be $u_y = 0$ through out the flow field. The constitutive equation (2.9) is simplified to $P_{xy} = -\mu\frac{\mathrm{d}u_x}{\mathrm{d}y}$ and $P_{yy} = p$; the third equation of (4.6) gives $p = \text{const}$. The expressions for $u_x(y)$ and $T(y)$ are solutions of the following

system of ODEs

$$\frac{\mathrm{d}^2}{\mathrm{d}y^2}\begin{bmatrix} u_x \\ T \end{bmatrix} = \begin{bmatrix} 0 \\ -\dfrac{\mu}{k}\left(\dfrac{\mathrm{d}u_x}{\mathrm{d}y}\right)^2 \end{bmatrix}. \tag{4.7}$$

The first equation shows that $u_x(y)$ is only a linear function; the second-order modification to the velocity-slip boundary condition does not matter in this case. Using the boundary conditions (4.2) (1^{st}-order only) and (4.3), we obtain

$$u_x(y) = \frac{U^{\mathrm{T}} + U^{\mathrm{B}}}{2} + \frac{\mathrm{d}u_x}{\mathrm{d}y} y, \tag{4.8}$$

$$T(y) = T^{\mathrm{w}} + \frac{\mu H^2}{2k}\left(\frac{\mathrm{d}u_x}{\mathrm{d}y}\right)^2 \left[\frac{1}{Pr}\frac{2\gamma}{\gamma+1}\frac{2-\sigma_{\mathrm{e}}}{\sigma_{\mathrm{e}}} Kn\left(E_1 - 2E_2 Kn\right) + \frac{1}{4} - \frac{y^2}{H^2}\right], \tag{4.9}$$

where

$$\frac{\mathrm{d}u_x}{\mathrm{d}y} = \frac{1}{1 + 2\dfrac{2-\sigma_{\mathrm{m}}}{\sigma_{\mathrm{m}}} Kn} \frac{U^{\mathrm{T}} - U^{\mathrm{B}}}{H}.$$

Then, the expressions for shear stress and heat fluxes are

$$P_{xy} = -\mu \frac{\mathrm{d}u_x}{\mathrm{d}y}, \tag{4.10}$$

$$q_x(y) = -k\frac{\mathrm{d}T}{\mathrm{d}x} = 0, \tag{4.11}$$

$$q_y(y) = -k\frac{\mathrm{d}T}{\mathrm{d}y} = \mu\left(\frac{\mathrm{d}u_x}{\mathrm{d}y}\right)^2 y. \tag{4.12}$$

It is interesting that the modification to account for the temperature-jump does not have any effect on any other flow-quantities, namely P_{xy}, $q_x(y)$, and $q_y(y)$.

4.1.2 Poiseuille flow

Contrary to Couette flow, the plates in Poiseuille flow are static and finite; their length is denoted by L. The left-to-right flow is driven by a negative pressure gradient in the x-direction. At the inlet of the channel, there is a region of the *entrance effect*,

in which the boundary layers of the top and bottom plates are growing and have not touched each other yet; the flow quantities are functions of both x and y. However, once the two boundary layers merge, the flow can be considered moving purely in the horizontal direction, i. e. $u_y = 0$. It is now called *fully-developed* flow.

Due to the incompressibility, and the assumption $u_y = 0$, the first equation of system (4.1) shows that u_x is not a function of x. The third equation reduces to $\partial p/\partial y = 0$ indicating that pressure only varies in the x-direction. The second and last equations become

$$\frac{\mathrm{d}^2}{\mathrm{d}y^2}\begin{bmatrix} u_x \\ T \end{bmatrix} = \begin{bmatrix} \dfrac{1}{\mu}\dfrac{\mathrm{d}p}{\mathrm{d}x} \\ -\dfrac{\mu}{k}\left(\dfrac{\mathrm{d}u_x}{\mathrm{d}y}\right)^2 + \dfrac{3}{2k}\dfrac{\mathrm{d}p}{\mathrm{d}x}u_x \end{bmatrix}. \tag{4.13}$$

As u_x remains a function of y only, $\mathrm{d}p/\mathrm{d}x$ cannot be a function of x, so $\mathrm{d}p/\mathrm{d}x$ can only be a constant, or p is linear in x.

System (4.13) is solved with boundary conditions (4.2) and (4.3) to obtain the following results:

$$u_x(y) = \frac{H^2}{2\mu}\frac{\mathrm{d}p}{\mathrm{d}x}\left[\frac{y^2}{H^2} - \frac{1}{4} - \frac{2-\sigma_\mathrm{m}}{\sigma_\mathrm{m}}Kn\left(D_1 + 2D_2Kn\right)\right], \tag{4.14}$$

$$\begin{aligned} T(y) = T^\mathrm{w} + \frac{H^4}{96k\mu}\left(\frac{\mathrm{d}p}{\mathrm{d}x}\right)^2 \Bigg[&- \frac{y^2}{H^2}\left(9 + 36D + 2\frac{y^2}{H^2}\right) + \frac{19}{8} + 9D \\ &+ 2Kn\frac{1}{Pr}\frac{2\gamma}{\gamma+1}\frac{2-\sigma_\mathrm{e}}{\sigma_\mathrm{e}}\left(18D\left(E_1 - 2E_2Kn\right) + 5E_1 - 12E_2Kn\right)\Bigg], \end{aligned} \tag{4.15}$$

where

$$D = \frac{2-\sigma_\mathrm{m}}{\sigma_\mathrm{m}}Kn\left(D_1 + 2D_2Kn\right).$$

Shear stress and heat fluxes are calculated from their derivatives as

$$P_{xy} = -\mu \frac{\mathrm{d}u_x}{\mathrm{d}y} = -\frac{\mathrm{d}p}{\mathrm{d}x} y, \tag{4.16}$$

$$q_x(x) = -k \frac{\mathrm{d}T}{\mathrm{d}x} = 0, \tag{4.17}$$

$$q_y(y) = -k \frac{\mathrm{d}T}{\mathrm{d}y} = \frac{H^3}{48\mu} \left(\frac{\mathrm{d}p}{\mathrm{d}x} \right)^2 \frac{y}{H} \left(9 + 36D + 4\frac{y^2}{H^2} \right). \tag{4.18}$$

As in Couette flow, P_{xy}, q_x, and q_y of Poiseuille flow are not affected by modification accounting for the temperature-jump's.

4.2 Numerical methods for Grad's 13-moment system

Section 4.1 shows that, for steady-state Couette or Poiseuille flows at the limit of laminar and incompressible flow, the NSF system reduces to a system of only two ODEs. Coupled with the nice form of the slip boundary conditions (4.2) and (4.3), it allows of analytical solutions. For Grad's 13–moment system, however, due to the much larger set of dependent variables and the intricate form of the boundary conditions, there is no other possibility but to solve (2.36) numerically.

In the current study, the 13M system will be solved numerically by the piecewise-linear ($p = 1$ or $p1$) Finite-Volume (FV) and Discontinuous Galerkin (DG) methods. From the previous study by Suzuki [60], the latter was shown to offer distinct advantages of accuracy and compactness over other traditional spatial discretizations, such as FV. DG will be the primary discretization, while FV will be used for comparison purposes.

The most popular choice of the $p1$ FV scheme is the venerable MUSCL-Hancock scheme [65]. It is a fully-discrete method that is robust, "*battle-tested*", and easy to implement in the computer program. However, it is not suitable for the steady-state problems because its steady-state solution depends on the precise time-step used.

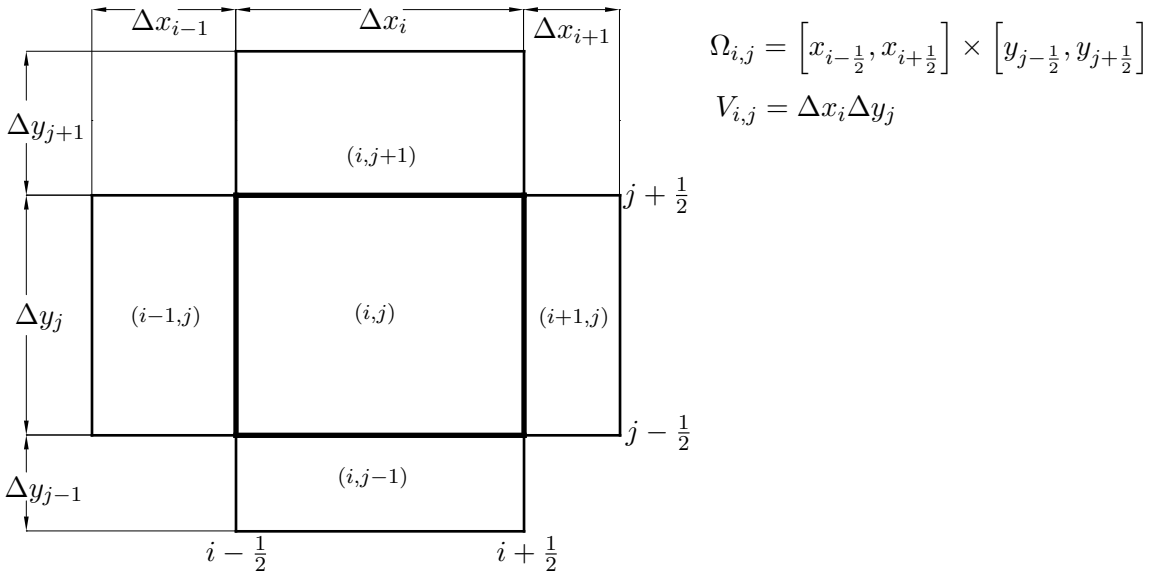

Figure 4.2: Configuration of the computational cells of a *non-uniform* Cartesian mesh in the two-dimensional *physical space*. Index i indicates the x-coordinate, while j will be used exclusively for the y-coordinate.

Thus it was decided to use a semi-discretization instead.

In the case of the DG discretization, both semi-discrete and fully-discrete (space-time) versions are available. The former generally has the advantage of simplicity and flexibility, while the latter is more accurate and allows a larger CFL number. We decided to use the semi-discrete version for its simplicity, and also because the steady-state solutions are our main focus, not the temporally accurate ones.

The following sub-sections will first describe the method-of-lines and the Runge–Kutta method used for temporal discretization, then the $p1$ FV and DG spatial discretizations for a non-uniform Cartesian mesh in the two-dimensional physical space. Figure 4.2 shows the typical configuration of a physical cell and its neighboring cells sharing common interfaces.

4.2.1 The Method-of-Lines discretization

In a semi-discrete numerical scheme, the PDEs are divided into two parts,

$$\frac{\partial \mathbf{U}}{\partial t} + \frac{\partial \mathbf{F}^{(\alpha)}}{\partial x_\alpha} = \mathbf{S} \rightarrow \frac{\partial \mathbf{U}}{\partial t} = \mathbf{R}(\mathbf{U}) \,, \tag{4.19}$$

which are to be discretized independently:

- the residual $\mathbf{R}(\mathbf{U})$ is comprised by terms that do not contain temporal derivative, i.e., the spatial derivatives and source term. It will be numerically approximated by spatial discretizations, which in this study are according to the FV and DG methods.

- the temporal derivative $\partial_t \mathbf{U}$, which will be discretized by appropriate time-integration schemes such as the one-step multi-stage method or multi-step methods. Interested readers can find more information about the time-integration schemes in LeVeque [37, Part II]. We will use the *explicit* Runge–Kutta method, which is a one-step multi-stage method.

Marching to a steady state by an explicit method is not the most efficient. To remain stable, the time-step is sometimes severely restricted comparing to the permissible time-step of implicit schemes. However, the explicit methods have the advantage of being simpler to construct and implement in the computer programs. Programs for implicit schemes will involve solving a fairly large system of linear equations, demanding attention to efficiency and accuracy. Thus we select the explicit schemes, as numerical methods for the moment system are not our current focus.

Another concern, also about the suitability of explicit methods, is the stiffness caused by the relaxation time τ in the source term. There are cases in which the relaxation time τ is significantly smaller than the typical advection time-scale; this will badly restrict the time-step. It is suggested to use the *hybrid* implicit-explicit

approaches, in which the spatial-derivative terms (flux terms or advection terms) are treated explicitly, while the source term is approximated by an implicit discretization. The interested reader is referred to Section 2.5 of [60] for more information. However, it turns out that the advection time-scale of our simulations are significantly smaller than the relaxation time. The computational domains of both Couette and Poiseuille flows are quite small, in the sense that the smallest cell-size is even smaller than the typical value of the mean-free-path, which scales with τ.

Of all the flavors of the Runge-Kutta discretization, we will use the strongly-stability-preserving 2-stage method [22, 55], or SSP2 for short. It is a second-order accurate method and it will be used in combination with both FV and DG discretizations. The one-stage Runge–Kutta method ("forward Euler") cannot be used due to the instability when combined with the $p1$ FV/DG discretizations [16]. When the residual $\mathbf{R}$ is discretized by the $p1$ DG method, which is potentially higher-than-second-order accurate in space, one wonders if it would be better to use a higher-order Runge–Kutta method, such as the 4-stage SSP method. Even though the accuracy of the temporal discretization is not quite relevant, for steady-state problems, a higher-order-accurate one permits a larger time-step, suggesting a shorter running time, owing to the larger CFL number as shown in Table 4.2. However, the CFL number of the RK4 method is only $\sim 40\%$ larger than that of SSP2, which is not enough to compensate for the doubled amount of calculations per time-step (4-stage vs. 2-stage). A higher-order Runge–Kutta method is not useful either when combined with the $p1$ FV discretization, which is only second-order accurate in space.

The SSP2 method is given by

$$\mathbf{U}^{(1)} = \mathbf{U}^n + \Delta t\, \mathbf{R}(\mathbf{U}^n)\,, \tag{4.20a}$$

$$\mathbf{U}^{n+1} = \frac{1}{2}\mathbf{U}^{(1)} + \frac{1}{2}\mathbf{U}^n + \frac{1}{2}\Delta t\, \mathbf{R}\big(\mathbf{U}^{(1)}\big)\,; \tag{4.20b}$$

Table 4.2: The CFL numbers for DG methods using piecewise polynomials of degree p and Runge–Kutta methods of order m (from Table 2.2 of [16, p. 191]).

	$p = 0$ piecewise constant	$p = 1$ piecewise linear
$m = 1$ (forward Euler, 1-stage)	1.000	unstable
$m = 2$ (SSP2 or RK21 [9, p. 94], 2-stage)	1.000	0.333
$m = 3$ (SSP3, 3-stage)	1.256	0.409
$m = 4$ (RK4, 4-stage)	1.392	0.464

or equivalently, but not as memory-efficient because we need to store the initial residual:

$$\mathbf{U}^{(1)} = \mathbf{U}^n + \Delta t\, \mathbf{R}(\mathbf{U}^n)\,, \tag{4.21a}$$

$$\mathbf{U}^{n+1} = \mathbf{U}^n + \frac{1}{2}\Delta t\Big[\mathbf{R}(\mathbf{U}^n) + \mathbf{R}\big(\mathbf{U}^{(1)}\big)\Big]. \tag{4.21b}$$

4.2.2 Finite-Volume spatial discretization

The FV discretization described here can be used for any moment system having a hyperbolic-relaxation form similarly to Eq. (2.36):

$$\frac{\partial \mathbf{U}\,(t,x,y)}{\partial t} + \frac{\partial \mathbf{F}\,(\mathbf{U})}{\partial x} + \frac{\partial \mathbf{G}\,(\mathbf{U})}{\partial y} = -\frac{1}{\tau\,(\mathbf{U})}\mathbf{S}\,(\mathbf{U}), \tag{4.22}$$

The numerical solution of $\mathbf{U}(t,x,y)$ in cell (i,j) is represented by the following polynomial

$$\underset{(x,y)\in\Omega_{i,j}}{\mathbf{U}(t,x,y) \approx \mathbf{U}_{i,j}(t,x,y)} = \overline{\mathbf{U}}_{i,j}(t) + \overline{\Delta_x \mathbf{U}}_{i,j}(t)\,\frac{x-x_i}{\Delta x_i} + \overline{\Delta_y \mathbf{U}}_{i,j}(t)\,\frac{y-y_j}{\Delta y_j} + \overline{\Delta_{xy} \mathbf{U}}_{i,j}(t)\,\frac{x-x_i}{\Delta x_i}\frac{y-y_j}{\Delta y_j}. \tag{4.23}$$

The first term $\overline{\mathbf{U}}_{i,j}(t)$ is called the cell-average and it is defined by

$$\overline{\mathbf{U}}_{ij}(t) = \frac{1}{V_{i,j}} \iint_{\Omega_{i,j}} \mathbf{U}(t,x,y)\,\mathrm{d}x\,\mathrm{d}y. \tag{4.24}$$

The quantities $\overline{\Delta_x \mathbf{U}}$, $\overline{\Delta_y \mathbf{U}}$, and $\overline{\Delta_{xy} \mathbf{U}}$ are called *undivided* derivatives because they relate to the derivatives of the solution averaged over the cell. With regard to the solution approximation (4.23) we observe that these quantities correspond to exact cell averages:

$$\frac{\overline{\Delta_x \mathbf{U}}_{i,j}}{\Delta x_i} = \frac{1}{V_{i,j}} \iint_{\Omega_{i,j}} \frac{\partial \mathbf{U}_{i,j}}{\partial x} \mathrm{d}x\,\mathrm{d}y, \tag{4.25a}$$

$$\frac{\overline{\Delta_y \mathbf{U}}_{i,j}}{\Delta y_j} = \frac{1}{V_{i,j}} \iint_{\Omega_{i,j}} \frac{\partial \mathbf{U}_{i,j}}{\partial y} \mathrm{d}x\,\mathrm{d}y, \tag{4.25b}$$

$$\frac{\overline{\Delta_{xy} \mathbf{U}}_{i,j}}{\Delta x_i \Delta y_j} = \frac{1}{V_{i,j}} \iint_{\Omega_{i,j}} \frac{\partial^2 \mathbf{U}_{i,j}}{\partial x \partial y} \mathrm{d}x\,\mathrm{d}y. \tag{4.25c}$$

For instance, in the FV discretization the undivided derivatives are not independently updated like the cell-averages. Their values are instead obtained from the cell-averages $\overline{\mathbf{U}}$ in the neighboring cells by procedures named *reconstruction*.

Integrating Eq. (4.22) over the physical domain $\Omega_{i,j}$ yields the following semi-discrete equation

$$\begin{aligned}\frac{\partial \overline{\mathbf{U}}_{i,j}(t)}{\partial t} = &-\frac{1}{V_{i,j}} \underbrace{\int_{I_j} \mathbf{F}(\mathbf{U}(t,x,y))\Big|_{x_{i-1/2}}^{x_{i+1/2}} \mathrm{d}y}_{\text{Boundary integral}} - \frac{1}{V_{i,j}} \underbrace{\int_{I_i} \mathbf{G}(\mathbf{U}(t,x,y))\Big|_{y_{j-1/2}}^{y_{j+1/2}} \mathrm{d}x}_{\text{Boundary integral}} \\ &- \frac{1}{V_{i,j}} \underbrace{\iint_{\Omega_{i,j}} \frac{\mathbf{S}(\mathbf{U}(t,x,y))}{\tau(\mathbf{U}(t,x,y))}\,\mathrm{d}x\,\mathrm{d}y}_{\text{Volume integral}},\end{aligned} \tag{4.26}$$

where $I_i = \left\{x : x \in \left[x_{i-1/2}, x_{i+1/2}\right]\right\}$ and $I_j = \left\{y : y \in \left[y_{j-1/2}, y_{j+1/2}\right]\right\}$. To compute the volume integral, we replace the exact solution $\mathbf{U}(t,x,y)$ by its numerical approximation $\mathbf{U}_{i,j}(t,x,y)$ defined in Eq. (4.23). Then the source integral will be calculated

numerically by Gaussian quadrature, as it is impossible to do it analytically due to the strongly non-linear nature of the fraction $\dfrac{\mathbf{S}}{\tau}$. The interface fluxes can be rewritten as follows:

$$\begin{aligned}\frac{1}{V_{i,j}}\int_{I_j}\mathbf{F}(\mathbf{U}(t,x,y))\Big|_{x_{i-1/2}}^{x_{i+1/2}}\mathrm{d}y &= \frac{1}{V_{i,j}}\int_{I_j}\left[\mathbf{F}_{i+1/2}(t,y)-\mathbf{F}_{i-1/2}(t,y)\right]\mathrm{d}y \\ &= \frac{1}{\Delta x_i}\left[\overline{\mathbf{F}}_{i+1/2}(t)-\overline{\mathbf{F}}_{i-1/2}(t)\right],\end{aligned} \tag{4.27}$$

$$\begin{aligned}\frac{1}{V_{i,j}}\int_{I_i}\mathbf{G}(\mathbf{U}(t,x,y))\Big|_{y_{j-1/2}}^{y_{j+1/2}}\mathrm{d}x &= \frac{1}{V_{i,j}}\int_{I_i}\left[\mathbf{G}_{j+1/2}(t,x)-\mathbf{G}_{j-1/2}(t,x)\right]\mathrm{d}x \\ &= \frac{1}{\Delta y_j}\left[\overline{\mathbf{G}}_{j+1/2}(t)-\overline{\mathbf{G}}_{j-1/2}(t)\right],\end{aligned} \tag{4.28}$$

where $\mathbf{F}_{i\pm1/2}(t,y)$ and $\mathbf{G}_{j\pm1/2}(t,x)$ are notations for $\mathbf{F}\big(t,x_{i\pm1/2},y\big)$ and $\mathbf{G}\big(t,x,y_{j\pm1/2}\big)$ respectively. These averages of interface fluxes are defined by

$$\overline{\mathbf{F}}_{i\pm1/2}(t) = \frac{1}{\Delta y_j}\int_{I_j}\mathbf{F}\big(t,x_{i\pm1/2},y\big)\,\mathrm{d}y, \tag{4.29a}$$

$$\overline{\mathbf{G}}_{j\pm1/2}(t) = \frac{1}{\Delta x_i}\int_{I_i}\mathbf{G}\big(t,x,y_{j\pm1/2}\big)\,\mathrm{d}x. \tag{4.29b}$$

Their calculations will be elaborated further in Section 4.2.4. Equation (4.26) becomes

$$\begin{aligned}\frac{\partial\overline{\mathbf{U}}_{i,j}(t)}{\partial t} = &-\frac{1}{\Delta x_i}\left[\overline{\mathbf{F}}_{i+1/2}(t)-\overline{\mathbf{F}}_{i-1/2}(t)\right]-\frac{1}{\Delta y_j}\left[\overline{\mathbf{G}}_{j+1/2}(t)-\overline{\mathbf{G}}_{j-1/2}(t)\right] \\ &-\frac{1}{V_{i,j}}\iint_{\Omega_{i,j}}\frac{\mathbf{S}}{\tau}\big(\mathbf{U}_{i,j}(t,x,y)\big)\,\mathrm{d}x\,\mathrm{d}y.\end{aligned} \tag{4.30}$$

Computation of undivided derivatives $\overline{\Delta_x\mathbf{U}}_{i,j}$, $\overline{\Delta_y\mathbf{U}}_{i,j}$, and $\overline{\Delta_{xy}\mathbf{U}}_{i,j}$

In order to calculate the undivided x-gradient in an arbitrary cell $\overline{\Delta_x\mathbf{U}}_2$, we need the values of the cell-averages and the cell-sizes of its left and right neighbors, denoted by subscripts 1 and 3. The procedure to calculate $\overline{\Delta_x\mathbf{U}}_2$ from $\big(\overline{\mathbf{U}}_1,\overline{\mathbf{U}}_2,\overline{\mathbf{U}}_3\big)$ and $\Delta x_1,\Delta x_2,\Delta x_3$ is called the *central* reconstruction. We calculate a parabolic $f(x)=$

$a_0 + a_1 x + a_2 x^2$ spanning the three cells that will preserve all cell-averages

$$\int_{I_1} f(x)\,\mathrm{d}x = \Delta x_1 \overline{\mathbf{U}}_1,$$
$$\int_{I_2} f(x)\,\mathrm{d}x = \Delta x_2 \overline{\mathbf{U}}_2,$$
$$\int_{I_3} f(x)\,\mathrm{d}x = \Delta x_3 \overline{\mathbf{U}}_3.$$

Then the undivided gradient is given by

$$\overline{\Delta_x \mathbf{U}}_2 = f\left(x_2 + \frac{\Delta x_2}{2}\right) - f\left(x_2 - \frac{\Delta x_2}{2}\right).$$

For cells adjacent to the solid boundaries, there is no three-cell stencil having the of interest cell at the center. We have to use the *one-sided* reconstruction, in which the of interest cell will either be the left cell (cell 1) or the right cell (cell 3) of the three-cell stencil. The calculation is the same as in central reconstruction,

$$\overline{\Delta_x \mathbf{U}}_1 = f\left(x_1 + \frac{\Delta x_1}{2}\right) - f\left(x_1 - \frac{\Delta x_1}{2}\right),$$
$$\overline{\Delta_x \mathbf{U}}_3 = f\left(x_3 + \frac{\Delta x_3}{2}\right) - f\left(x_3 - \frac{\Delta x_3}{2}\right).$$

The final results are

$$\textit{center}\text{: } \overline{\Delta_x \mathbf{U}}_2 = \Delta x_2 \left[\frac{\Delta x_3 + \Delta x_2/2}{L}\delta_{21} + \frac{\Delta x_1 + \Delta x_2/2}{L}\delta_{32}\right], \tag{4.31a}$$

$$\textit{left}\text{: } \overline{\Delta_x \mathbf{U}}_1 = \Delta x_1 \left[\left(1 + \frac{\Delta x_2 + \Delta x_1/2}{L}\right)\delta_{21} - \frac{\Delta x_2 + \Delta x_1/2}{L}\delta_{32}\right], \tag{4.31b}$$

$$\textit{right}\text{: } \overline{\Delta_x \mathbf{U}}_3 = \Delta x_3 \left[-\frac{\Delta x_2 + \Delta x_3/2}{L}\delta_{21} + \left(1 + \frac{\Delta x_2 + \Delta x_3/2}{L}\right)\delta_{32}\right], \tag{4.31c}$$

with

$$
\begin{aligned}
L &= \Delta x_1 + \Delta x_2 + \Delta x_3, \\
\delta_{21} &= \frac{2\left(\overline{\mathbf{U}}_2 - \overline{\mathbf{U}}_1\right)}{\Delta x_1 + \Delta x_2}, \\
\delta_{32} &= \frac{2\left(\overline{\mathbf{U}}_3 - \overline{\mathbf{U}}_2\right)}{\Delta x_2 + \Delta x_3}.
\end{aligned}
$$

The calculation of the undivided y-gradient is fundamentally identical. After having obtained the values of $\overline{\Delta_x \mathbf{U}}$ and $\overline{\Delta_y \mathbf{U}}$ for all cells in the computational domain, we then compute the values of $\overline{\Delta_{xy} \mathbf{U}}$. Assuming we need the value of $\overline{\Delta_{xy} \mathbf{U}}_{i,j}$, we first calculate

$$
\begin{aligned}
\overline{\Delta_{xy} \mathbf{U}}^{(1)}_{i,j} &= \text{central reconstruction } \left(\overline{\Delta_x \mathbf{U}}_{i,j-1}, \overline{\Delta_x \mathbf{U}}_{i,j}, \overline{\Delta_x \mathbf{U}}_{i,j+1}\right), \\
\overline{\Delta_{xy} \mathbf{U}}^{(2)}_{i,j} &= \text{central reconstruction } \left(\overline{\Delta_y \mathbf{U}}_{i-1,j}, \overline{\Delta_y \mathbf{U}}_{i,j}, \overline{\Delta_y \mathbf{U}}_{i+1,j}\right).
\end{aligned}
$$

Then $\overline{\Delta_{xy} \mathbf{U}}_{i,j}$ is the average those two values:

$$
\overline{\Delta_{xy} \mathbf{U}}_{i,j} = \frac{\overline{\Delta_{xy} \mathbf{U}}^{(1)}_{i,j} + \overline{\Delta_{xy} \mathbf{U}}^{(2)}_{i,j}}{2}.
$$

Normally for a compressible flow with shock waves, it is necessary to "limit" the values of the reconstructed $\overline{\Delta_{(\cdot)} \mathbf{U}}$ to avoid spurious oscillations in the numerical solutions. This is unnecessary for our simulations, however, due to the smoothness of Couette- and Poiseuille-flow solutions. Our numerical experiments with Couette flow indeed shows no meaningful enhancement when a limiter (the *minmod* limiter) is used.

4.2.3 Discontinuous Galerkin spatial discretization

In the $p1$ DG discretization we employ, the numerical approximation of the true solution $\mathbf{U}(t,x,y)$ is a polynomial constructed from the Legendre-polynomial full-tensor basis

$$\begin{aligned}\underset{(x,y)\in\Omega_{i,j}}{\mathbf{U}(t,x,y)} \approx \mathbf{U}_{i,j}(t,x,y) &= \sum_{\alpha,\beta=0}^{1} \mathbf{a}_{i,j}^{\alpha\beta}(t)\,\phi_{i,j}^{\alpha\beta}(x,y) \\ &= \mathbf{a}_{i,j}^{00}(t)\,\phi_{i,j}^{00} + \mathbf{a}_{i,j}^{10}(t)\,\phi_{i,j}^{10}(x) + \mathbf{a}_{i,j}^{01}(t)\,\phi_{i,j}^{01}(y) + \mathbf{a}_{i,j}^{11}(t)\,\phi_{i,j}^{11}(x,y)\,, \quad (4.32)\end{aligned}$$

where

$$\phi_{i,j}^{00} = 1, \quad (4.33a)$$

$$\phi_{i,j}^{10}(x) = \frac{x-x_i}{\Delta x_i}, \quad (4.33b)$$

$$\phi_{i,j}^{01}(y) = \frac{y-y_j}{\Delta y_j}, \quad (4.33c)$$

$$\phi_{i,j}^{11}(x,y) = \frac{x-x_i}{\Delta x_i}\frac{y-y_j}{\Delta y_j}. \quad (4.33d)$$

These Legendre polynomials are orthogonal

$$\iint_{\Omega_{i,j}} \phi_{i,j}^{\alpha_1\beta_1}(x,y)\,\phi_{i,j}^{\alpha_2\beta_2}(x,y)\,\mathrm{d}x\,\mathrm{d}y = \begin{cases} 0 & \text{if } (\alpha_1,\beta_1) \neq (\alpha_2,\beta_2) \\ \dfrac{V_{i,j}}{12^{\alpha_1+\beta_1}} & \text{if } (\alpha_1,\beta_1) \equiv (\alpha_2,\beta_2) \end{cases} \quad (4.34)$$

which leads to the following result:

$$\iint_{\Omega_{i,j}} \phi_{i,j}^{\alpha\beta}(x,y)\,\mathbf{U}_{i,j}(t,x,y)\,\mathrm{d}x\,\mathrm{d}y = \frac{V_{i,j}}{12^{\alpha+\beta}}\mathbf{a}_{i,j}^{\alpha\beta}(t)\,. \quad (4.35)$$

When comparing Eq. (4.32) to Eq. (4.23), it is clear that the coefficients $\mathbf{a}_{i,j}^{\alpha\beta}$ represent the same type of information as the cell-average $\overline{\mathbf{U}}_{i,j}$ and the undivided derivatives $\overline{\Delta_{(\cdot)}\mathbf{U}}_{i,j}$ in the $p1$ FV discretization. Unlike in the FV discretization, each

of the $\mathbf{a}_{i,j}^{\alpha\beta}$ terms will be updated by its dedicated update equation, which amounts to a total of *four* update equations in this case. In general the number of the update equations is $(p+1)^2$ in two-dimensional space and $(p+1)^3$ in three-dimensional space. This number increases rapidly when we want to represent the exact solution by higher-order polynomials. Conversely, the number of the update equations in the FV discretization is always *one*; a higher-order representation means it is necessary to reconstruct additional higher-order undivided derivatives from the cell-averages. The computational stencil will have to grow bigger, including "neighbors" of the immediate neighbors, while that of the DG discretization stays unchanged.

To find update equations for $\mathbf{a}_{i,j}^{\alpha\beta}$ we multiply Eq. (4.22) by the basis functions spanning the cell (i,j), then integrate over the domain $\Omega_{i,j}$ to the semi-discrete form

$$\frac{\partial}{\partial t}\iint_{\Omega_{i,j}} \phi_{i,j}(x,y)\,\mathbf{U}(t,x,y)\;\mathrm{d}x\,\mathrm{d}y = -\iint_{\Omega_{i,j}} \phi_{i,j}(x,y)\,\frac{\partial \mathbf{F}(\mathbf{U})}{\partial x}\,\mathrm{d}x\,\mathrm{d}y - \iint_{\Omega_{i,j}} \phi_{i,j}(x,y)\,\frac{\partial \mathbf{G}(\mathbf{U})}{\partial y}\,\mathrm{d}x\,\mathrm{d}y - \iint_{\Omega_{i,j}} \phi_{i,j}(x,y)\,\frac{\mathbf{S}(\mathbf{U})}{\tau(\mathbf{U})}\,\mathrm{d}x\,\mathrm{d}y; \quad (4.36)$$

applying integration by parts on the flux terms, we obtain the following form:

$$\begin{aligned}\frac{\partial}{\partial t}\iint_{\Omega_{i,j}} \phi_{i,j}(x,y)\,\mathbf{U}(t,x,y)\;\mathrm{d}x\,\mathrm{d}y = \\ -\left[\int_{I_j} \phi_{i,j}(x,y)\,\mathbf{F}(\mathbf{U})\,\Big|_{x_{i-1/2}}^{x_{i+1/2}}\mathrm{d}y - \iint_{\Omega_{i,j}} \frac{\partial \phi_{i,j}(x,y)}{\partial x}\mathbf{F}(\mathbf{U})\;\mathrm{d}x\,\mathrm{d}y\right] \\ -\left[\int_{I_i} \phi_{i,j}(x,y)\,\mathbf{G}(\mathbf{U})\,\Big|_{y_{j-1/2}}^{y_{j+1/2}}\mathrm{d}x - \iint_{\Omega_{i,j}} \frac{\partial \phi_{i,j}(x,y)}{\partial y}\mathbf{G}(\mathbf{U})\;\mathrm{d}x\,\mathrm{d}y\right] \\ - \iint_{\Omega_{i,j}} \phi_{i,j}(x,y)\,\frac{\mathbf{S}(\mathbf{U})}{\tau(\mathbf{U})}\,\mathrm{d}x\,\mathrm{d}y. \quad (4.37)\end{aligned}$$

Substituting the expressions for the basis functions from Eq. (4.33) we obtain the following semi-discrete equations for $\mathbf{a}_{i,j}^{\alpha\beta}$.

- $\phi_{i,j}(x,y) = \phi_{i,j}^{00} = 1$: the equation for $\mathbf{a}_{i,j}^{00}$

$$V_{i,j}\,\frac{\partial \mathbf{a}_{i,j}^{00}(t)}{\partial t} = -\underbrace{\int_{I_j}\Big(\mathbf{F}_{i+1/2}(t,y) - \mathbf{F}_{i-1/2}(t,y)\Big)\mathrm{d}y}_{\text{Boundary integral}} - \underbrace{\int_{I_i}\Big(\mathbf{G}_{j+1/2}(t,x) - \mathbf{G}_{j-1/2}(t,x)\Big)\mathrm{d}x}_{\text{Boundary integral}} - \underbrace{\iint_{\Omega_{i,j}} \frac{\mathbf{S}}{\tau}(\mathbf{U})\;\mathrm{d}x\,\mathrm{d}y}_{\text{Volume integral}}; \quad (4.38)$$

- $\phi_{i,j}(x,y) = \phi_{i,j}^{10}(x) = \dfrac{x - x_i}{\Delta x_i}$: the equation for $\mathbf{a}_{i,j}^{10}$

$$\frac{V_{i,j}}{12}\,\frac{\partial \mathbf{a}_{i,j}^{10}(t)}{\partial t} = -\frac{1}{2}\underbrace{\int_{I_j}\Big(\mathbf{F}_{i+1/2}(t,y) + \mathbf{F}_{i-1/2}(t,y)\Big)\mathrm{d}y}_{\text{Boundary integral}} - \underbrace{\int_{I_i}\phi_{i,j}^{10}(x)\,\Big(\mathbf{G}_{j+1/2}(t,x) - \mathbf{G}_{j-1/2}(t,x)\,\Big)\mathrm{d}x}_{\text{Boundary integral}} + \underbrace{\frac{1}{\Delta x_i}\iint_{\Omega_{i,j}}\mathbf{F}(\mathbf{U})\,\mathrm{d}x\,\mathrm{d}y}_{\text{Volume integral}} - \underbrace{\iint_{\Omega_{i,j}}\phi_{i,j}^{10}(x)\,\frac{\mathbf{S}}{\tau}(\mathbf{U})\;\mathrm{d}x\,\mathrm{d}y}_{\text{Volume integral}}; \quad (4.39)$$

- $\phi_{i,j}(x,y) = \phi_{i,j}^{01}(y) = \dfrac{y - y_j}{\Delta y_j}$: the equation for $\mathbf{a}_{i,j}^{01}$

$$\frac{V_{i,j}}{12}\,\frac{\partial \mathbf{a}_{i,j}^{01}(t)}{\partial t} = -\underbrace{\int_{I_j}\phi_{i,j}^{01}(y)\,\Big(\mathbf{F}_{i+1/2}(t,y) - \mathbf{F}_{i-1/2}(t,y)\,\Big)\mathrm{d}y}_{\text{Boundary integral}} - \frac{1}{2}\underbrace{\int_{I_i}\Big(\mathbf{G}_{j+1/2}(t,x) + \mathbf{G}_{j-1/2}(t,x)\Big)\mathrm{d}x}_{\text{Boundary integral}} + \frac{1}{\Delta y_j}\underbrace{\iint_{\Omega_{i,j}}\mathbf{G}(\mathbf{U})\,\mathrm{d}x\,\mathrm{d}y}_{\text{Volume integral}} - \underbrace{\iint_{\Omega_{i,j}}\phi_{i,j}^{01}(y)\,\frac{\mathbf{S}}{\tau}(\mathbf{U})\;\mathrm{d}x\,\mathrm{d}y}_{\text{Volume integral}}; \quad (4.40)$$

- $\phi_{i,j}(x,y) = \phi^{11}_{i,j}(x,y) = \dfrac{x-x_i}{\Delta x_i}\dfrac{y-y_j}{\Delta y_j}$: the equation for $\mathbf{a}^{11}_{i,j}$

$$\begin{aligned}\frac{V_{i,j}}{144}\frac{\partial \mathbf{a}^{11}_{i,j}(t)}{\partial t} = &-\frac{1}{2}\underbrace{\int_{I_j}\phi^{01}_{i,j}(y)\left(\mathbf{F}_{i+1/2}(t,y)+\mathbf{F}_{i-1/2}(t,y)\right)\mathrm{d}y}_{\text{Boundary integral}}\\ &-\frac{1}{2}\underbrace{\int_{I_i}\phi^{10}_{i,j}(x)\left(\mathbf{G}_{j+1/2}(t,x)+\mathbf{G}_{j-1/2}(t,x)\right)\mathrm{d}x}_{\text{Boundary integral}}\\ &+\frac{1}{\Delta x_i}\underbrace{\iint_{\Omega_{i,j}}\phi^{01}_{i,j}(y)\,\mathbf{F}(\mathbf{U})\,\mathrm{d}x\,\mathrm{d}y}_{\text{Volume integral}}+\frac{1}{\Delta y_j}\underbrace{\iint_{\Omega_{i,j}}\phi^{10}_{i,j}(x)\,\mathbf{G}(\mathbf{U})\,\mathrm{d}x\,\mathrm{d}y}_{\text{Volume integral}}\\ &-\underbrace{\iint_{\Omega_{i,j}}\phi^{11}_{i,j}(x,y)\,\frac{\mathbf{S}}{\tau}(\mathbf{U})\;\mathrm{d}x\,\mathrm{d}y}_{\text{Volume integral}}. \end{aligned} \tag{4.41}$$

The calculation procedure for the volume integrals is similar to those used for the FV discretization. We substitute $\mathbf{U}_{i,j}(t,x,y)$ defined by Eq. (4.32) for the exact solution $\mathbf{U}(t,x,y)$ in the volume-integral terms. The expressions for the basis function $\phi^{\alpha\beta}_{i,j}(x,y)$ are given by Eq. (4.33). The variance within cell (i,j) of the integrands of the volume-integral terms is now fully described. Due to the complexity of the expressions, it is not practical to integrate the volume integrals analytically; instead, they will be computed approximately by Gaussian quadrature.

4.2.4 Boundary integrals of the interface fluxes

The boundary-integral terms of both the FV and DG discretizations have the following general forms

$$x\text{-interface-terms} \qquad \int_{I_j} f(y)\,\mathbf{F}_{i+1/2}(t,y)\,\mathrm{d}y, \tag{4.42a}$$

$$y\text{-interface-terms} \qquad \int_{I_i} g(x)\,\mathbf{G}_{j+1/2}(t,x)\,\mathrm{d}x. \tag{4.42b}$$

It is sufficient to elaborate upon the boundary integrals of the x-interface-terms as Eq. (4.42a) and Eq. (4.42b) are fundamentally identical. These integrals will also be computed approximately by Gaussian quadrature, which will require value of $\mathbf{F}$ at Gaussian points along the $\left(i+\frac{1}{2}\right)$-interface. The interface flux at an arbitrary Gaussian point $y = y_0$ is the solution of a Riemann problem, of which the inputs are the values of the conservative flow variables on the left and right sides of the interface

$$\begin{aligned}\mathbf{F}_{i+1/2}(t, y_0) &= \text{Riemann}\left(\mathbf{U}^{\text{L}}, \mathbf{U}^{\text{R}}\right) \\ &= \text{Riemann}\Big(\mathbf{U}_{i,j}\left(t, x_{i+1/2}, y_0\right), \mathbf{U}_{i+1,j}\left(t, x_{i+1/2}, y_0\right)\Big),\end{aligned} \tag{4.43}$$

where $\mathbf{U}_{i,j}(t, x, y)$ and $\mathbf{U}_{i+1,j}(t, x, y)$ have the general piecewise-linear form defined by Eq. (4.23) (in the FV discretization) or Eq. (4.32) in the DG discretization.

For the Euler system, assuming a perfect gas law, we can solve the Riemann problem analytically by an exact Riemann solver, or approximately by approximate Riemann solvers, such as the HLL solver [27] or Roe's solver [48]. For the moment systems, the exact Riemann solver will not be used, as ***a)*** it does not currently exist for a general moment system; and ***b)*** even if there existed one, it is justifiable to use the approximate Riemann solvers because these are more efficient and the governing systems are solved approximately by numerical discretizations anyway. There have been efforts to extend the approximate Riemann solvers for the Euler system to moment systems, such as the adaptation of Roe's solver to the 10-moment and 35-moment systems presented in Brown's dissertation [8]. The distinct difficulty in this approach is that it depends crucially on knowledges about the eigenvalues and eigenvectors of the Jacobian matrices of the flux functions $\dfrac{\partial \mathbf{F}^{(\alpha)}}{\partial \mathbf{U}}$. They are to be calculated analytically or numerically, which would become *generally impossible* (analytical calculation) or *expensive* (numerical calculation) due to the large dimensions of the Jacobian matrices if the governing system has more moments, i.e., 13 or more.

It is possible to circumvent knowing the Jacobian eigenstructure by taking ad-

vantage of how the fluxes are constructed in the moment system. As presented in Section 2.1.3, the α-direction flux function, $\mathbf{F}^{(\alpha)}$, is the moment of the distribution function with the appropriate weight $\mathbf{W}(\mathbf{v})$,

$$\mathbf{F}^{(\alpha)}(t,\mathbf{x}) = \iiint_{-\infty}^{+\infty} v_\alpha \mathbf{W}(\mathbf{v})\, f(t,\mathbf{x},\mathbf{v})\,\mathrm{d}\mathbf{v}. \tag{4.44}$$

It is recognized, at an interface, that the contribution of the left cell to the interface flux is carried by the right-moving molecules; conversely, the right cell's contribution is carried by the left-moving molecules. Thus, the interface flux is split into two half-v_x-space integrals,

$$\begin{aligned}\mathbf{F}_{i+1/2}(t,y_0) = &\iint_{-\infty}^{+\infty}\left(\int_{-\infty}^{0} v_x \mathbf{W}(\mathbf{v})\, f^{\mathrm{R}}(\mathbf{v})\,\mathrm{d}v_x\right)\mathrm{d}v_y\,\mathrm{d}v_z \\ &+ \iint_{-\infty}^{+\infty}\left(\int_{0}^{+\infty} v_x \mathbf{W}(\mathbf{v})\, f^{\mathrm{L}}(\mathbf{v})\,\mathrm{d}v_x\right)\mathrm{d}v_y\,\mathrm{d}v_z,\end{aligned} \tag{4.45}$$

where the distribution functions $f^{\mathrm{L}}(\mathbf{v})$ and $f^{\mathrm{R}}(\mathbf{v})$ are constructed from $\mathbf{U}^{\mathrm{L}}$ and $\mathbf{U}^{\mathrm{R}}$, respectively. We call this approximate Riemann solver a *kinetic* flux-vector splitting—KFVS (or Boltzmann solver, in the terminology of [27]). In concept, it is similar to the *equilibrium flux method* (EFM) by Pullin [47] and the *beam scheme* by Sanders and Prendergast [50]. The *potential* disadvantages of this method are that ***a)*** it requires an *explicit relation* between the distribution function and the flow variables; and ***b)*** the expression better be *analytically integrable* with various weight functions in the half-velocity space, otherwise the numerical integration would have to be used, which would be costly because of the semi-infinite domain.

Fortunately, for Grad's 13-moment system, the relation between the $f_{\mathrm{Grad13M}}(\mathbf{v})$ distribution and the flow variables is explicitly defined by Eq. (2.30). In two dimen-

sions, the weight-function vector is defined by:

$$\mathbf{W}(\mathbf{v}) = \left[1, v_x, v_y, v_x^2, v_y^2, v_z^2, v_x v_y, v_x \mathbf{v}^2, v_y \mathbf{v}^2\right]. \tag{4.46}$$

Furthermore, the half-velocity-space integrals in Eq. (4.45) are perfectly analytically integrable, owing to the simplicity of the Maxwellian distribution function, of which Grad's 13-moment distribution function is a perturbation. The solutions for those integrals are shown in Appendix B. Thus, all necessary "ingredients" for the calculations of boundary integrals, Eq. (4.42), are available.

4.2.5 Restriction on time-step Δt

The allowable time-step in each cell, $\Delta t_{i,j}$, is the minimum of the advection time-step and the relaxation time-step. The global time-step used in update equations is the minimum of $\Delta t_{i,j}$,

$$\begin{aligned} \Delta t &= \min_{i,j} \left(\min\left(\Delta t_{ai,j}, \overline{\tau}_{i,j}\right) \right) \\ &= \min \left(\min_{i,j}\left(\Delta t_{ai,j}\right), \min_{i,j}\left(\overline{\tau}_{i,j}\right) \right). \end{aligned} \tag{4.47}$$

The advection time-step in cell (i, j) is calculated by the following equation

$$\Delta t_{ai,j} = \frac{CFL}{\dfrac{\max\left(\left|\boldsymbol{\lambda}_{xi,j}\right|\right)}{\Delta x_i} + \dfrac{\max\left(\left|\boldsymbol{\lambda}_{y_{i,j}}\right|\right)}{\Delta y_j}}, \tag{4.48}$$

where $\boldsymbol{\lambda}_{xi,j}$ and $\boldsymbol{\lambda}_{y_{i,j}}$ are the vectors of signal speeds in the x-flux and y-flux respectively. They are the eigenvalues of the Jacobian matrices $\dfrac{\partial \mathbf{F}}{\partial \mathbf{U}}$ and $\dfrac{\partial \mathbf{G}}{\partial \mathbf{U}}$, which are not calculated in the KFVS approximate Riemann solver. However, we only need their maximum value and it is only used for stability purposes. Since its value does not play any role in the accuracy of the numerical method, a rough estimation is

adequate. It is known from Grad [25] that the fastest *equilibrium* eigenvalues of the one-dimensional 13M system have the form of $u_x \pm 1.65a$, where a is the speed of sound. It is, therefore, reasonable to assume that the maximum of the eigenvalues, of any moment system in *nonequilibrium* flows is approximated by $|u_x| + c_a a$. Then Eq. (4.48) becomes

$$\Delta t_{a\,i,j} = \frac{CFL}{\dfrac{\left|\overline{u_x}_{i,j}\right| + c_a \overline{a}_{i,j}}{\Delta x_i} + \dfrac{\left|\overline{u_y}_{i,j}\right| + c_a \overline{a}_{i,j}}{\Delta y_j}}, \tag{4.49}$$

where the average sound speed is calculated from the average temperature,

$$\overline{a}_{i,j} = \sqrt{\gamma R \overline{T}_{i,j}}\,.$$

For the 13M system we use $c_a = 2$, and the value of the *CFL* number is 0.3.

The average relaxation time in cell (i, j) is also calculated from the averages of the flow quantities:

$$\overline{\tau}_{i,j} = \frac{\overline{\mu}_{i,j}}{\overline{p}_{i,j}} = \frac{\mu_{\text{ref}}}{(T_{\text{ref}})^{\omega}} \frac{\left(\overline{T}_{i,j}\right)^{\omega}}{\overline{p}_{i,j}}, \tag{4.50}$$

in which a power law for the temperature-dependence of viscosity is used

$$\mu = \mu_{\text{ref}} \left(\frac{T}{T_{\text{ref}}}\right)^{\omega}. \tag{4.51}$$

For Argon gas, $\omega = 0.72$, $T_{\text{ref}} = 273\text{K}$, and $\mu_{\text{ref}} = 2.125 \times 10^{-5}\text{Ns/m}^2$, values taken from Table 2-1 [69, p. 29].

4.3 Numerical methods for the BGK equation

4.3.1 Reduction approach

The BGK equation introduced in Section 2.1 is expensive to solve numerically due to a large number of independent variables. For a 2-D flow geometry, it has the following form,

$$\frac{\partial f}{\partial t} + v_x \frac{\partial f}{\partial x} + v_y \frac{\partial f}{\partial y} = -\frac{f - f_{\mathrm{M}}}{\tau}, \tag{4.52}$$

where f is a function of six independent variables (t, x, y, v_x, v_y, v_z). We are not interested in the z-direction, as every flow quantity is assumed uniform in that direction. However, when Eq. (4.52) is solved numerically, the v_z-dimension still has to be discretized by division into N_{v_z} small intervals; the phase-space mesh is N_{v_z} times larger than necessary, and makes an already expensive calculation almost prohibitive.

To make the calculation more feasible, we utilize the *reduction approach* proposed by Chu [14, 15]. Instead of solving a *single* equation that defined in five-dimensional phase space (x, y, v_x, v_y, v_z), we solve a system of *two* equations having a similar mathematical form but depending only on a 4-D phase space (x, y, v_x, v_y). We don't have to discretize the v_z-dimension, saving us at the very least an order of magnitude in terms of grid size, while the number of the governing equations only doubles. The system to solve is

$$\frac{\partial \boldsymbol{\Phi}}{\partial t} + v_x \frac{\partial \boldsymbol{\Phi}}{\partial x} + v_y \frac{\partial \boldsymbol{\Phi}}{\partial y} = -\frac{\boldsymbol{\Phi} - \boldsymbol{\Phi}_{\mathrm{M}}}{\tau} \tag{4.53}$$

where the reduced distribution functions $\boldsymbol{\Phi} = (\Phi_0, \Phi_1)$ are functions of only *five* independent variables (t, x, y, v_x, v_y). Equation (4.53) will be called "reduced system of the BGK equation", or just "reduced system" for short. The components of $\boldsymbol{\Phi}$ are related to the original distribution function of the BGK equation by the following

integrals:

$$\begin{bmatrix} \Phi_0 \\ \Phi_1 \end{bmatrix} = \int_{-\infty}^{+\infty} \begin{bmatrix} 1 \\ v_z^2 \end{bmatrix} f(t, x, y, v_x, v_y, v_z)\, \mathrm{d}v_z. \tag{4.54}$$

The quantities Φ_0 and Φ_1 carry information about mass density and total energy in the z-direction, respectively. The *reduced* Maxwellian distribution functions $\mathbf{\Phi}_\mathrm{M} = (\Phi_{0\mathrm{M}}, \Phi_{1\mathrm{M}})$ are calculated using Eq. (4.54) and Eq. (2.15),

$$\Phi_{0\mathrm{M}}(t, x, y, v_x, v_y) = \frac{\rho}{2\pi RT} \exp\left[-\frac{(v_x - u_x)^2 + (v_y - u_y)^2}{2RT}\right], \tag{4.55a}$$

$$\Phi_{1\mathrm{M}}(t, x, y, v_x, v_y) = \frac{RT}{2}\Phi_{0\mathrm{M}} = \frac{\rho}{4\pi} \exp\left[-\frac{(v_x - u_x)^2 + (v_y - u_y)^2}{2RT}\right]; \tag{4.55b}$$

the quantities ρ, T, u_x, and u_y are functions of time and physical space.

The conservative variables of the 2-D 13M system are calculated from linear combination of the corresponding moments of $\mathbf{\Phi}$ as shown below

$$\mathbf{U} = \iiint_{-\infty}^{+\infty} \begin{bmatrix} 1 \\ v_x \\ v_y \\ v_x^2 \\ v_y^2 \\ v_z^2 \\ v_x v_y \\ v_x \mathbf{v}^2 \\ v_y \mathbf{v}^2 \end{bmatrix} f\, \mathrm{d}\mathbf{v} = \iint_{-\infty}^{+\infty} \begin{bmatrix} \Phi_0 \\ v_x \Phi_0 \\ v_y \Phi_0 \\ v_x^2 \Phi_0 \\ v_y^2 \Phi_0 \\ \Phi_1 \\ v_x v_y \Phi_0 \\ v_x \left(v_x^2 + v_y^2\right) \Phi_0 + v_x \Phi_1 \\ v_y \left(v_x^2 + v_y^2\right) \Phi_0 + v_y \Phi_1 \end{bmatrix} \mathrm{d}v_x \mathrm{d}v_y. \tag{4.56}$$

One important thing to note is that the reduction approach is not useful for a three-dimensional flow, as v_z-related moments will definitely be among the flow variables, such as $\iiint v_x v_z f \mathrm{d}\mathbf{v}$.

Just as for the moment system, we will use the semi-discrete method to solve Eq. (4.53) with the Runge–Kutta method used as the temporal discretization. For the spatial discretization, both piecewise-linear FV and DG methods are utilized.

4.3.2 Computational grid of the velocity space

Since $\mathbf{\Phi}$ is a function of time and phase space, the residual $\mathbf{R}$ in Eq. (4.19) contains the discretization of $\mathbf{\Phi}$ in the four-dimensional space (x, y, v_x, v_y). Contrary to the physical space, the velocity space is not limited, spanning the space between $-\infty$ and $+\infty$. It is necessary to truncate the space to a finite square domain centering at the bulk velocity (u_x, u_y). The distance from the centroid to the boundary equals a *few* thermal speeds [3, Section 3.1], which is proportional to the sound speed. The truncated space has to be large enough make the contribution from the ignored space negligible. For example, consider the one-dimensional Maxwellian distribution function defined as

$$f_{\mathrm{M}}^{\text{1-D}}(v_x) = \frac{\rho}{\sqrt{2\pi RT}} \exp\left[-\frac{(v_x - u_x)^2}{2RT}\right]; \tag{4.57}$$

the original infinite domain of v_x is limited to $[u_x - na, u_x + na]$ with the sound speed of monatomic gas given by $a = \sqrt{\gamma RT} = \sqrt{5RT/3}$. The value of n is calculated from condition that $f_{\mathrm{M}}^{\mathrm{1D}}(v_x)$ over the truncated domain still conserves the original mass, x-momentum and energy within computer round-off. The relative differences between

Table 4.3: The relative differences of mass, momentum, and energy between the infinite and truncated velocity spaces of the 1-D Maxwellian distribution function.

n	mass	energy ($M = 0$)	energy ($M = 20$)
2	9.823×10^{-3}	8.332×10^{-2}	9.933×10^{-3}
5	1.082×10^{-10}	4.722×10^{-9}	1.151×10^{-10}
6.5	4.801×10^{-17}	3.476×10^{-15}	5.315×10^{-17}
7	1.611×10^{-19}	1.347×10^{-17}	1.810×10^{-19}

the infinite and truncated spaces are given by

$$\text{mass:} \quad 1 - \frac{\int_{u_x-na}^{u_x+na} f_{\mathrm{M}}^{1\mathrm{D}}(v_x)\,\mathrm{d}v_x}{\int_{-\infty}^{+\infty} f_{\mathrm{M}}^{1\mathrm{D}}(v_x)\,\mathrm{d}v_x} = 1 - \operatorname{erf}\left[n\sqrt{\frac{5}{6}}\right], \tag{4.58}$$

$$\text{momentum:} \quad 1 - \frac{\int_{u_x-na}^{u_x+na} v_x f_{\mathrm{M}}^{1\mathrm{D}}(v_x)\,\mathrm{d}v_x}{\int_{-\infty}^{+\infty} v_x f_{\mathrm{M}}^{1\mathrm{D}}(v_x)\,\mathrm{d}v_x} = 1 - \operatorname{erf}\left[n\sqrt{\frac{5}{6}}\right], \tag{4.59}$$

$$\text{energy:} \quad 1 - \frac{\int_{u_x-na}^{u_x+na} \frac{v_x^2}{2} f_{\mathrm{M}}^{1\mathrm{D}}(v_x)\,\mathrm{d}v_x}{\int_{-\infty}^{+\infty} \frac{v_x^2}{2} f_{\mathrm{M}}^{1\mathrm{D}}(v_x)\,\mathrm{d}v_x} = 1 - \operatorname{erf}\left[n\sqrt{\frac{5}{6}}\right] + \frac{3n}{3+5M^2}\sqrt{\frac{10}{3\pi}}\exp\left[-\frac{5n^2}{6}\right], \tag{4.60}$$

with Mach number $M = u_x/a$. Table 4.3 shows that the smallest value of n that make all relative differences smaller than 10^{-16} is 7, which will be used in our simulations.

In the truncated velocity space denoted $\Omega_{\mathbf{v}}$, the v_x-dimension will be divided into N_{v_x} equal intervals of size Δv_x; similarly the v_y-dimension will be divided into N_{v_y} uniform intervals of size Δv_y. We reserve the notation (k, l) exclusively for indexing the (v_x, v_y)-location the velocity cells. A typical velocity cell and its neighbors are shown in Fig. 4.3. The phase-space cell (i, j, k, l) will span the product of the physical domain $\Omega_{i,j}$ and the velocity domain $\Omega_{k,l}$, $\Omega_{i,j,k,l} = \Omega_{i,j} \times \Omega_{k,l}$; its volume is

$$V_{i,j,k,l} = V_{i,j}V_{k,l} = \Delta x_i \Delta y_j \Delta v_{xk} \Delta v_{yl}.$$

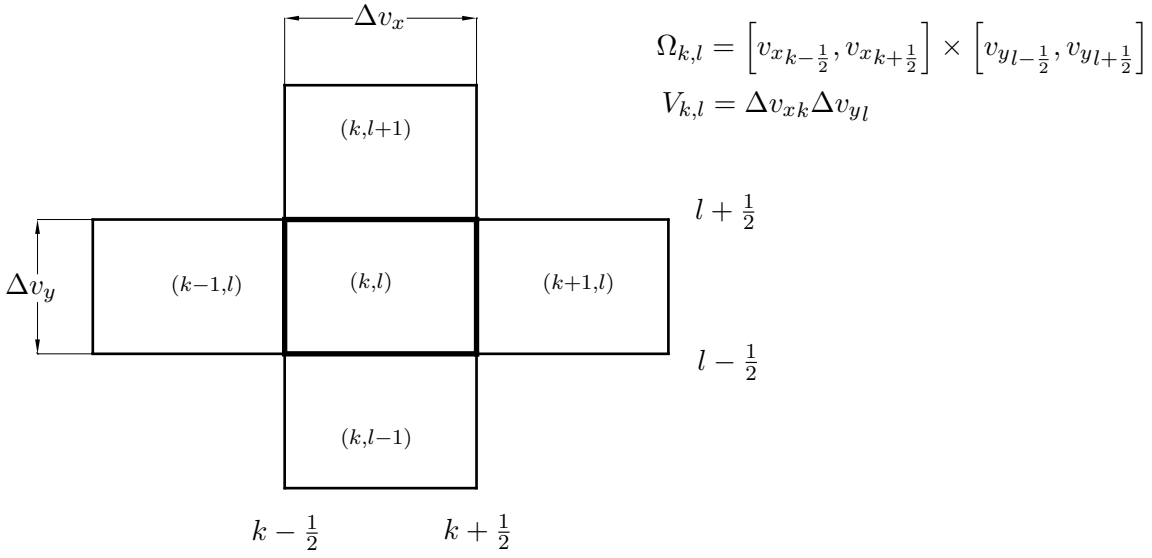

Figure 4.3: Configuration of the computational cells of the Cartesian velocity-mesh in two dimensions. Index k indicates the v_x-coordinate, while l will be used exclusively for the v_y-coordinate.

For simplicity, the velocity grid is kept unchanged in the physical space. Therefore, the truncated velocity space has to be sufficiently large to account for the possible range of the flow's temperature and velocities. The bounds of the velocity space are calculated as follows:

$$\left[\min_{x,y}(u_x) - 7\sqrt{\gamma R \max_{x,y}(T)}\right] \leq v_x \leq \left[\max_{x,y}(u_x) - 7\sqrt{\gamma R \max_{x,y}(T)}\right],$$
$$\left[\min_{x,y}(u_y) - 7\sqrt{\gamma R \max_{x,y}(T)}\right] \leq v_y \leq \left[\max_{x,y}(u_y) - 7\sqrt{\gamma R \max_{x,y}(T)}\right].$$

For Couette and Poiseuille flows in the laminar incompressible regime, the flow's temperature does not change significantly from the wall temperature T^{w}. The vertical velocity $u_y(y)$ is essentially zero in both flows. The Mach number is small for the flows to remain incompressible, thus we also assume $\max(u_x) = \min(u_x) \approx 0$.

4.3.3 Finite-Volume discretization of the reduced system of the BGK equation

Differently from the traditional piecewise-linear FV discretization, the reduced distribution functions in a phase-space cell (i, j, k, l) are approximated by the following polynomial based on an expanded basis:

$$\begin{aligned}\underset{(x,y,v_x,v_y)\in\Omega_{i,j,k,l}}{\boldsymbol{\Phi}(t,x,y,v_x,v_y)} &\approx \boldsymbol{\Phi}_{i,j,k,l}(t,x,y,v_x,v_y)\\ &= \overline{\boldsymbol{\Phi}}_{i,j,k,l}(t) + \overline{\Delta_x\boldsymbol{\Phi}}_{i,j,k,l}(t)\,\frac{x-x_i}{\Delta x_i} + \overline{\Delta_y\boldsymbol{\Phi}}_{i,j,k,l}(t)\,\frac{y-y_j}{\Delta y_j}\\ &\quad + \overline{\Delta_{v_x}\boldsymbol{\Phi}}_{i,j,k,l}(t)\,\frac{v_x-v_{xk}}{\Delta v_{xk}} + \overline{\Delta_{v_y}\boldsymbol{\Phi}}_{i,j,k,l}(t)\,\frac{v_y-v_{yl}}{\Delta v_{yl}}\\ &\quad + \overline{\Delta_{xv_x}\boldsymbol{\Phi}}_{i,j,k,l}(t)\,\frac{x-x_i}{\Delta x_i}\frac{v_x-v_{xk}}{\Delta v_{xk}} + \overline{\Delta_{yv_y}\boldsymbol{\Phi}}_{i,j,k,l}(t)\,\frac{y-y_j}{\Delta y_j}\frac{v_y-v_{yl}}{\Delta v_{yl}}. \quad (4.61)\end{aligned}$$

The dependence on (t, x, y, v_x, v_y) of $\boldsymbol{\Phi}$ and $\boldsymbol{\Phi}_{i,j,k,l}$ will be omitted from subsequent expressions; so will the time-dependence of the cell-average $\overline{\boldsymbol{\Phi}}_{i,j,k,l}$ and the undivided gradients $\overline{\Delta_{(\cdot)}\boldsymbol{\Phi}}_{i,j,k,l}$. The cell-average is defined as

$$\overline{\boldsymbol{\Phi}}_{i,j,k,l} = \frac{1}{V_{i,j,k,l}}\iiiint_{\Omega_{i,j,k,l}} \boldsymbol{\Phi}\,\mathrm{d}x\,\mathrm{d}y\,\mathrm{d}v_x\mathrm{d}v_y; \quad (4.62)$$

it is the solution to the discretization equation Eq. (4.66). The undivided gradients are computed from the cell-averages by the same *reconstruction* procedure presented in the FV discretization for the moment system, Section 4.2.2, except for the calculations of

- the quantities $\overline{\Delta_{v_x/v_y}\boldsymbol{\Phi}}$ of cells at the edge of the velocity space

$$\begin{aligned}\overline{\Delta_{v_x}\boldsymbol{\Phi}}_{i,j,1,l} &= \text{central reconstruction}\big(0, \overline{\boldsymbol{\Phi}}_{i,j,1,l}, \overline{\boldsymbol{\Phi}}_{i,j,2,l}\big)\,,\\ \overline{\Delta_{v_x}\boldsymbol{\Phi}}_{i,j,N_{v_x},l} &= \text{central reconstruction}\big(\overline{\boldsymbol{\Phi}}_{i,j,N_{v_x}-1,l}, \overline{\boldsymbol{\Phi}}_{i,j,N_{v_x},l}, 0\big)\,,\end{aligned}$$

$\overline{\Delta_{v_y}\mathbf{\Phi}}$ at $l = 1/N_{v_y}$, calculated similarly; recall that $\overline{\Delta_{x/y}\mathbf{\Phi}}$ of cells at the edge of the physical space are reconstructed by the *one-sided* calculation;

- the cross-space undivided gradients

$$\overline{\Delta_{xv_x}\mathbf{\Phi}}_{i,j,k,l} = \text{central reconstruction}\left(\overline{\Delta_x\mathbf{\Phi}}_{i,j,k-1,l}, \overline{\Delta_x\mathbf{\Phi}}_{i,j,k,l}, \overline{\Delta_x\mathbf{\Phi}}_{i,j,k+1,l}\right),$$
$$\overline{\Delta_{yv_y}\mathbf{\Phi}}_{i,j,k,l} = \text{central reconstruction}\left(\overline{\Delta_y\mathbf{\Phi}}_{i,j,k,l-1}, \overline{\Delta_y\mathbf{\Phi}}_{i,j,k,l}, \overline{\Delta_y\mathbf{\Phi}}_{i,j,k,l+1}\right),$$

this calculation has one operation less than the calculation of $\overline{\Delta_{xy}\mathbf{U}}$ in the moment system, saving significant computational time as the current computational grid is easily two orders of magnitude larger than that of the moment system. At the edge of the velocity space we have

$$\overline{\Delta_{xv_x}\mathbf{\Phi}}_{i,j,1,l} = \text{central reconstruction}\left(0, \overline{\Delta_x\mathbf{\Phi}}_{i,j,1,l}, \overline{\Delta_x\mathbf{\Phi}}_{i,j,2,l}\right),$$
$$\overline{\Delta_{xv_x}\mathbf{\Phi}}_{i,j,N_{v_x},l} = \text{central reconstruction}\left(\overline{\Delta_x\mathbf{\Phi}}_{i,j,N_{v_x}-1,l}, \overline{\Delta_x\mathbf{\Phi}}_{i,j,N_{v_x},l}, 0\right).$$

In the velocity space outside of $\Omega_{\mathbf{v}}$, it is assumed that values of both the cell-averages and the undivided gradients are zero.

Equation (4.53) is integrated over the phase-space domain $\Omega_{i,j,k,l}$ to obtain the following semi-discrete equation

$$\begin{aligned}\frac{\partial\overline{\mathbf{\Phi}}_{i,j,k,l}(t)}{\partial t} = &-\frac{1}{V_{i,j,k,l}}\underbrace{\int_{I_j}\left(\iint_{\Omega_{k,l}} v_x\mathbf{\Phi}\Big|_{x_{i-1/2}}^{x_{i+1/2}}\mathrm{d}v_x\mathrm{d}v_y\right)\mathrm{d}y}_{\text{Boundary integral}}\\ &-\frac{1}{V_{i,j,k,l}}\underbrace{\int_{I_i}\left(\iint_{\Omega_{k,l}} v_y\mathbf{\Phi}\Big|_{y_{j-1/2}}^{y_{j+1/2}}\mathrm{d}v_x\mathrm{d}v_y\right)\mathrm{d}x}_{\text{Boundary integral}}\\ &-\frac{1}{V_{i,j,k,l}}\underbrace{\iint_{\Omega_{i,j}}\frac{1}{\tau(x,y)}\left(\iint_{\Omega_{k,l}}(\mathbf{\Phi}-\mathbf{\Phi}_{\mathrm{M}})\,\mathrm{d}v_x\mathrm{d}v_y\right)\mathrm{d}x\,\mathrm{d}y}_{\text{Volume integral}},\end{aligned} \tag{4.66}$$

where $\mathbf{\Phi}_{\mathrm{M}}$ is also a function of (t, x, y, v_x, v_y), $I_i = \{x : x \in [x_{i-1/2}, x_{i+1/2}]\}$, and $I_j = \{y : y \in [y_{j-1/2}, y_{j+1/2}]\}$. Quite opposite to properties of the moment system, the integrands of the boundary integrals have uncomplicated expressions that are analytically integrable. Computing the volume integral of the collision integral, however, is not straightforward.

The calculations of the x-interface and y-interface boundary integrals are fundamentally identical. For illustrative purposes, the calculation of the $\left(i + \frac{1}{2}\right)$-interface term will be described in detail. The distribution function at that interface has the upwind value

$$\mathbf{\Phi}_{i+1/2,j,k,l}(y, v_x, v_y) = \begin{cases} \mathbf{\Phi}_{i+1,j,k,l}\left(x_{i+1/2}, y, v_x, v_y\right) & \text{if } v_x \leq 0 \\ \mathbf{\Phi}_{i,j,k,l}\left(x_{i+1/2}, y, v_x, v_y\right) & \text{if } v_x \geq 0 \end{cases}. \tag{4.67}$$

To facilitate the calculation, the velocity grid is created in such a way that v_x or v_y of any phase-space cell is either *only negative* or *only positive*. The boundary integral is then evaluated analytically:

- when v_x is always negative in cell $\Omega_{i,j,k,l}$, $v_{xk+1/2} \leq 0$,

$$\begin{aligned} \int_{I_j} \left(\iint_{\Omega_{k,l}} v_x \mathbf{\Phi}_{i+1/2,j,k,l}(y, v_x, v_y) \, \mathrm{d}v_x \mathrm{d}v_y \right) \mathrm{d}y \\ = V_{k,l} \Delta y_j \left[v_{xk} \left(\overline{\mathbf{\Phi}}_{i+1,j,k,l} - \frac{\overline{\Delta_x \mathbf{\Phi}}_{i+1,j,k,l}}{2} \right) \right. \\ \left. + \frac{\Delta v_{xk}}{12} \left(\overline{\Delta_{v_x} \mathbf{\Phi}}_{i+1,j,k,l} - \frac{\overline{\Delta_{x v_x} \mathbf{\Phi}}_{i+1,j,k,l}}{2} \right) \right]; \end{aligned} \tag{4.68}$$

- when v_x is always positive in cell $\Omega_{i,j,k,l}$, $v_{xk-1/2} \geq 0$,

$$\int_{I_j} \left(\iint_{\Omega_{k,l}} v_x \boldsymbol{\Phi}_{i+1/2,j,k,l}(y, v_x, v_y)\, \mathrm{d}v_x \mathrm{d}v_y \right) \mathrm{d}y = V_{k,l} \Delta y_j \left[v_{xk} \left(\overline{\boldsymbol{\Phi}}_{i,j,k,l} + \frac{\overline{\Delta_x \boldsymbol{\Phi}}_{i,j,k,l}}{2} \right) + \frac{\Delta v_{xk}}{12} \left(\overline{\Delta_{v_x} \boldsymbol{\Phi}}_{i,j,k,l} + \frac{\overline{\Delta_{x v_x} \boldsymbol{\Phi}}_{i,j,k,l}}{2} \right) \right]; \quad (4.69)$$

In the volume integral, $\boldsymbol{\Phi}$ is substituted by $\boldsymbol{\Phi}_{i,j,k,l}$ defined in Eq. (4.61). Then the integral over the velocity domain $\Omega_{k,l}$ is computed exactly,

$$\iint_{\Omega_{k,l}} \boldsymbol{\Phi}\, \mathrm{d}v_x \mathrm{d}v_y = \iint_{\Omega_{k,l}} \boldsymbol{\Phi}_{i,j,k,l} \mathrm{d}v_x \mathrm{d}v_y = V_{k,l} \left(\overline{\boldsymbol{\Phi}}_{i,j,k,l} + \overline{\Delta_x \boldsymbol{\Phi}}_{i,j,k,l} \frac{x - x_i}{\Delta x_i} + \overline{\Delta_y \boldsymbol{\Phi}}_{i,j,k,l} \frac{y - y_j}{\Delta y_j} \right). \quad (4.70)$$

The reduced Maxwellian distribution functions $\boldsymbol{\Phi}_{\mathrm{M}}$ is defined by Eq. (4.55) using the macroscopic quantities $\rho_{i,j}$, $u_{x i,j}$, $u_{y_{i,j}}$, and $T_{i,j}$, which generally vary in the physical domain $\Omega_{i,j}$. Section 4.3.5 will present their calculation from the numerical solutions $\boldsymbol{\Phi}_{i,j,k,l}$. Unlike $\boldsymbol{\Phi}_{i,j,k,l}$, which is only defined over the phase-space domain $\Omega_{i,j,k,l}$, the $\boldsymbol{\Phi}_{\mathrm{M}}$ as described is not a "piecewise" defined function with respect to the velocity space. At any location within the physical domain $\Omega_{i,j}$, it is a unique function depending on (v_x, v_y) that does not change when we move from one velocity domain to another. Thus it is indexed by (i, j), not (i, j, k, l),

$$\boldsymbol{\Phi}_{\mathrm{M}} \to \boldsymbol{\Phi}_{\mathrm{M}i,j}(t, x, y, v_x, v_y) = \begin{bmatrix} 1 \\ \frac{RT_{i,j}}{2} \end{bmatrix} \frac{\rho_{i,j}}{2\pi RT_{i,j}} \exp\left[-\frac{\left(v_x - u_{x i,j}\right)^2 + \left(v_y - u_{y_{i,j}}\right)^2}{2RT_{i,j}} \right]. \quad (4.71)$$

Its integral over the velocity domain is analytically integrable:

$$\begin{aligned}\iint_{\Omega_{k,l}} \Phi_{0\mathrm{M}i,j}\mathrm{d}v_x\mathrm{d}v_y &= V_{k,l}\left\langle \Phi_{0\mathrm{M}i,j}\right\rangle_{k,l} \\ &= \frac{\rho_{i,j}}{4}\left[\operatorname{erf}\left(\frac{v_{xk+1/2}-u_{xi,j}}{\sqrt{2RT_{i,j}}}\right)-\operatorname{erf}\left(\frac{v_{xk-1/2}-u_{xi,j}}{\sqrt{2RT_{i,j}}}\right)\right] \\ &\quad\times\left[\operatorname{erf}\left(\frac{v_{yl+1/2}-u_{yi,j}}{\sqrt{2RT_{i,j}}}\right)-\operatorname{erf}\left(\frac{v_{yl-1/2}-u_{yi,j}}{\sqrt{2RT_{i,j}}}\right)\right], \end{aligned} \tag{4.72a}$$

$$\iint_{\Omega_{k,l}} \Phi_{1\mathrm{M}i,j}\mathrm{d}v_x\mathrm{d}v_y = V_{k,l}\left\langle \Phi_{1\mathrm{M}i,j}\right\rangle_{k,l} = V_{k,l}\,\frac{RT_{i,j}}{2}\left\langle \Phi_{0\mathrm{M}i,j}\right\rangle_{k,l}. \tag{4.72b}$$

Here the angled brackets $\langle\cdot\rangle_{k,l}$ denote averaging over the velocity domain $\Omega_{k,l}$, as oppose to the notation $\overline{(\cdot)}$ used for averaging over the whole phase-space domain $\Omega_{i,j,k,l}$. The expression for the volume integral, after integration over the velocity domain, is too complicated to be handled analytically any further. Therefore, the integration over the physical domain $\Omega_{i,j}$ will be computed approximately by Gaussian quadrature.

It must be noted that the calculation of $\left\langle \mathbf{\Phi}_{\mathrm{M}i,j}\right\rangle_{k,l}$ by averaging the smooth $\mathbf{\Phi}_{\mathrm{M}i,j}$ given by Eq. (4.71) will not preserve the collisional invariants described in Section 2.1.2, as pointed out by Mieussens [41, 42]. This means the resulted numerical discretization will not insure the conservation of mass, momentum, and energy. For these conservation laws to be fulfilled, at any arbitrary physical location, $\mathbf{\Phi}_{\mathrm{M}}$ has to produce the same (ρ, u_x, u_y, T) as $\mathbf{\Phi}$ does. This condition is automatically satisfied by the smooth $\mathbf{\Phi}_{\mathrm{M}i,j}$ because it is constructed using $(\rho, u_x, u_y, T)_{i,j}$ calculated from the numerical solution $\mathbf{\Phi}_{i,j,k,l}$. However, the volume-integral calculation described by Eq. (4.72) has the effect of replacing the *smooth* $\mathbf{\Phi}_{\mathrm{M}i,j}(v_x, v_y)$ by the *piecewise-constant* approximation $\left\langle \mathbf{\Phi}_{\mathrm{M}i,j}\right\rangle_{k,l}$, which has the same mass but not momentum and energy. We correct this situation by refining the velocity grid so that the thatched-roof function better approximates the smooth distribution. This brute-force approach

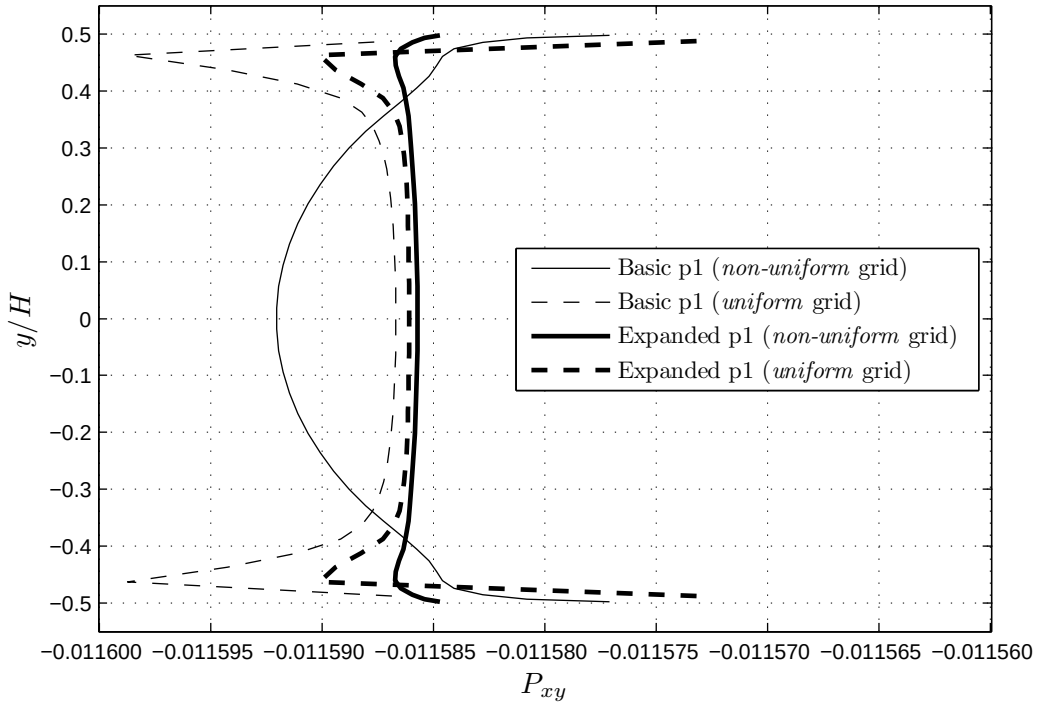

Figure 4.4: Profile of shear stress for Couette flow at $Kn = 0.1$, $T^{\mathrm{w}} = 300\mathrm{K}$, and $M^{\mathrm{w}} = 0.01$, with fully-diffuse solid-boundary condition. The computational grid is $N_y = 40$ and $N_{v_x} \times N_{v_y} = 50 \times 50$.

has the advantage of being simple, but it will make the simulation run more slowly and require more computer memory. The remedy presented in [41, 42] is elegant, but might be expensive and complicated. It requires solving an optimization problem with $N_{v_x} \times N_{v_y}$ variables.

Why do we use the expanded basis?

In a FV discretization, the exact $\mathbf{\Phi}$ over the phase-space cell (i, j, k, l) is traditionally approximated by

$$\begin{aligned}\underset{(x,y,v_x,v_y)\in\Omega_{i,j,k,l}}{\mathbf{\Phi}(t,x,y,v_x,v_y)} &\approx \mathbf{\Phi}_{i,j,k,l}(t,x,y,v_x,v_y) \\ &= \overline{\mathbf{\Phi}}_{i,j,k,l}(t) + \overline{\Delta_x \mathbf{\Phi}}_{i,j,k,l}(t)\,\frac{x-x_i}{\Delta x_i} + \overline{\Delta_y \mathbf{\Phi}}_{i,j,k,l}(t)\,\frac{y-y_j}{\Delta y_j} \\ &\quad + \overline{\Delta_{v_x} \mathbf{\Phi}}_{i,j,k,l}(t)\,\frac{v_x - v_{xk}}{\Delta v_{xk}} + \overline{\Delta_{v_y} \mathbf{\Phi}}_{i,j,k,l}(t)\,\frac{v_y - v_{yl}}{\Delta v_{yl}}, \quad (4.73)\end{aligned}$$

i. e., the cross-derivatives terms missing. Figure 4.4 shows that the solution of this basic FV discretization is surprisingly *grid-dependent*, although the difference is only approximately 0.2%. The addition of the cross-terms associated with $\overline{\Delta_{xv_x/yv_y}\mathbf{\Phi}}$ removes the dependence. There still is a difference between the expanded-FV results on the uniform and non-uniform grids; this is due to the difference in grid resolution near the wall. The improvement achieved by adding cross-terms motivates us to use a full-tensor basis in the spatial discretizations of the moment system as presented in Sections 4.2.2 and 4.2.3.

4.3.4 Discontinuous Galerkin discretization of the reduced system of the BGK equation

Recognizing the improvement offered by cross-terms, presented in the previous section, we use the full-tensor $p1$ DG discretization to solve the reduced system of the BGK equation, Eq. (4.53). The true solution $\mathbf{\Phi}(t, x, y, v_x, v_y)$ is approximated by a four-dimensional polynomial,

$$\begin{aligned}
\underset{(x,y,v_x,v_y)\in\Omega_{i,j,k,l}}{\mathbf{\Phi}(t,x,y,v_x,v_y)} \approx \mathbf{\Phi}_{i,j,k,l}(t,x,y,v_x,v_y) &= \sum_{\alpha,\beta,\gamma,\delta=0}^{1} \mathbf{a}_{i,j,k,l}^{\alpha\beta\gamma\delta}(t)\,\phi_{i,j,k,l}^{\alpha\beta\gamma\delta}(x,y,v_x,v_y) \\
&= \mathbf{a}_{i,j,k,l}^{0000}\phi_{i,j,k,l}^{0000} + \mathbf{a}_{i,j,k,l}^{1000}\phi_{i,j,k,l}^{1000} + \mathbf{a}_{i,j,k,l}^{0100}\phi_{i,j,k,l}^{0100} + \mathbf{a}_{i,j,k,l}^{1100}\phi_{i,j,k,l}^{1100} \\
&+ \mathbf{a}_{i,j,k,l}^{0010}\phi_{i,j,k,l}^{0010} + \mathbf{a}_{i,j,k,l}^{1010}\phi_{i,j,k,l}^{1010} + \mathbf{a}_{i,j,k,l}^{0110}\phi_{i,j,k,l}^{0110} + \mathbf{a}_{i,j,k,l}^{1110}\phi_{i,j,k,l}^{1110} \\
&+ \mathbf{a}_{i,j,k,l}^{0001}\phi_{i,j,k,l}^{0001} + \mathbf{a}_{i,j,k,l}^{1001}\phi_{i,j,k,l}^{1001} + \mathbf{a}_{i,j,k,l}^{0101}\phi_{i,j,k,l}^{0101} + \mathbf{a}_{i,j,k,l}^{1101}\phi_{i,j,k,l}^{1101} \\
&+ \mathbf{a}_{i,j,k,l}^{0011}\phi_{i,j,k,l}^{0011} + \mathbf{a}_{i,j,k,l}^{1011}\phi_{i,j,k,l}^{1011} + \mathbf{a}_{i,j,k,l}^{0111}\phi_{i,j,k,l}^{0111} + \mathbf{a}_{i,j,k,l}^{1111}\phi_{i,j,k,l}^{1111}.
\end{aligned} \tag{4.74}$$

The general expression of the four-dimensional orthogonal Legendre polynomials $\phi_{i,j,k,l}^{\alpha\beta\gamma\delta}$ is given by

$$\phi_{i,j,k,l}^{\alpha\beta\gamma\delta}(x,y,v_x,v_y) = \underbrace{\phi_i^{\alpha}(x)\,\phi_j^{\beta}(y)}_{\phi_{i,j}^{\alpha\beta}(x,y)}\underbrace{\phi_k^{\gamma}(v_x)\,\phi_l^{\delta}(v_y)}_{\phi_{k,l}^{\gamma\delta}(v_x,v_y)}, \tag{4.75}$$

where the 1-D Legendre polynomials, up to first-order, are defined below:

$$\phi_i^0(x) \equiv \phi_j^0(y) \equiv \phi_k^0(v_x) \equiv \phi_l^0(v_y) = 1, \tag{4.76a}$$

$$\phi_i^1(x) = \frac{x - x_i}{\Delta x_i}, \tag{4.76b}$$

$$\phi_j^1(y) = \frac{y - y_j}{\Delta y_j}, \tag{4.76c}$$

$$\phi_k^1(v_x) = \frac{v_x - v_{xk}}{\Delta v_{xk}}, \tag{4.76d}$$

$$\phi_l^1(v_y) = \frac{v_y - v_{yl}}{\Delta v_{yl}}. \tag{4.76e}$$

Owing to the orthogonality of the basis functions, we have

$$\iiiint_{\Omega_{i,j,k,l}} \phi_{i,j,k,l}^{\alpha\beta\gamma\delta} \mathbf{\Phi}_{i,j,k,l} \mathrm{d}x \, \mathrm{d}y \, \mathrm{d}v_x \mathrm{d}v_y = \frac{V_{i,j,k,l}}{12^{\alpha+\beta+\gamma+\delta}} \mathbf{a}_{i,j,k,l}^{\alpha\beta\gamma\delta}. \tag{4.77}$$

Sixteen update equations for the *sixteen* coefficients $\mathbf{a}_{i,j,k,l}^{\alpha\beta\gamma\delta}$ are derived by the same four-step procedure used in the DG discretization of moment systems. They are

- multiply Eq. (4.53) with the basis function $\phi_{i,j,k,l}^{\alpha\beta\gamma\delta}(x, y, v_x, v_y)$,
- integrate over the phase-space domain $\Omega_{i,j,k,l}$,
- apply integration by parts to the flux terms to transfer the spatial derivatives from the flux functions to the basis functions,
- calculate the volume integrals using only local information, which means substituting the exact solution $\mathbf{\Phi}$ by its numerical representation $\mathbf{\Phi}_{i,j,k,l}$, and
- calculate the boundary integrals using information of the current cell, $\mathbf{\Phi}_{i,j,k,l}$, and its neighbors in physical space, $\mathbf{\Phi}_{i\pm\frac{1}{2},j\pm\frac{1}{2},k,l}$.

In the end, we obtain the semi-discrete equations for the coefficients $\mathbf{a}_{i,j,k,l}^{\alpha\beta\gamma\delta}$, which

have the following general form:

$$\frac{V_{i,j,k,l}}{12^{\alpha+\beta+\gamma+\delta}}\frac{\partial \mathbf{a}_{i,j,k,l}^{\alpha\beta\gamma\delta}(t)}{\partial t} =$$
$$\underbrace{-\int_{I_j}\iint_{\Omega_{k,l}}\left(\phi_{i,j,k,l}^{\alpha\beta\gamma\delta}v_x\mathbf{\Phi}\right)\Big|_{x_{i-1/2}}^{x_{i+1/2}}\mathrm{d}v_x\mathrm{d}v_y\,\mathrm{d}y}_{\text{boundary integral}} + \underbrace{\iiiint_{\Omega_{i,j,k,l}}\frac{\partial\phi_{i,j,k,l}^{\alpha\beta\gamma\delta}}{\partial x}v_x\mathbf{\Phi}_{i,j,k,l}\,\mathrm{d}x\,\mathrm{d}y\,\mathrm{d}v_x\mathrm{d}v_y}_{\text{volume integral}}$$
$$\underbrace{-\int_{I_i}\iint_{\Omega_{k,l}}\left(\phi_{i,j,k,l}^{\alpha\beta\gamma\delta}v_y\mathbf{\Phi}\right)\Big|_{y_{j-1/2}}^{y_{j+1/2}}\mathrm{d}v_x\mathrm{d}v_y\,\mathrm{d}x}_{\text{boundary integral}} + \underbrace{\iiiint_{\Omega_{i,j,k,l}}\frac{\partial\phi_{i,j,k,l}^{\alpha\beta\gamma\delta}}{\partial y}v_y\mathbf{\Phi}_{i,j,k,l}\,\mathrm{d}x\,\mathrm{d}y\,\mathrm{d}v_x\mathrm{d}v_y}_{\text{volume integral}}$$
$$\underbrace{-\iint_{\Omega_{i,j}}\frac{1}{\tau(x,y)}\left[\iint_{\Omega_{k,l}}\phi_{i,j,k,l}^{\alpha\beta\gamma\delta}\left(\mathbf{\Phi}_{i,j,k,l}-\mathbf{\Phi}_{\mathrm{M}i,j}\right)\mathrm{d}v_x\mathrm{d}v_y\right]\mathrm{d}x\,\mathrm{d}y}_{\text{volume integral}}\,. \quad (4.78)$$

The reduced Maxwellian distribution function $\mathbf{\Phi}_{\mathrm{M}i,j}(t,x,y,v_x,v_y)$ has been defined by Eq. (4.71).

The volume integral of the source term is rearranged to

$$\iint_{\Omega_{i,j}}\frac{1}{\tau(x,y)}\left[\iint_{\Omega_{k,l}}\phi_{i,j,k,l}^{\alpha\beta\gamma\delta}\left(\mathbf{\Phi}_{i,j,k,l}-\mathbf{\Phi}_{\mathrm{M}i,j}\right)\mathrm{d}v_x\mathrm{d}v_y\right]\mathrm{d}x\,\mathrm{d}y$$
$$=\iint_{\Omega_{i,j}}\frac{\phi_{i,j}^{\alpha\beta}(x,y)}{\tau(x,y)}\left[\iint_{\Omega_{k,l}}\phi_{k,l}^{\gamma\delta}(v_x,v_y)\left(\mathbf{\Phi}_{i,j,k,l}-\mathbf{\Phi}_{\mathrm{M}i,j}\right)\mathrm{d}v_x\mathrm{d}v_y\right]\mathrm{d}x\,\mathrm{d}y \quad (4.79)$$

The inner integration over the velocity domain $\Omega_{k,l}$ is evaluated analytically, for all four possibilities of $\phi_{k,l}^{\gamma\delta}(v_x,v_y)$. Result of the $\mathbf{\Phi}_{i,j,k,l}$-term can be expressed in a generic

form,

$$\iint\limits_{\Omega_{k,l}} \phi_{k,l}^{\gamma\delta} \mathbf{\Phi}_{i,j,k,l} \mathrm{d}v_x \mathrm{d}v_y$$
$$= V_{i,j} \left(\mathbf{a}_{i,j,k,l}^{00\gamma\delta} + \mathbf{a}_{i,j,k,l}^{10\gamma\delta} \phi_i^1(x) + \mathbf{a}_{i,j,k,l}^{01\gamma\delta} \phi_j^1(y) + \mathbf{a}_{i,j,k,l}^{11\gamma\delta} \phi_i^1(x) \phi_j^1(y) \right). \quad (4.80)$$

For the $\mathbf{\Phi}_{\mathrm{M}i,j}$-term, unfortunately there is no generic form;

- for $\phi_{k,l}^{\gamma\delta}(v_x, v_y) = \phi_{k,l}^{00}(v_x, v_y) = \phi_k^0(v_x)\, \phi_l^0(v_y) = 1$,

$$\iint\limits_{\Omega_{k,l}} \mathbf{\Phi}_{\mathrm{M}i,j} \mathrm{d}v_x \mathrm{d}v_y = \begin{bmatrix} 1 \\ \frac{RT_{i,j}}{2} \end{bmatrix} \frac{\rho}{4} \, \mathrm{ErfTv_x} \, \mathrm{ErfTv_y}; \quad (4.81)$$

- for $\phi_{k,l}^{\gamma\delta}(v_x, v_y) = \phi_{k,l}^{10}(v_x, v_y) = \phi_k^1(v_x)\phi_l^0(v_y) = \dfrac{v_x - v_{xk}}{\Delta v_{xk}}$,

$$\iint\limits_{\Omega_{k,l}} \frac{v_x - v_{xk}}{\Delta v_{xk}} \mathbf{\Phi}_{\mathrm{M}i,j} \mathrm{d}v_x \mathrm{d}v_y$$
$$= \begin{bmatrix} 1 \\ \frac{RT_{i,j}}{2} \end{bmatrix} \frac{\rho_{i,j}}{2\Delta v_{xk}} \mathrm{ErfTv_y} \left(\frac{u_{xi,j} - v_{xk}}{2} \mathrm{ErfTv_x} - \sqrt{\frac{RT_{i,j}}{2\pi}} \mathrm{ExpTv_x} \right); \quad (4.82)$$

- for $\phi_{k,l}^{\gamma\delta}(v_x, v_y) = \phi_{k,l}^{01}(v_x, v_y) = \phi_k^0(v_x)\, \phi_l^1(v_y) = \dfrac{v_y - v_{yl}}{\Delta v_{yl}}$,

$$\iint\limits_{\Omega_{k,l}} \frac{v_y - v_{yl}}{\Delta v_{yl}} \mathbf{\Phi}_{\mathrm{M}i,j} \mathrm{d}v_x \mathrm{d}v_y$$
$$= \begin{bmatrix} 1 \\ \frac{RT_{i,j}}{2} \end{bmatrix} \frac{\rho_{i,j}}{2\Delta v_{yl}} \mathrm{ErfTv_x} \left(\frac{u_{yi,j} - v_{yl}}{2} \mathrm{ErfTv_y} - \sqrt{\frac{RT_{i,j}}{2\pi}} \mathrm{ExpTv_y} \right); \quad (4.83)$$

- for $\phi_{k,l}^{\gamma\delta}(v_x, v_y) = \phi_{k,l}^{11}(v_x, v_y) = \phi_k^1(v_x)\phi_l^1(v_y) = \dfrac{v_x - v_{xk}}{\Delta v_{xk}} \dfrac{v_y - v_{yl}}{\Delta v_{yl}}$,

$$\begin{aligned}
&\iint\limits_{\Omega_{k,l}} \frac{v_x - v_{xk}}{\Delta v_{xk}} \frac{v_y - v_{yl}}{\Delta v_{yl}} \mathbf{\Phi}_{\mathrm{M}i,j} \mathrm{d}v_x \mathrm{d}v_y \\
&\qquad = \frac{1}{V_{k,l}} \iint_{\Omega_{k,l}} v_x v_y \mathbf{\Phi}_{\mathrm{M}i,j} \mathrm{d}v_x \mathrm{d}v_y - \frac{v_{xk}}{\Delta v_{xk}} \int_{\Omega_{k,l}} \phi_{k,l}^{01} \mathbf{\Phi}_{\mathrm{M}i,j} \mathrm{d}v_x \mathrm{d}v_y \\
&\qquad\quad - \frac{v_{yl}}{\Delta v_{yl}} \int_{\Omega_{k,l}} \phi_{k,l}^{10} \mathbf{\Phi}_{\mathrm{M}i,j} \mathrm{d}v_x \mathrm{d}v_y - \frac{v_{xk} v_{yl}}{V_{k,l}} \iint_{\Omega_{k,l}} \mathbf{\Phi}_{\mathrm{M}i,j} \mathrm{d}v_x \mathrm{d}v_y; \quad (4.84)
\end{aligned}$$

where

$$\mathrm{ErfTv_x} = \mathrm{erf}\left(\frac{v_{xk+1/2} - u_{xi,j}}{\sqrt{2RT_{i,j}}} \right) - \mathrm{erf}\left(\frac{v_{xk-1/2} - u_{xi,j}}{\sqrt{2RT_{i,j}}} \right), \quad (4.85a)$$

$$\mathrm{ErfTv_y} = \mathrm{erf}\left(\frac{v_{yl+1/2} - u_{yi,j}}{\sqrt{2RT_{i,j}}} \right) - \mathrm{erf}\left(\frac{v_{yl-1/2} - u_{yi,j}}{\sqrt{2RT_{i,j}}} \right), \quad (4.85b)$$

$$\mathrm{ExpTv_x} = \exp\left(-\frac{\left(v_{xk+1/2} - u_{xi,j}\right)^2}{2RT_{i,j}} \right) - \exp\left(-\frac{\left(v_{xk-1/2} - u_{xi,j}\right)^2}{2RT_{i,j}} \right), \quad (4.85c)$$

$$\mathrm{ExpTv_y} = \exp\left(-\frac{\left(v_{yl+1/2} - u_{yi,j}\right)^2}{2RT_{i,j}} \right) - \exp\left(-\frac{\left(v_{yl-1/2} - u_{yi,j}\right)^2}{2RT_{i,j}} \right), \quad (4.85d)$$

and

$$\begin{aligned}
&\iint_{\Omega_{k,l}} v_x v_y \mathbf{\Phi}_{\mathrm{M}i,j} \mathrm{d}v_x \mathrm{d}v_y \\
&\qquad = \begin{bmatrix} 1 \\ \frac{RT_{i,j}}{2} \end{bmatrix} \frac{\rho}{4} \Big(2\mathrm{ExpTv_x} - u_{xi,j} \mathrm{ErfTv_x} \Big) \Big(2\mathrm{ExpTv_y} - u_{yi,j} \mathrm{ErfTv_y} \Big). \quad (4.86)
\end{aligned}$$

Similarly to the FV discretization of the reduced system, the 4-D volume integral is reduced to a 2-D integral in the physical domain $\Omega_{i,j}$, which is then computed approximately by Gaussian quadrature because its integrand is a complicated expression.

The quadruple volume integrals of the fluxes can be analytically integrated be-

cause their dependence on (x, y, v_x, v_y) is explicit and in polynomial form. For the purpose of illustration, only the calculation of the x-flux volume integral with the most complicated test-function, $\phi^{\alpha\beta\gamma\delta}_{i,j,k,l} = \phi^{1111}_{i,j,k,l}$, is presented; calculations for other test functions are fundamentally the same.

$$\iiiint\limits_{\Omega_{i,j,k,l}} \frac{\partial \phi^{1111}_{i,j,k,l}}{\partial x} v_x \mathbf{\Phi}_{i,j,k,l} \,\mathrm{d}x \,\mathrm{d}y \,\mathrm{d}v_x \mathrm{d}v_y$$
$$= \frac{\Delta y_j \Delta v_{xk} \Delta v_{yl}}{1728} \left(v_{xk} \mathbf{a}^{0111}_{i,j,k,l} + \Delta v_{xk} \mathbf{a}^{0101}_{i,j,k,l} \right) \quad (4.87)$$

The boundary integrals of the interface fluxes are also analytically integrable,

- when v_x is always negative in cell $\Omega_{i,j,k,l}$, $v_{xk+1/2} \leq 0$,

$$\int\limits_{I_j} \iint\limits_{\Omega_{k,l}} \left(\phi^{1111}_{i,j,k,l} v_x \mathbf{\Phi} \right) \Big|_{x_{i+1/2}} \mathrm{d}v_x \mathrm{d}v_y \,\mathrm{d}y$$
$$= \int\limits_{I_j} \iint\limits_{\Omega_{k,l}} \phi^{1111}_{i,j,k,l}\big(x_{i+1/2}, y, v_x, v_y\big) \, v_x \mathbf{\Phi}_{i+1,j,k,l}\big(x_{i+1/2}, y, v_x, v_y\big) \,\mathrm{d}v_x \mathrm{d}v_y \,\mathrm{d}y$$
$$= \frac{V_{i,j,k,l}}{3456 \Delta x_i} \left[\left(\mathbf{a}^{0111}_{i+1,j,k,l} - \frac{\mathbf{a}^{1111}_{i+1,j,k,l}}{2} \right) v_{xk} + \left(\mathbf{a}^{0101}_{i+1,j,k,l} - \frac{\mathbf{a}^{1101}_{i+1,j,k,l}}{2} \right) \Delta v_{xk} \right]; \quad (4.88)$$

- when v_x is always positive in cell $\Omega_{i,j,k,l}$, $v_{xk-1/2} \geq 0$,

$$\int\limits_{I_j} \iint\limits_{\Omega_{k,l}} \left(\phi^{1111}_{i,j,k,l} v_x \mathbf{\Phi} \right) \Big|_{x_{i+1/2}} \mathrm{d}v_x \mathrm{d}v_y \,\mathrm{d}y$$
$$= \int\limits_{I_j} \iint\limits_{\Omega_{k,l}} \phi^{1111}_{i,j,k,l}\big(x_{i+1/2}, y, v_x, v_y\big) \, v_x \mathbf{\Phi}_{i,j,k,l}\big(x_{i+1/2}, y, v_x, v_y\big) \,\mathrm{d}v_x \mathrm{d}v_y \,\mathrm{d}y$$
$$= \frac{V_{i,j,k,l}}{3456 \Delta x_i} \left[\left(\mathbf{a}^{0111}_{i,j,k,l} + \frac{\mathbf{a}^{1111}_{i,j,k,l}}{2} \right) v_{xk} + \left(\mathbf{a}^{0101}_{i,j,k,l} + \frac{\mathbf{a}^{1101}_{i,j,k,l}}{2} \right) \Delta v_{xk} \right]. \quad (4.89)$$

Now we have all necessary ingredients to represent Eq. (4.78).

4.3.5 Calculations of the macroscopic quantities from the discretized reduced distribution functions $\mathbf{\Phi}$

Macroscopic quantities of the flow are calculated from the reduced distribution functions by evaluating integrals over the truncated velocity domain $\Omega_{\mathbf{v}}$. The first step is to calculate the conservative variables directly from $\mathbf{\Phi}$ using Eq. (4.56). The second step is to compute the primitive variables $\mathbf{V}$, given by Eq. (2.35), from the conservative variables. The infinite integration limits in Eq. (4.56) are changed to the truncated velocity space $\Omega_{\mathbf{v}}$,

$$\begin{aligned}\mathbf{U}_{i,j}(x,y) &= \iint_{\Omega_{\mathbf{v}}} \Big(\mathbf{W}_0\Phi_0 + \mathbf{W}_1\Phi_1\Big)\mathrm{d}v_x\mathrm{d}v_y \\ &= \sum_{k=1}^{N_{vx}}\sum_{l=1}^{N_{vy}} \iint_{\Omega_{k,l}} \Big(\mathbf{W}_0\Phi_{0_{i,j,k,l}} + \mathbf{W}_1\Phi_{1_{i,j,k,l}}\Big)\mathrm{d}v_x\mathrm{d}v_y, \quad (4.90)\end{aligned}$$

where

$$\mathbf{W}_0(v_x,v_y) = \left[1, v_x, v_y, v_x^2, v_y^2, 0, v_xv_y, v_x\left(v_x^2+v_y^2\right), v_y\left(v_x^2+v_y^2\right)\right]^{\mathrm{T}}, \quad (4.91a)$$

$$\mathbf{W}_1(v_x,v_y) = [0,0,0,0,0,1,0,v_x,v_y]^{\mathrm{T}}. \quad (4.91b)$$

The integral over the velocity domain $\Omega_{k,l}$ is analytically executable because the integrand has the polynomial form. The resulting $\mathbf{U}_{i,j}$ has the following form if $\mathbf{\Phi}_{i,j,k,l}$ is represented by the DG approximation, Eq. (4.74),

$$\mathbf{U}_{i,j}(x,y) = \overline{\mathbf{U}}_{i,j} + \overline{\Delta_x\mathbf{U}}_{i,j}\phi^{10}_{i,j}(x) + \overline{\Delta_y\mathbf{U}}_{i,j}\phi^{01}_{i,j}(y) + \overline{\Delta_{xy}\mathbf{U}}_{i,j}\phi^{11}_{i,j}(x,y)\,; \quad (4.92)$$

or if the numerical solution is portrayed by Eq. (4.61),

$$\mathbf{U}_{i,j}(x,y) = \overline{\mathbf{U}}_{i,j} + \overline{\Delta_x\mathbf{U}}_{i,j}\phi^{10}_{i,j}(x) + \overline{\Delta_y\mathbf{U}}_{i,j}\phi^{01}_{i,j}(y)\,. \quad (4.93)$$

It is sufficient to present results for the integral $\iint_{\Omega_{k,l}} \mathbf{W}_0 \Phi_{0i,j,k,l} \mathrm{d}v_x \mathrm{d}v_y$, assuming $\Phi_{0i,j,k,l}$ is represented by Eq. (4.74), which will reduce to the FV representation, Eq. (4.61), if we only use $a^{0000}_{i,j,k,l}$, $a^{1000}_{i,j,k,l}$, $a^{0100}_{i,j,k,l}$, $a^{0010}_{i,j,k,l}$, $a^{0001}_{i,j,k,l}$, $a^{1010}_{i,j,k,l}$, and $a^{0101}_{i,j,k,l}$.

- $W = 1$:

$$\frac{1}{V_{k,l}} \iint_{\Omega_{k,l}} \Phi_{0i,j,k,l} \mathrm{d}v_x \mathrm{d}v_y = a^{0000}_{i,j,k,l} + a^{1000}_{i,j,k,l} \phi^{10}_{i,j} + a^{0100}_{i,j,k,l} \phi^{01}_{i,j} + a^{1100}_{i,j,k,l} \phi^{11}_{i,j}; \quad (4.94)$$

- $W = v_x$:

$$\begin{aligned} \frac{1}{V_{k,l}} \iint_{\Omega_{k,l}} v_x \Phi_{0i,j,k,l} \mathrm{d}v_x \mathrm{d}v_y = & \left(v_{xk} a^{0000}_{i,j,k,l} + \frac{\Delta v_{xk}}{12} a^{0010}_{i,j,k,l} \right) \\ & + \left(v_{xk} a^{1000}_{i,j,k,l} + \frac{\Delta v_{xk}}{12} a^{1010}_{i,j,k,l} \right) \phi^{10}_{i,j} + \left(v_{xk} a^{0100}_{i,j,k,l} + \frac{\Delta v_{xk}}{12} a^{0110}_{i,j,k,l} \right) \phi^{01}_{i,j} \\ & + \left(v_{xk} a^{1100}_{i,j,k,l} + \frac{\Delta v_{xk}}{12} a^{1110}_{i,j,k,l} \right) \phi^{11}_{i,j}; \quad (4.95) \end{aligned}$$

- $W = v_y$:

$$\begin{aligned} \frac{1}{V_{k,l}} \iint_{\Omega_{k,l}} v_y \Phi_{0i,j,k,l} \mathrm{d}v_x \mathrm{d}v_y = & \left(v_{yl} a^{0000}_{i,j,k,l} + \frac{\Delta v_{yl}}{12} a^{0001}_{i,j,k,l} \right) \\ & + \left(v_{yl} a^{1000}_{i,j,k,l} + \frac{\Delta v_{yl}}{12} a^{1001}_{i,j,k,l} \right) \phi^{10}_{i,j} + \left(v_{yl} a^{0100}_{i,j,k,l} + \frac{\Delta v_{yl}}{12} a^{0101}_{i,j,k,l} \right) \phi^{01}_{i,j} \\ & + \left(v_{yl} a^{1100}_{i,j,k,l} + \frac{\Delta v_{yl}}{12} a^{1101}_{i,j,k,l} \right) \phi^{11}_{i,j}; \quad (4.96) \end{aligned}$$

- $W = v_x^2$:

$$\begin{aligned} \frac{1}{V_{k,l}} \iint_{\Omega_{k,l}} v_x^2 \Phi_{0i,j,k,l} \mathrm{d}v_x \mathrm{d}v_y = & \left(f_1 a^{0000}_{i,j,k,l} + f_2 a^{0010}_{i,j,k,l} \right) \\ & + \left(f_1 a^{1000}_{i,j,k,l} + f_2 a^{1010}_{i,j,k,l} \right) \phi^{10}_{i,j} + \left(f_1 a^{0100}_{i,j,k,l} + f_2 a^{0110}_{i,j,k,l} \right) \phi^{01}_{i,j} \\ & + \left(f_1 a^{1100}_{i,j,k,l} + f_2 a^{1110}_{i,j,k,l} \right) \phi^{11}_{i,j}, \quad (4.97) \end{aligned}$$

where $f_1 = v_{x_k}^2 + \dfrac{\Delta v_{x_k}^2}{12}$ and $f_2 = \dfrac{v_{xk}\Delta v_{xk}}{6}$;

- $W = v_y^2$:

$$\frac{1}{V_{k,l}} \iint_{\Omega_{k,l}} v_y^2 \Phi_{0_{i,j,k,l}} \mathrm{d}v_x \mathrm{d}v_y = \left(f_1 a_{i,j,k,l}^{0000} + f_2 a_{i,j,k,l}^{0001}\right) + \left(f_1 a_{i,j,k,l}^{1000} + f_2 a_{i,j,k,l}^{1001}\right) \phi_{i,j}^{10} + \left(f_1 a_{i,j,k,l}^{0100} + f_2 a_{i,j,k,l}^{0101}\right) \phi_{i,j}^{01} + \left(f_1 a_{i,j,k,l}^{1100} + f_2 a_{i,j,k,l}^{1101}\right) \phi_{i,j}^{11}, \quad (4.98)$$

where $f_1 = v_{y_l}^2 + \dfrac{\Delta v_{y_l}^2}{12}$ and $f_2 = \dfrac{v_{y_l}\Delta v_{y_l}}{6}$;

- $W = v_x v_y$:

$$\frac{1}{V_{k,l}} \iint_{\Omega_{k,l}} v_x v_y \Phi_{0_{i,j,k,l}} \mathrm{d}v_x \mathrm{d}v_y = \left(f_1 a_{i,j,k,l}^{0000} + f_2 a_{i,j,k,l}^{0010} + f_3 a_{i,j,k,l}^{0001} + \frac{V_{k,l}}{144} a_{i,j,k,l}^{0011}\right) + \left(f_1 a_{i,j,k,l}^{1000} + f_2 a_{i,j,k,l}^{1010} + f_3 a_{i,j,k,l}^{1001} + \frac{V_{k,l}}{144} a_{i,j,k,l}^{1011}\right) \phi_{i,j}^{10} + \left(f_1 a_{i,j,k,l}^{0100} + f_2 a_{i,j,k,l}^{0110} + f_3 a_{i,j,k,l}^{0101} + \frac{V_{k,l}}{144} a_{i,j,k,l}^{0111}\right) \phi_{i,j}^{01} + \left(f_1 a_{i,j,k,l}^{1100} + f_2 a_{i,j,k,l}^{1110} + f_3 a_{i,j,k,l}^{1101} + \frac{V_{k,l}}{144} a_{i,j,k,l}^{1111}\right) \phi_{i,j}^{11}, \quad (4.99)$$

where $f_1 = v_{xk} v_{y_l}$, $f_2 = \dfrac{v_{y_l}\Delta v_{xk}}{12}$, and $f_3 = \dfrac{v_{xk}\Delta v_{y_l}}{12}$;

- $W = v_x \left(v_x^2 + v_y^2\right)$:

$$\frac{1}{V_{k,l}} \iint_{\Omega_{k,l}} v_x \left(v_x^2 + v_y^2\right) \Phi_{0_{i,j,k,l}} \mathrm{d}v_x \mathrm{d}v_y = \left(f_1 a_{i,j,k,l}^{0000} + f_2 a_{i,j,k,l}^{0010} + f_3 a_{i,j,k,l}^{0001} + f_4 a_{i,j,k,l}^{0011}\right) + \left(f_1 a_{i,j,k,l}^{1000} + f_2 a_{i,j,k,l}^{1010} + f_3 a_{i,j,k,l}^{1001} + f_4 a_{i,j,k,l}^{1011}\right) \phi_{i,j}^{10} + \left(f_1 a_{i,j,k,l}^{0100} + f_2 a_{i,j,k,l}^{0110} + f_3 a_{i,j,k,l}^{0101} + f_4 a_{i,j,k,l}^{0111}\right) \phi_{i,j}^{01} + \left(f_1 a_{i,j,k,l}^{1100} + f_2 a_{i,j,k,l}^{1110} + f_3 a_{i,j,k,l}^{1101} + f_4 a_{i,j,k,l}^{1111}\right) \phi_{i,j}^{11}, \quad (4.100)$$

with

$$f_1 = v_{xk}\left(v_{xk}^2 + v_{yl}^2 + \frac{\Delta v_{xk}^2}{4} + \frac{\Delta v_{yl}^2}{12}\right), \qquad f_3 = \frac{v_{xk}v_{yl}\Delta v_{yl}}{6},$$
$$f_2 = \frac{\Delta v_{xk}}{4}\left(v_{xk}^2 + \frac{v_{yl}^2}{3} + \frac{\Delta v_{xk}^2}{20} + \frac{\Delta v_{yl}^2}{36}\right), \quad f_4 = \frac{v_{yl}V_{k,l}}{72};$$

- $W = v_y\left(v_x^2 + v_y^2\right)$: same expression as Eq. (4.100) but with different values of f_i

$$f_1 = v_{yl}\left(v_{xk}^2 + v_{yl}^2 + \frac{\Delta v_{xk}^2}{12} + \frac{\Delta v_{yl}^2}{4}\right), \qquad f_2 = \frac{v_{xk}v_{yl}\Delta v_{xk}}{6},$$
$$f_3 = \frac{\Delta v_{yl}}{4}\left(\frac{v_{xk}^2}{3} + v_{yl}^2 + \frac{\Delta v_{xk}^2}{36} + \frac{\Delta v_{yl}^2}{20}\right), \quad f_4 = \frac{v_{xk}V_{k,l}}{72};$$

4.3.6 Restriction on time-step Δt

The time-step Δt used to solve the reduced system numerically is also computed by Eq. (4.47), but with a different calculation of the advection time-step. In the BGK equation, or its reduced system, the signal speeds of the x-flux and y-flux are v_x and v_y respectively, of which the largest in magnitude happen at the edge of the truncated velocity space $\Omega_{\mathbf{v}}$. Because the phase-space grid does not change in time, it is not necessary to recalculate the advection time-step during simulations. The computation of the collision time-step is identical to that used in the moment system.

4.4 Implementation of the Solid-boundary conditions

4.4.1 Implementation in the 13M system

The alternative solid-boundary conditions derived in Chapter III are only applicable if the solid boundaries are *static*, which is true in the case of Poiseuille flow. In Couette flow, however, the top and bottom solid boundaries move horizontally with

the velocity U^{T} and U^{B} respectively, $\mathbf{u}^{\mathrm{w}} = (U^{\mathrm{w}}, 0, 0)$. It is therefore necessary to modify the results obtained in Section 3.4 to account for movement of the walls.

At the wall, the distribution function (3.12) of the 1–C and Eq. (3.29) of the 2–C model can be commonly expressed as

$$f(\mathbf{v}) = C_1 f^{-}(\mathbf{v}) + \left[\sigma C_2 f_{\mathrm{M}}^{\mathrm{d}}(\mathbf{v}) + (1-\sigma) C_1 f^{-}(\mathbf{v}')\right], \tag{4.101}$$

where f^{-} is the Grad13M distribution function

$$f^{-}(\mathbf{v}) = \frac{\widetilde{\rho}}{\left(2\pi R\widetilde{T}\right)^{3/2}} \exp\left[-\frac{(\mathbf{v}-\widetilde{\mathbf{u}})^2}{2R\widetilde{T}}\right]\left[1 + \frac{\widetilde{p}_{ij}}{2\widetilde{p}R\widetilde{T}}(v_i-\widetilde{u}_i)(v_j-\widetilde{u}_j) + \cdots \right.$$
$$\left. + \frac{\widetilde{q}_k(v_k-\widetilde{u}_k)}{\widetilde{p}R\widetilde{T}}\left(\frac{(\mathbf{v}-\widetilde{\mathbf{u}})^2}{5R\widetilde{T}} - 1\right)\right]. \tag{4.102}$$

The quantities $\widetilde{(\cdot)}$ are the numerical solutions at $y = \pm H/2$, calculated from data of only cells lying next to the walls. The Maxwellian distribution functions $f_{\mathrm{M}}^{\mathrm{d}}$ (Eq. (3.3)) and $f_{\mathrm{M}}^{\mathrm{d}}$ (Eq. (3.11)) now carry information about the wall's velocity:

$$f_{\mathrm{M}}^{\mathrm{d/w}}(v) = \frac{\widetilde{\rho}}{\left(2\pi RT^{\mathrm{d/w}}\right)^{3/2}} \exp\left[-\frac{(v_x-U)^2 + v_y^2 + v_z^2}{2RT^{\mathrm{d/w}}}\right]; \tag{4.103}$$

we obtain following results

$$\left\langle (v_x - U) v_y f_{\mathrm{M}}^{\mathrm{d/w}}(\mathbf{v}) \right\rangle^{+} = 0 \tag{4.104}$$

$$\left\langle v_y \frac{(\mathbf{v}-\mathbf{u}^{\mathrm{w}})^2}{2} f_{\mathrm{M}}^{\mathrm{d/w}}(\mathbf{v}) \right\rangle^{+} = 2\widetilde{\rho}RT^{\mathrm{d/w}}\sqrt{\frac{RT^{\mathrm{d/w}}}{2\pi}}. \tag{4.105}$$

The modification principle is to replacing $\mathbf{v}$ by $(\mathbf{v}-\mathbf{u}^{\mathrm{w}}) = (v_x - U, v_y, v_z)$ in all calculations of C_1, C_2, σ, and T^{d}. Considering only the bottom wall, velocities of the

incident molecules satisfy

$$(\mathbf{v}-\mathbf{u}^{\mathrm{w}})\cdot\mathbf{n}\leq 0\Rightarrow v_y\leq 0;$$

conversely, the reflected molecules' velocities satisfy

$$(\mathbf{v}-\mathbf{u}^{\mathrm{w}})\cdot\mathbf{n}\geq 0\Rightarrow v_y\geq 0.$$

Formulas for the non-penetration and normalization conditions are unchanged from Eq. (3.31). Due to the appearance of v_x in the expressions of σ_{m} and σ_{e}, Eqs. (3.33a) and (3.33b) are adjusted to

$$\sigma_{\mathrm{m}}=\frac{\sigma C_1\left\langle (v_x-U)\,v_y f^{-}(\mathbf{v})\right\rangle^{-}+\sigma C_2\left\langle (v_x-U)\,v_y f_{\mathrm{M}}^{\mathrm{d}}(\mathbf{v})\right\rangle^{+}}{C_1'\left\langle (v_x-U)\,v_y f^{-}(\mathbf{v})\right\rangle^{-}+C_2'\left\langle (v_x-U)\,v_y f_{\mathrm{M}}^{\mathrm{w}}(\mathbf{v})\right\rangle^{+}}, \tag{4.106a}$$

$$\sigma_{\mathrm{e}}=\frac{\sigma C_1\left\langle v_y\dfrac{(\mathbf{v}-\mathbf{u}^{\mathrm{w}})^2}{2}f^{-}(\mathbf{v})\right\rangle^{-}+\sigma C_2\left\langle v_y\dfrac{(\mathbf{v}-\mathbf{u}^{\mathrm{w}})^2}{2}f_{\mathrm{M}}^{\mathrm{d}}(\mathbf{v})\right\rangle^{+}}{C_1'\left\langle v_y\dfrac{(\mathbf{v}-\mathbf{u}^{\mathrm{w}})^2}{2}f^{-}(\mathbf{v})\right\rangle^{-}+C_2'\left\langle v_y\dfrac{(\mathbf{v}-\mathbf{u}^{\mathrm{w}})^2}{2}f_{\mathrm{M}}^{\mathrm{w}}(\mathbf{v})\right\rangle^{+}}. \tag{4.106b}$$

All subsequent steps are similar to those presented in Section 3.4.2. The values of C_1, C_2, σ, and T^{d} are summarized in Table 4.4. Note that this is for the bottom wall only; the calculation for the top wall is conceptually identical. Now the distribution function at the wall is completely defined in terms of the wall's parameters and the flow data at $y=\pm H/2$. The y-interface flux at the solid boundary is then computed by integrating Eq. (4.101) over the velocity space:

$$\begin{aligned}\iiint_{-\infty}^{+\infty} v_y\mathbf{W}(\mathbf{v})\,f(\mathbf{v})\,\mathrm{d}\mathbf{v}&=C_1\left\langle v_y\mathbf{W}(\mathbf{v})\,f^{-}(\mathbf{v})\right\rangle^{-}+\cdots\\&\quad+\sigma C_2\left\langle v_y\mathbf{W}(\mathbf{v})\,f_{\mathrm{M}}^{\mathrm{d}}(\mathbf{v})\right\rangle^{+}+(1-\sigma)\,C_1\left\langle v_y\mathbf{W}(\mathbf{v})\,f^{-}(\mathbf{v}')\right\rangle^{+},\end{aligned} \tag{4.107}$$

where $\mathbf{W}(\mathbf{v})$ defined by Eq. (4.46), and the half-v_y-space integrals of $f_{\mathrm{w}}^{\mathrm{d}}$ are shown in Table A.2 of Appendix A.

4.4.2 Implementation in the BGK equation

For the reduced system of the BGK equation, we also used two boundary-condition models, the 1–C and the 2–C model. The 1–C is the Maxwell model presented in Section 3.1, while the latter is an adaptation of the 2–C model derived for moment systems in Section 3.4.2.

The distribution function at the wall is also expressed by Eq. (4.101). The expressions for the coefficients C_1 and C_2, as well as σ and T^{d} are given in Table 4.4. In moment systems, the explicit relation between f^- and the flow's macroscopic quantities facilitates analytical computation of all necessary half-v_y-space integrals for the boundary-condition formulation. However, in the BGK equation, there is no such an explicit relation; the half-v_y-space integrals are calculated in discretized manner similar to the calculation of the conservative variables from $\mathbf{\Phi}_{i,j,k,l}$ in Section 4.3.5.

$$\begin{aligned}
\left\langle \widehat{f}^{-}(\mathbf{v}) \right\rangle^{-} &= \frac{1}{\rho} \int_{-\infty}^{+\infty} \int_{-\infty}^{0} {\Phi_0}^{-}(v_x, v_y)\, \mathrm{d}v_y \mathrm{d}v_x \\
&= \frac{1}{\rho} \sum_{k=1}^{N_{v_x}} \sum_{\forall l: v_y \le 0} \iint_{\Omega_{k,l}} {\Phi_0}^{-}(v_x, v_y)\, \mathrm{d}v_x \mathrm{d}v_y, \qquad (4.108) \\
\left\langle v_y f^{-}(\mathbf{v}) \right\rangle^{-} &= \int_{-\infty}^{+\infty} \int_{-\infty}^{0} v_y {\Phi_0}^{-}(v_x, v_y)\, \mathrm{d}v_y\, \mathrm{d}v_x \\
&= \sum_{k=1}^{N_{v_x}} \sum_{\forall l: v_y \le 0} \iint_{\Omega_{k,l}} v_y {\Phi_0}^{-}(v_x, v_y)\, \mathrm{d}v_x \mathrm{d}v_y, \qquad (4.109)
\end{aligned}$$

and

$$\left\langle v_y \frac{\left(\mathbf{v}-\mathbf{u}^{\mathrm{w}}\right)^2}{2} f^-(\mathbf{v}) \right\rangle^-$$
$$= \int_{-\infty}^{+\infty} \int_{-\infty}^{0} \left[v_y \frac{(v_x-U)^2+v_y^2}{2} {\Phi_0}^-(v_x,v_y) + \frac{v_y}{2} {\Phi_1}^-(v_x,v_y) \right] \mathrm{d}v_y \, \mathrm{d}v_x$$
$$= \frac{1}{2} \sum_{k=1}^{N_{v_x}} \sum_{\forall l: v_y \leq 0} \iint_{\Omega_{k,l}} \left[v_y \left((v_x-U)^2+v_y^2 \right) {\Phi_0}^- + v_y {\Phi_1}^- \right] \mathrm{d}v_x \mathrm{d}v_y. \quad (4.110)$$

The incident distribution function $\mathbf{\Phi}^-$ is the numerical solution at $y = \pm H/2$

Table 4.4: Values of C_1, C_2, σ, and T^{d} in solid-boundary conditions for Grad's 13-moment system in two dimensions.

Boundary condition models	C_1	C_2	σ	T^{d}
1–C model	1	$-\dfrac{\left\langle v_y f^- (\mathbf{v})\right\rangle^-}{\left\langle v_y f_{\mathrm{M}}^{\mathrm{d}} (\mathbf{v})\right\rangle^+}$	σ_{m}	T_1
2–C model	$-\dfrac{\left\langle v_y f_{\mathrm{M}}^{\mathrm{d}} (\mathbf{v})\right\rangle^+}{\Delta}$	$\dfrac{\left\langle v_y f^- (\mathbf{v})\right\rangle^-}{\Delta}$	σ_1	

$$\Delta = \sigma\left\langle \widehat{f}_{\mathrm{M}}^{\mathrm{d}} (\mathbf{v})\right\rangle^+ \left\langle v_y f^- (\mathbf{v})\right\rangle^- - (2-\sigma)\left\langle \widehat{f}^- (\mathbf{v})\right\rangle^- \left\langle v_y f_{\mathrm{M}}^{\mathrm{d}} (\mathbf{v})\right\rangle^+$$

$$T_1 = \frac{\sigma_{\mathrm{e}}}{\sigma_{\mathrm{m}}} T^{\mathrm{w}} + \left(1 - \frac{\sigma_{\mathrm{e}}}{\sigma_{\mathrm{m}}}\right) \frac{\left\langle v_y \dfrac{(\mathbf{v}-\mathbf{u}^{\mathrm{w}})^2}{2} f^- (\mathbf{v})\right\rangle^-}{2R\left\langle v_y f^- (\mathbf{v})\right\rangle^-}$$

$$\sigma_1 = \frac{-2\sigma_{\mathrm{m}}}{\left(1 - \sigma_{\mathrm{m}}\sqrt{\dfrac{T^{\mathrm{w}}}{T^{\mathrm{d}}}}\right) \dfrac{\left\langle \widehat{f}_{\mathrm{M}}^{\mathrm{w}} (\mathbf{v})\right\rangle^+}{\left\langle \widehat{f}^- (\mathbf{v})\right\rangle^-} \dfrac{\left\langle v_y f^- (\mathbf{v})\right\rangle^-}{\left\langle v_y f_{\mathrm{M}}^{\mathrm{w}} (\mathbf{v})\right\rangle^+} - (1+\sigma_{\mathrm{m}})}$$

$$\left\langle \widehat{f}^- (\mathbf{v})\right\rangle^- = \frac{1}{2} + \sqrt{\frac{R\widetilde{T}}{2\pi}} \frac{\widetilde{q}_y}{5\widetilde{p}R\widetilde{T}} \qquad \left\langle \widehat{f}_{\mathrm{M}}^{\mathrm{w/d}} (\mathbf{v})\right\rangle^+ = \frac{1}{2}$$

$$\left\langle v_y f^- (\mathbf{v})\right\rangle^- = -\frac{\widetilde{\rho}}{2}\sqrt{\frac{R\widetilde{T}}{2\pi}}\left(1 + \frac{\widetilde{P}_{yy}}{\widetilde{p}}\right) \qquad \left\langle v_y f_{\mathrm{M}}^{\mathrm{w/d}} (\mathbf{v})\right\rangle^+ = \widetilde{\rho}\sqrt{\frac{RT^{\mathrm{w/d}}}{2\pi}}$$

$$\left\langle v_y \frac{(\mathbf{v}-\mathbf{u}^{\mathrm{w}})^2}{2} f^- (\mathbf{v})\right\rangle^- = \frac{\widetilde{u}_x \widetilde{P}_{xy} + \widetilde{q}_y}{2} - \frac{1}{2}\sqrt{\frac{R\widetilde{T}}{2\pi}}\left[\widetilde{p} + 3\widetilde{P}_{yy} + \frac{(\widetilde{u}_x - U)^2}{2R\widetilde{T}}\left(\widetilde{p} + \widetilde{P}_{yy}\right) + \frac{2(\widetilde{u}_x - U)\widetilde{q}_x}{5R\widetilde{T}}\right]$$

CHAPTER V

Numerical solutions of Couette and Poiseuille flows

5.1 Numerical solutions of Couette flow

In this section, we present solutions of Couette flow obtained by methods described in Chapter IV. The flow settings are:

- the working fluid is the monatomic Argon gas with ratio of specific heats $\gamma = 5/3$ and specific gas constant $R = 208.132 \frac{\mathrm{J}}{\mathrm{kg\,K}}$;
- the temperature of both top and bottom plates is kept constant at 300K for all simulations, unless specified otherwise;
- the top and bottom plates move in opposite direction with the same speed U^{w} where $M^{\mathrm{w}} = \dfrac{U^{\mathrm{w}}}{\sqrt{\gamma R T^{\mathrm{w}}}} = 0.01$, unless otherwise specified;
- the value of the Prandtl number is $Pr = 1$;
- four different values of the Knudsen number are used, $Kn = 0.01$, 0.1, 1, or 10;
- the gas-surface interaction is fully diffuse, $\sigma_{\mathrm{m}} = 1$ and $\sigma_{\mathrm{e}} = 1$.

We run the simulations at a small Mach number to assure that the flows are always *incompressible* and *laminar*, justifying comparison to the corresponding exact NSF solutions. At these conditions, the variance of temperature in the flow field is

insignificant. The largest difference from T^{w} is approximately 0.1%. The variance of ρ, P_{xx}, P_{yy}, and P_{zz} is also negligible. Therefore, only solutions of u_x, P_{xy}, q_x, and q_y will be displayed. As pointed out in Section 4.1.1, the type of temperature-jump boundary conditions is not relevant for these quantities.

5.1.1 Grid-convergence studies for Couette flow

Before comparing the solutions to the different equation systems amongst themselves, we must establish how fine the grids must be on which these solutions are obtained, to ensure sufficient solution accuracy. Each of the combinations of equations and methods must therefore be subjected to a grid-convergence study. The studies for the 13M system at $Kn = 0.1$ and 10, obtained by both FV and DG discretizations, are presented first in Figs. 5.1 and 5.2. Convergence studies for the BGK equation with the DG method are shown later in Fig. 5.3, but only at $Kn = 0.1$.

Figure 5.1 shows results of the 13M system at $Kn = 0.1$. We only show results for one-tenth of the half-channel abutting the top wall ($y/H = 0.45 \rightarrow 0.5$), where all important details of the grid-refinement studies appear.

The profiles of u_x and q_x show behavior that is qualitatively identical. Values at the wall are approximately the same on all grids. Results from finer grids are *more* oscillatory than results obtained from coarser grids, e. g., 80-cell and 160-cell solutions versus the 20-cell solution by DG, or the 400-cell result versus those on coarser grids by FV. As the grid is refined, the domain of the oscillation is reduced in height and pushed against the boundary, just like oscillations in a shock-wave simulation are pushed toward the shock. Compared to DG solutions, the oscillatory domains obtained by FV are always larger and completely smooth transitions, owing to the higher degree of numerical dissipation associated with the latter discretization.

Shear stress P_{xy} and vertical heat flux q_y also behave quite similarly. Solutions from all grids also give roughly the same values at the wall. A notable difference in

the FV results, compared to the previous solutions of u_x and q_x, is the appearance of excursions at the boundary cell in both P_{xy} and q_y. The magnitudes of the excursions are reduced extremely slowly with grid-refinement; the rate is obviously much smaller than expected even from a first-order method. This results in sharp oscillations followed by a smooth transition domain; similarly to previous results, the combined size of both domains is reduced with the grid-cell size. The anomaly in P_{xy} appears in the FV solutions for all Knudsen numbers, as shown in Fig. 5.2 for $Kn = 10$ and Fig. 5.5 for $Kn = 0.01$ and 1.0. However, for the q_y quantity, it only exists in simulations at $Kn = 0.01$ and 0.1 (shown in Fig. 5.9).

The DG solutions show no such anomaly for any value of the Knudsen number. The visually large differences in P_{xy} as obtained by DG on different grids are actually insignificant because the first five decimal digits of the solutions are the same. It must be mentioned that the convergence rate of P_{xy}(DG) is seemingly only first-order, while we expect it to be at least second-order. However, our studies of the 13M system with *no-slip* boundary condition (not shown) show a convergence rate larger than second-/third-order in the L_∞/L_1-norms, respectively. We therefore attribute the reduction of the convergence rate to effects of the 1–C and 2–C boundary conditions.

Later, in the comparative study of Section 5.1.2, for this Knudsen number ($Kn = 0.1$), we choose to present data obtained from the 40-cell grid (DG) and 80-cell grid (FV), as these grids are sufficiently fine and the oscillation in u_x is less severe than in the results from the two finer grids. Grid-convergence studies at $Kn = 0.01$ and 1 were also preformed but are not presented as they resemble the current case.

Figure 5.2 shows the results for $Kn = 10$ over the top half of the channel ($y/H = 0 \rightarrow H/2$). Compared to the previous calculations at $Kn = 0.1$, the 13M system behaves quite differently. Both DG and FV profiles of u_x, q_x and q_y show that solutions are *divergent* as the grid is refined. Furthermore, the oscillations are no longer restricted to small domains next to the wall but spread over the whole

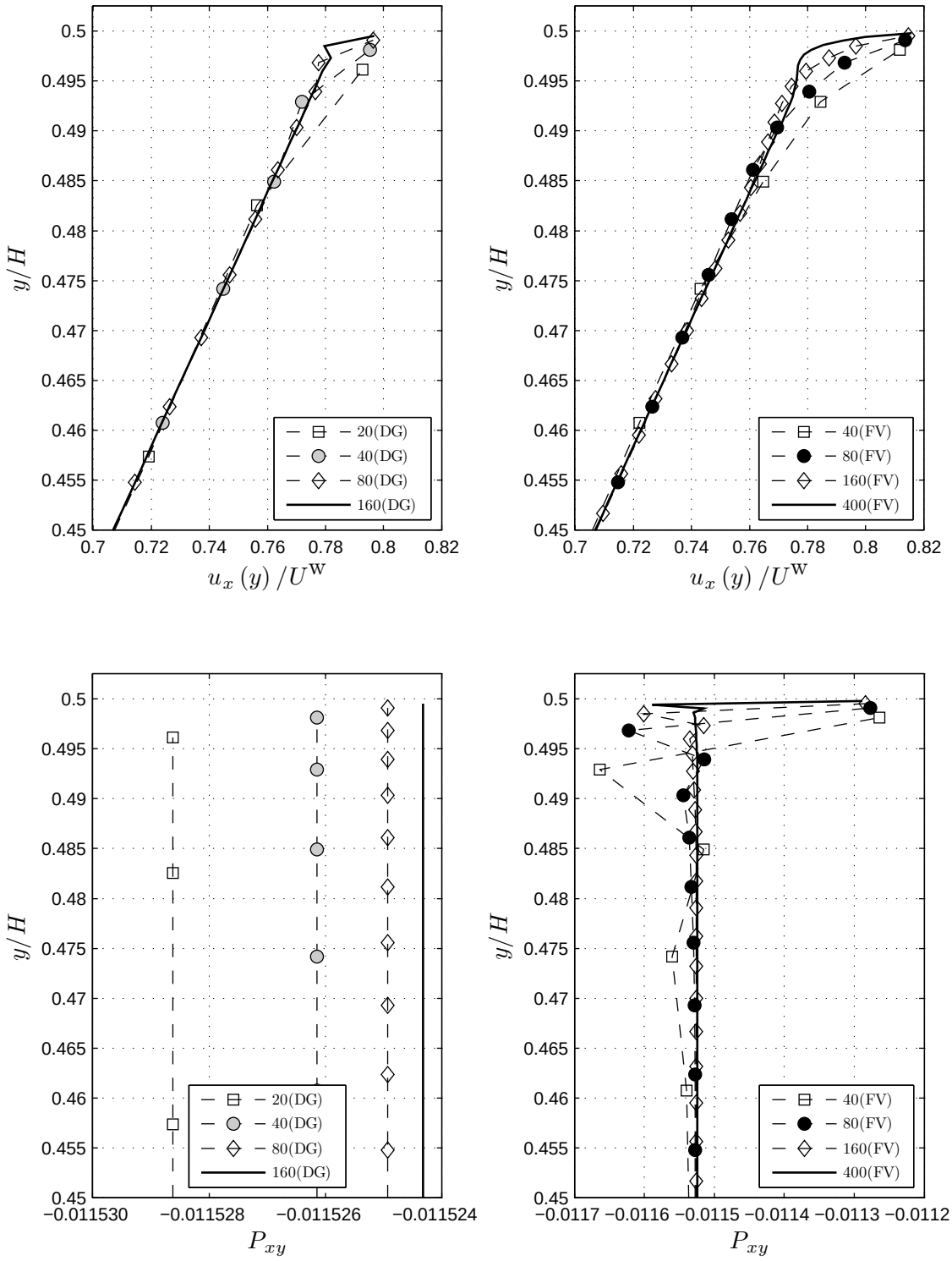

Figure 5.1: Grid-convergence study of the 13M system for Couette flow at $Kn = 0.1$ (left: DG; right:FV).

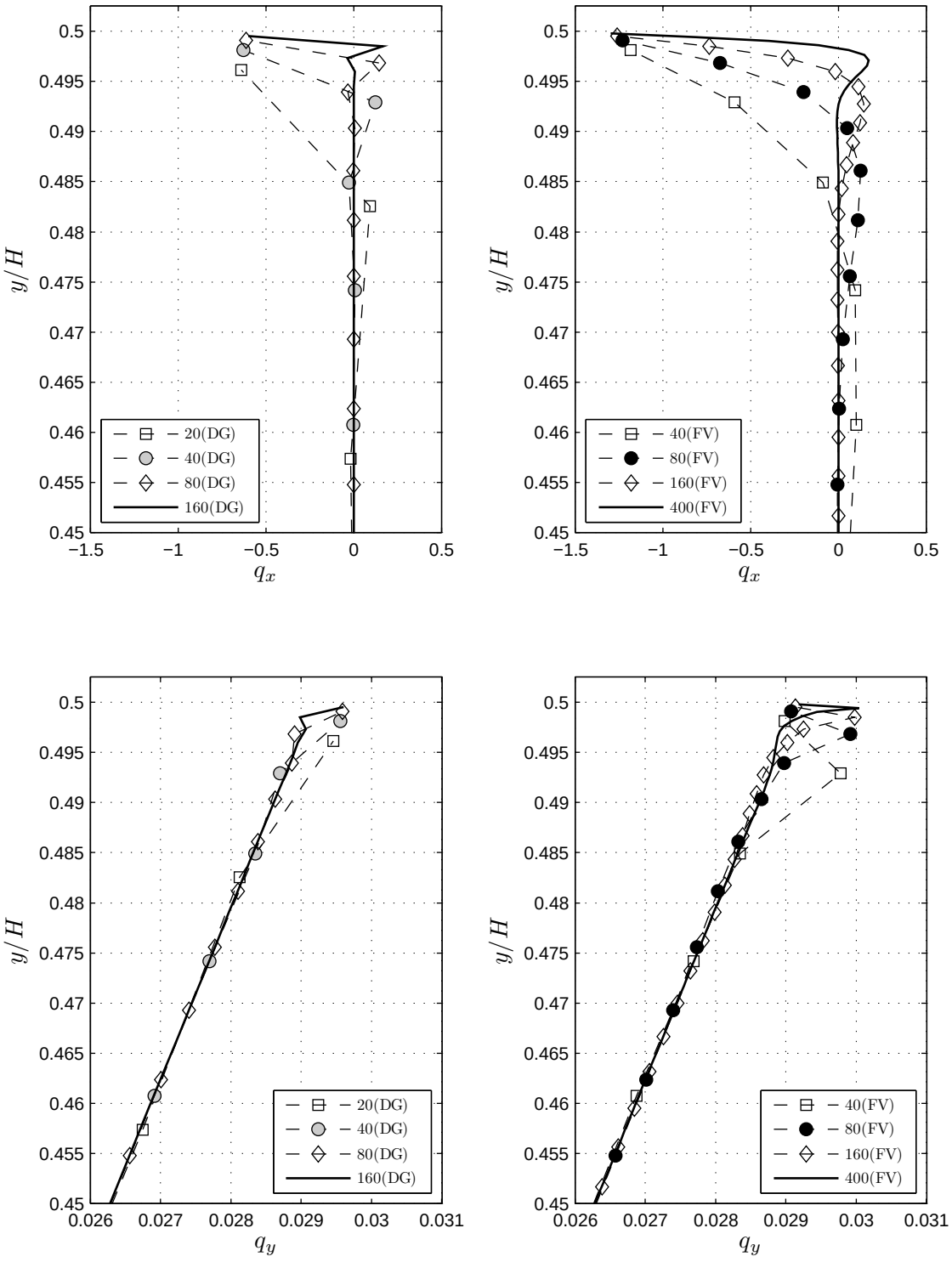

Figure 5.1: Grid-convergence study for the 13M system for Couette flow at $Kn = 0.1$ (cont'd).

channel, and grid refinement makes the situation even worse. For DG solutions, the magnitude of the oscillations on the finest grid (10-cell grid) is so large that it dwarfs details still present on coarser grids. This is why later, in the comparative results of Figures 5.4, 5.7 and 5.8, we stay with an 8-cell grid for $Kn = 10$. These figures show that solutions of u_x, q_x and q_y obtained on the 8-cell grid are, qualitatively, as oscillatory as those on a 10-cell grid.

The DG results for P_{xy} behave badly only on the finest grid, while FV solutions surprisingly converge in the same manner as in the calculations at lower Knudsen numbers. In our opinion, however, the adequate behavior of P_{xy} is merely exception; profiles of other quantities shows that the 13M solutions have become unreliable at $Kn = 10$. Nevertheless, later in Section 5.1.2, we will present the 13M results obtained from the 8-cell grid (DG) and the 20-cell grid (FV) as they are the finest grids having the least oscillations.

The last study we present is the grid refinement with the DG discretization for the BGK equation at $Kn = 0.1$. In Couette flow, the set of independent coordinates is (y, v_x, v_y); the grid-convergence study has to be conducted over the velocity space as well as the physical space. Following is the procedure we employed:

- Choose a certain physical grid that is not too coarse, e. g., a non-uniform 20-cell grid at this particular Knudsen number;
- Start with a coarse velocity grid, e. g., a 10×10 grid, and keep refining it until solution has converged. The finest grid we used is 80×80, and the convergence is essentially achieved by the 16×40 grid.
- Refine the physical grid and repeat the same grid-refinement procedure for velocity space, with 16×40 being the coarsest grid. Our studies show that 16×40 is sufficient for all physical grids studied.

This procedure is repeated for calculations at other Knudsen numbers, with a condi-

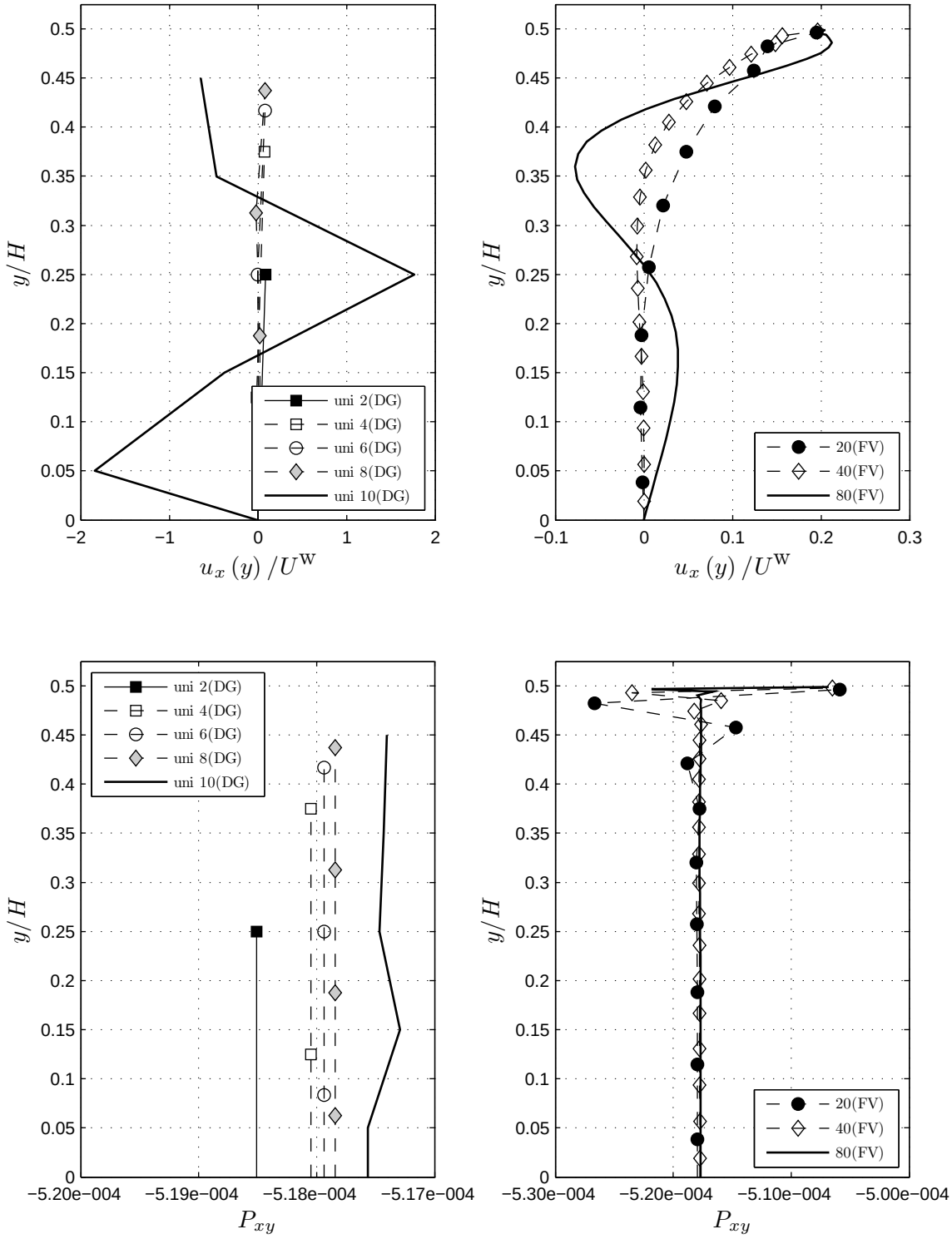

Figure 5.2: Grid-convergence study of the 13M system for Couette flow at $Kn = 10$ (left: DG with *uniform* grid; right: FV with *non-uniform* grid).

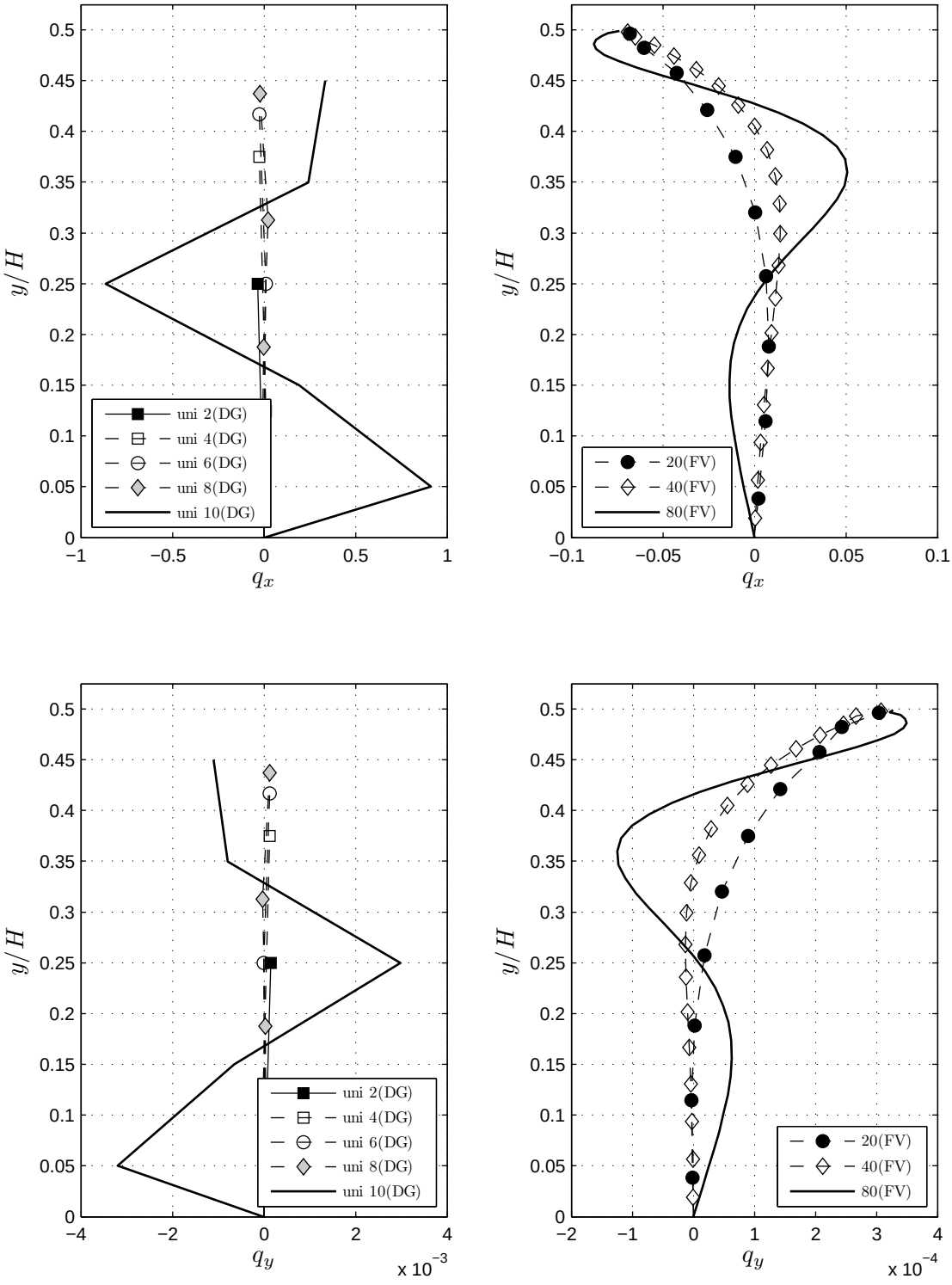

Figure 5.2: Grid-convergence study for the 13M system for Couette flow at $Kn = 10$ (cont'd).

tion that the coarsest grid is always 16×40.

Figure 5.3 shows that it is unnecessary to use a fine physical-grid if the velocity grid is sufficient for convergence, which is also observed in calculations at other Knudsen numbers. The solution from the coarse physical-grid lies on top of the solution from the finest. The figure also demonstrates that a velocity grid of 16×40 is adequate.

Unlike the 13M system, the BGK equation still behaves nicely at $Kn = 10$, as expected. Its solution is qualitatively indifferent from the present case study, thus it is unnecessary to present the data for the other Kn-values, to avoid duplication. Owing to the qualitative similarities between FV and DG solutions, we will not present data from the studies of the former either. The notable difference lies in the converged velocity-grid for the FV discretization, which has 20×50 cells, approximately 1.6 times larger than that of the converged DG grid (16×40).

It is useful to compare 13M and BGK codes with regards to their computational efficiency. Table 5.1 shows the computational cost of the BGK simulations in comparison with the 13M simulations, in terms of required memory and running times using the grids selected previously. All simulations were executed on a personal computer with Intel® Core i7-875K processor (all available 4-core/8-thread were utilized to run in parallel). This table shows that solving the BGK equation requires one order-of-magnitude more computer memory and it runs at least two orders-of-magnitude slower. It must be noted that the faster running time of the DG simulation for the BGK equation compared to FV is probably the result of better optimization of the DG code, as this code was written much later than the FV code, when our proficiency in the C++ language had vastly improved. When everything is equal, we expect the DG simulation to take longer than FV due to the much larger number of update equations (16 vs. 1), even when the phase-space grid of the latter is generally finer.

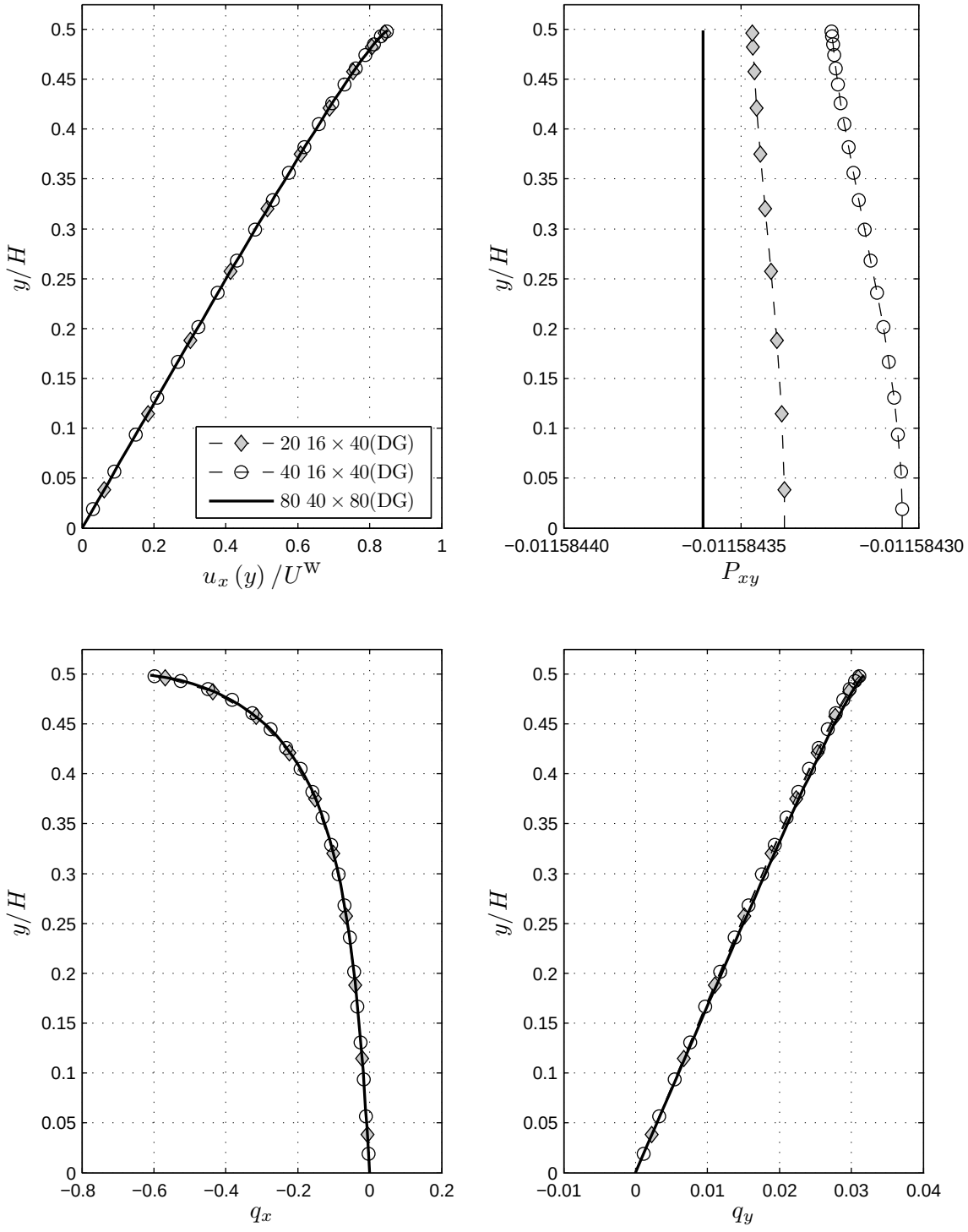

Figure 5.3: Grid-convergence study of the BGK equation (discretized by DG) for Couette flow at $Kn = 0.1$. The first number in the legend is the number of cells in the y-direction, the other two are for the v_x- and v_y-directions.

Table 5.1: Computational costs for Couette-flow simulations at $Kn = 0.1$.

Physical model	Grid	Memory(KB)	Running time(s/h)
13M(FV)	80	2,156	13/0.004
13M(DG)	40	2,140	5/0.001
BGK (FV)	80 20×50	20,556	3,194/0.887
BGK (DG)	40 16×40	28,724	2,548/0.708

5.1.2 Solutions for all values of the Knudsen number

In this section, we compare convergent solutions from all described numerical methods together with the analytical NSF results, at all Knudsen numbers. Figure 5.4 shows the *normalized* velocity at the top wall, $u_x(H/2)$, and the profiles of u_x obtained with DG and FV approximations to the BGK equation and the 13M system, and from the exact NSF solutions. The wall-boundary condition for BGK and 13M is 1–C; for NSF, Maxwell's first-order slip boundary condition was used. Derivation of the analytical NSF solution for Couette flow is presented in Section 4.1.

The two BGK solutions are practically on top of each other for all Knudsen numbers and will serve as the benchmark for 13M and NSF. At $Kn = 0.01$, all solutions are on top of each other. For the next two values, 0.1 and 1, the 13M system has a better prediction of the amount of velocity-slip at the wall than the NSF system. However, slopes of the velocity profiles predicted by the moment system are consistently worse than the NSF results. For $Kn = 10$ the normalized velocities at the wall, $\frac{u_x(H/2)}{U^{\mathrm{w}}}$, of the 13M calculations (both FV and DG) are not shown because they are grossly inaccurate, as seen from the plot of the u_x profile. The result obtained from the FV discretization varies smoothly, while the DG solution is sharply oscillatory. As shown previously in Fig. 5.2, grid refinement does not lead to a convergent solution for either DG or FV; it only results in an even more oscillatory profile with a much larger oscillation amplitude. Conversely, the BGK profiles are entirely smooth,

monotone, and convergent with regard to grid refinement. This reinforces our earlier observation that 13M solutions at $Kn = 10$ are totally inaccurate.

There is a difference of approximately 5% in at $Kn = 10$ between DG and FV results for the BGK equation. There are similar differences, also with the same relative error, in the vertical heat flux q_y at $Kn = 0.01$ and $Kn = 10$ shown in Fig. 5.8.

The inaccuracy of the 13M system at $Kn = 10$ is reasonably understandable. This value borders the *collisionless* flow-regime, which is highly non-equilibrium; the Grad13M distribution function, Eq. (2.30), attempts to account for non-equilibrium effects by perturbing the *equilibrium* Maxwellian distribution function. In order to capture highly non-equilibrium effects it is necessary to add more degrees of freedom to the perturbation process, which means adding more equations to the moment system. This is not unlike the first remedies mentioned in Section 2.3.2 to overcome the embeded inviscid-shock problem.

Figure 5.5 shows results of P_{xy} for all Knudsen numbers. The profiles of P_{xy} from the BGK equation are not really as uniform as shown in the figure. Figure 5.3(DG) and Fig. 5.6(FV) indicate that they actually vary, *insignificantly*, over the flow field. The difference between DG and FV results for the BGK equation are also practically ignorable. At the scale of Fig. 5.5, they are indistinguishable from each other, and their profiles are just vertical lines.

Qualitatively speaking, the NSF and 13M(DG) results match the BGK solutions extremely well for their profiles are also essentially uniform. In the middle region of the channel, the 13M(FV) profiles also match the BGK quite well; for all Knudsen number, however, they exhibit spurious excursion close to the wall. The value of P_{xy} in the boundary cell is always smaller, in magnitude, than those of cells in the middle region, by a small amount, approximately 2.5% for all Knudsen numbers. This spurious jump does exist in the $Kn = 10$ solution as shown in Fig. 5.2, but due to the small magnitude it is not represented well in Fig. 5.5. The excursion causes an sharp

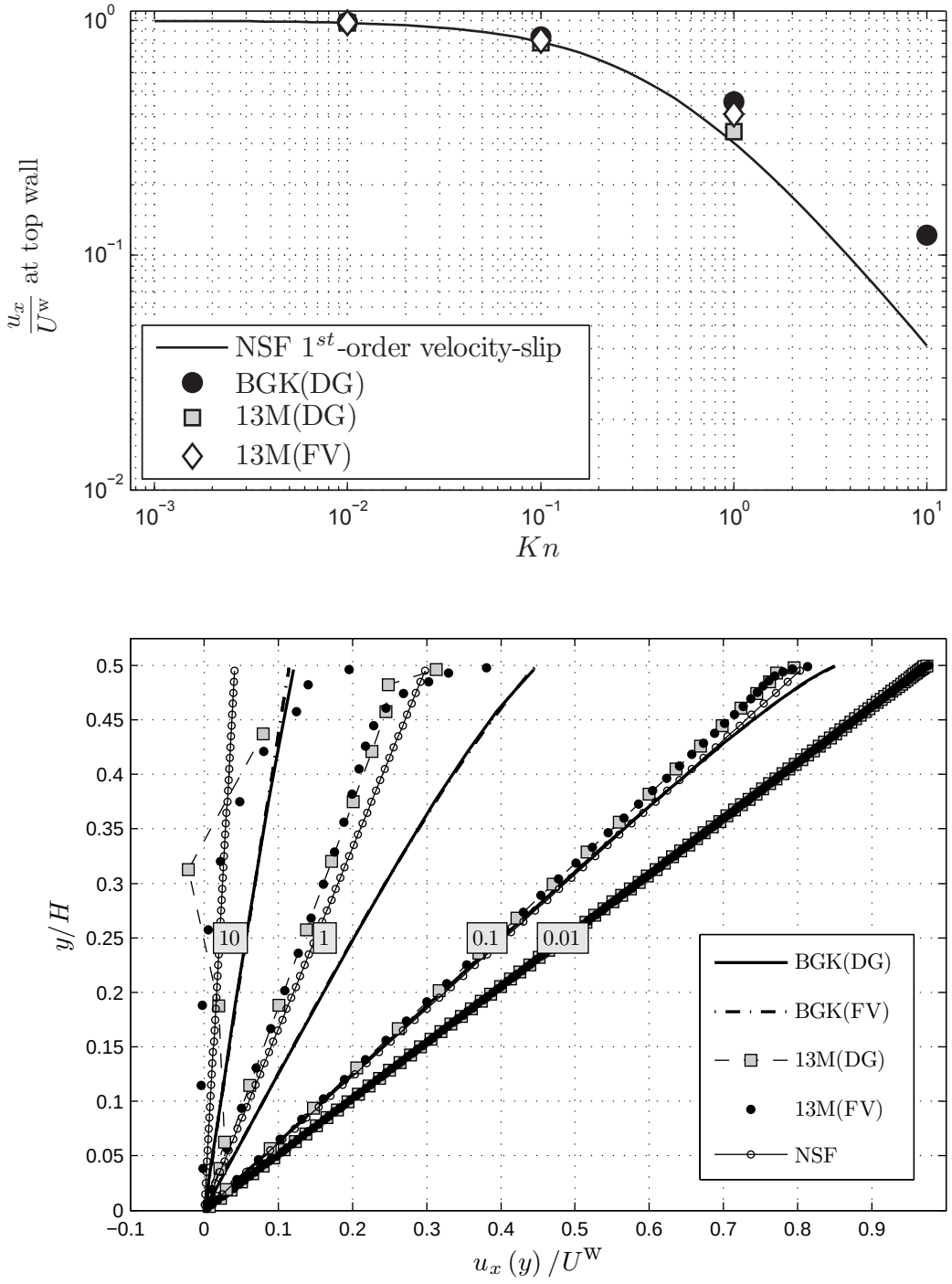

Figure 5.4: Horizontal velocity u_x for Couette flow (top: at the wall; bottom: profile) for $Kn = [0.01, 0.1, 1, 10]$ with 1–C boundary condition (NSF-solutions are obtained with 1^{st}-order velocity-slip boundary condition).

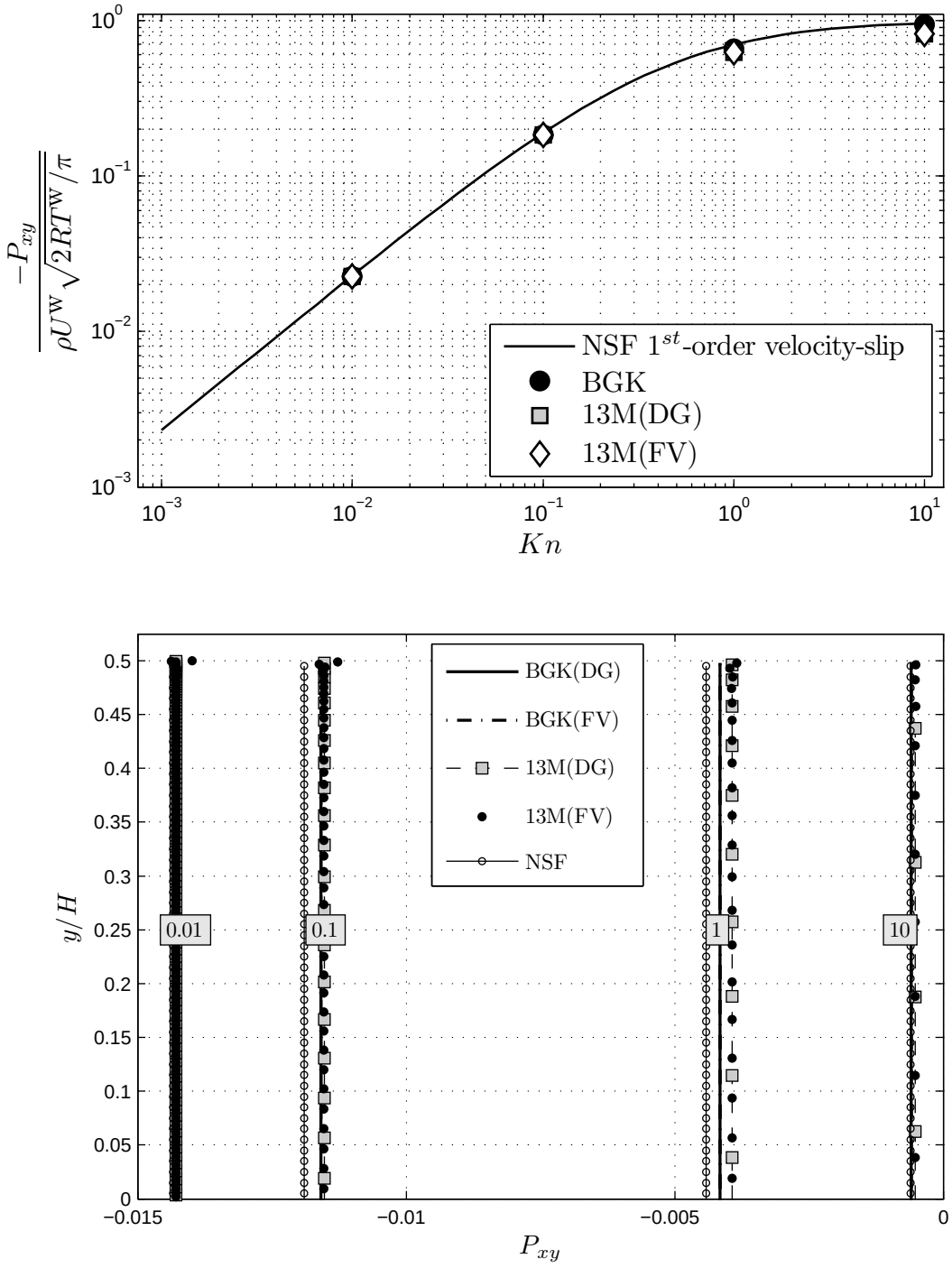

Figure 5.5: Shear stress P_{xy} for Couette flow (top: at wall; bottom: profile) for $Kn = [0.01, 0.1, 1, 10]$ with 1–C boundary condition (NSF-solutions are obtained with 1^{st}-order velocity-slip boundary condition).

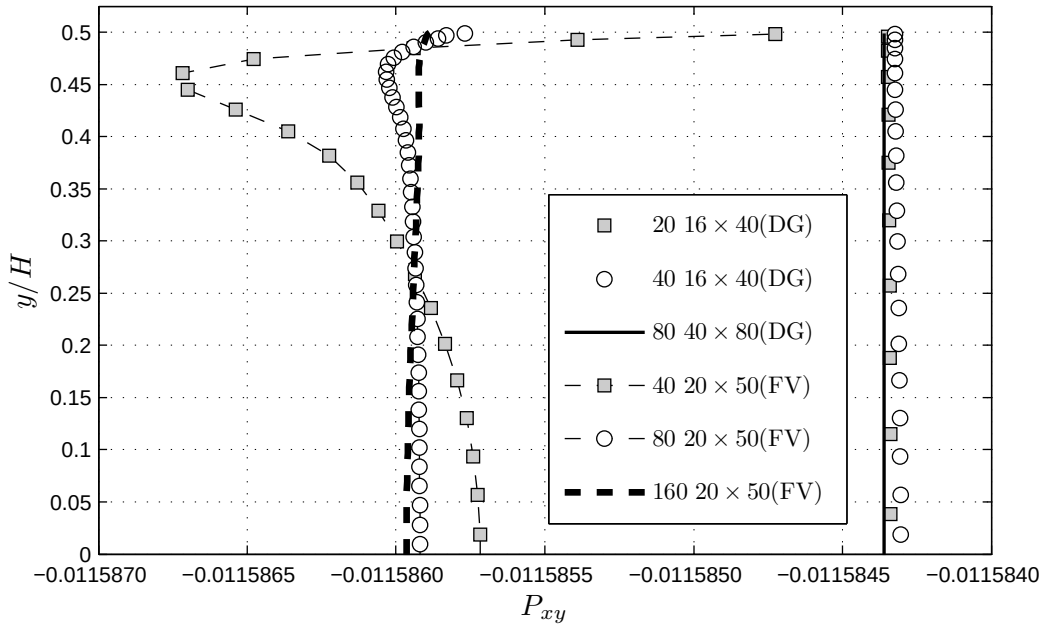

Figure 5.6: Shear stress P_{xy} of the BGK solution for Couette flow at $Kn = 0.1$ with 1–C boundary condition.

oscillation that is damped out over the next few cells. For the plot of normalized P_{xy} (top frame) we use value of the middle region. Results of the 13M system obtained by the DG discretization are clearly better for having no such anomalies.

At a closer look, the behaviors of FV solutions from both 13M system and BGK equation are not unlike. Figure 5.6 for BGK shows that for $Kn = 0.1$ there exist similar jumps in the boundary cell, albeit at an insignificantly small scale; the magnitude of the jump is smaller than 0.03% of the plateau value. The jump also initiates a small oscillatory domain that is shrunk very quickly by grid refinement, which also reduces the jump significantly. A similar situation does exist in calculations at $Kn = 0.01$ (not shown) but not at the other two higher values, 1 and 10. Recall that grid refinement barely has any effect on the 13M(FV) excursion as shown in the grid-convergence studies presented in Section 5.1.1. Again, the DG discretization shows its advantage by eliminating the possible jump in the BGK solutions.

Quantitatively speaking, the 13M system predicts a smaller value of P_{xy} than the

Table 5.2: Values of P_{xy} obtained from the BGK equation (DG), the 13M system (DG), and the NSF system. The relative differences are calculated based on original *double-precision* values of the P_{xy}.

Kn	BGK (DG)	13M(DG)		NSF	
		Value (N/m^2)	Difference vs. BGK (%)	Value (N/m^2)	Difference vs. BGK (%)
0.01	-0.014284	-0.014284	0	-0.014340	0.392
0.1	-0.011528	-0.011526	0.017	-0.011903	3.253
1	-0.003932	-0.003931	0.025	-0.004410	12.157
10	-0.000594	-0.000518	12.795	-0.000604	1.684

BGK solution, while the NSF result is consistently larger. As shown in Table 5.2, the difference between solutions of the 13M system and the BGK equation is insignificant, notwithstanding the result at $Kn = 10$. At all values of Kn up to and including $Kn = 1$, Table 5.2 shows that predictions for shear stress by the 13M system match the BGK solution much better than those produced by the NSF system.

Another interesting observation regarding the shear-stress results is how the NSF solution differs from the BGK solution. Figure 5.4 shows that, for $Kn = 1$ and $Kn = 10$, the velocity gradient $\partial u_x/\partial y$ of the NSF solution is clearly smaller than that of the BGK solution. If we assume the familiar relation (4.10) between shear stress and velocity gradient used in the NSF theory is accurate, P_{xy} of the NSF system is expected to be smaller than value of the BGK solution. However, the opposite relation is supported by the numerical solutions, as shown clearly by the data in Table 5.2. It is thus proved that the aforementioned relation is no longer accurate for flows at sufficiently high Knudsen number. This is one of the factors that makes the NSF system unsuitable for simulating rarefied gas flow.

Figure 5.7 shows the profiles of q_x for all Knudsen numbers. Based on the BGK solution, there is a horizontal heat flux in the direction opposite to the horizontal velocity. The largest value in magnitude is at the boundary, which decreases when

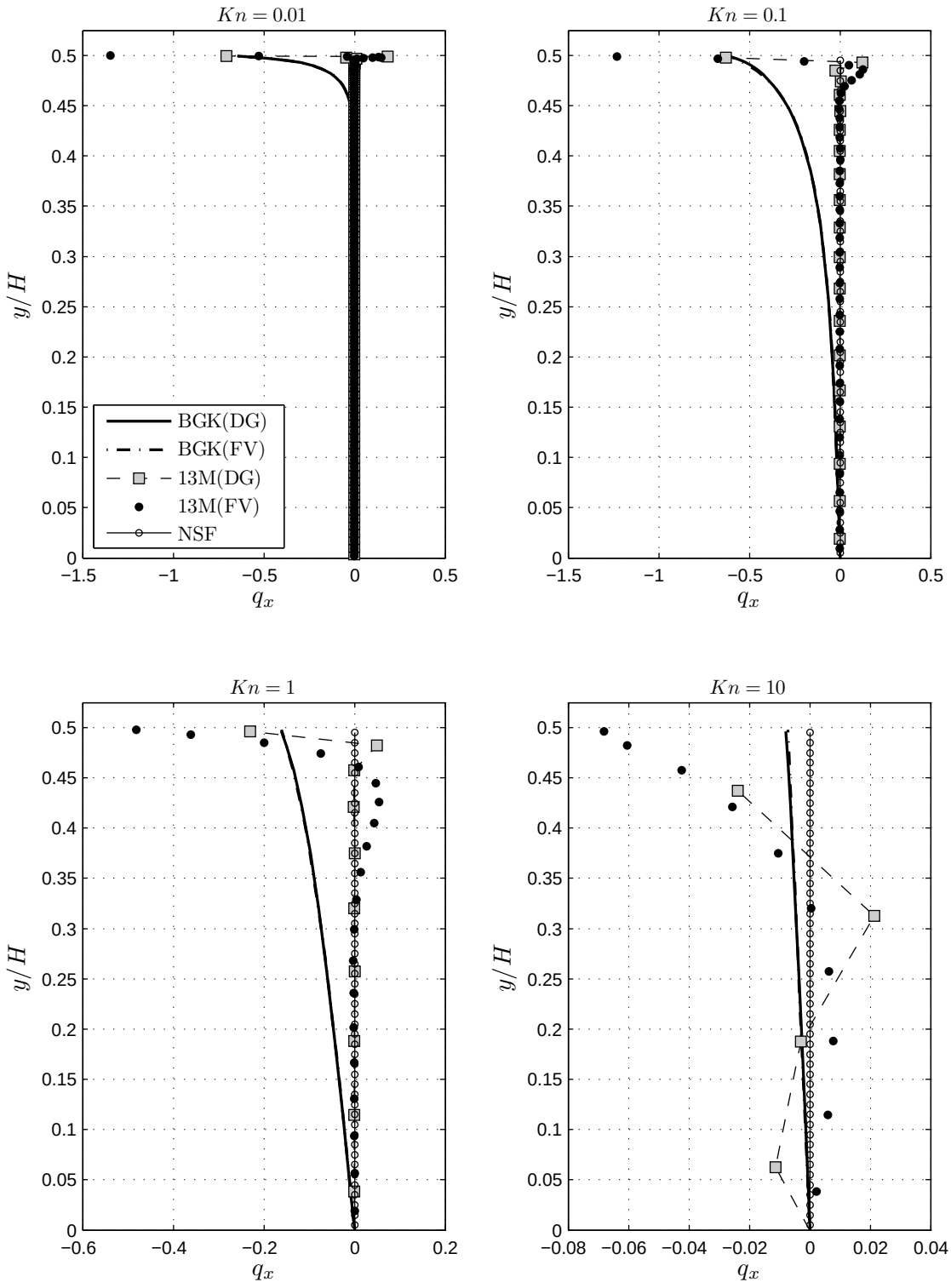

Figure 5.7: Couette solutions of $q_x(y)$ for all Knudsen numbers with 1–C boundary condition, except for NSF-solutions, which are obtained with 1$^{\text{st}}$-order velocity-slip boundary condition.

the Knudsen number is increasing; it then relaxes to zero towards the middle region. The thickness of the relaxation layer is approximately five mean free paths for $Kn = 0.01$ and 0.1, corresponding with the thickness of the Knudsen layer mentioned in Section 3.4.1. For $Kn = 1$ and $Kn = 10$, in which there are only one and one-tenth mean free paths in the channel cross-section, respectively, q_x does not have enough space to relax. The profiles are not quite tangent to the y-axis at $y = 0$.

For all Knudsen numbers, the boundary value of the 13M(FV) solution overestimate $q_x(H/2)$; the 13M(DG) value is rather accurate. Then, these values relax to the midstream value at a much faster rate than the BGK solution, even changing sign for DG discretization. It is interesting that the NSF system predicts $q_x = 0$ for all Knudsen numbers. In this respect, at least the boundary conditions for the 13M system are better than the NSF's velocity-slip model.

Figure 5.8 shows the profiles of q_y for all Knudsen numbers. Similarly to the profiles of u_x, results at $Kn = 0.01$ are hardly distinguishable, with the exception of the BGK solution obtained by FV. For other Knudsen numbers, the NSF system predicts the q_y-gradient better than the 13M system. Similar to the solutions of u_x and q_x in Figs. 5.4 and 5.7, the boundary condition of the 13M system is able to sense the BGK boundary value; however, the 13M solution relaxes too fast over the next few cells. At $Kn = 10$, the 13M solutions are also oscillatory and inaccurate. The NSF solutions, despite being just as incorrect, are at least smooth; probably because the NSF system is parabolic with an infinitesimal diffusion time-scale. In the 13M system, providing diffusion is the role of the source term; its diffusion time-scale (relaxation time τ) is finite, consequently the 13M system physically has less diffusion to damp out oscillations.

Figure 5.9 shows that, at $Kn = 0.01$ and 0.1, the quantity $q_y(y)$ computed with 13M(FV) exhibits a similar anomaly as observed previously in P_{xy}-profiles with 13M(FV). As shown in Fig. 5.1, grid refinement cannot extinguish these q_y-excursions

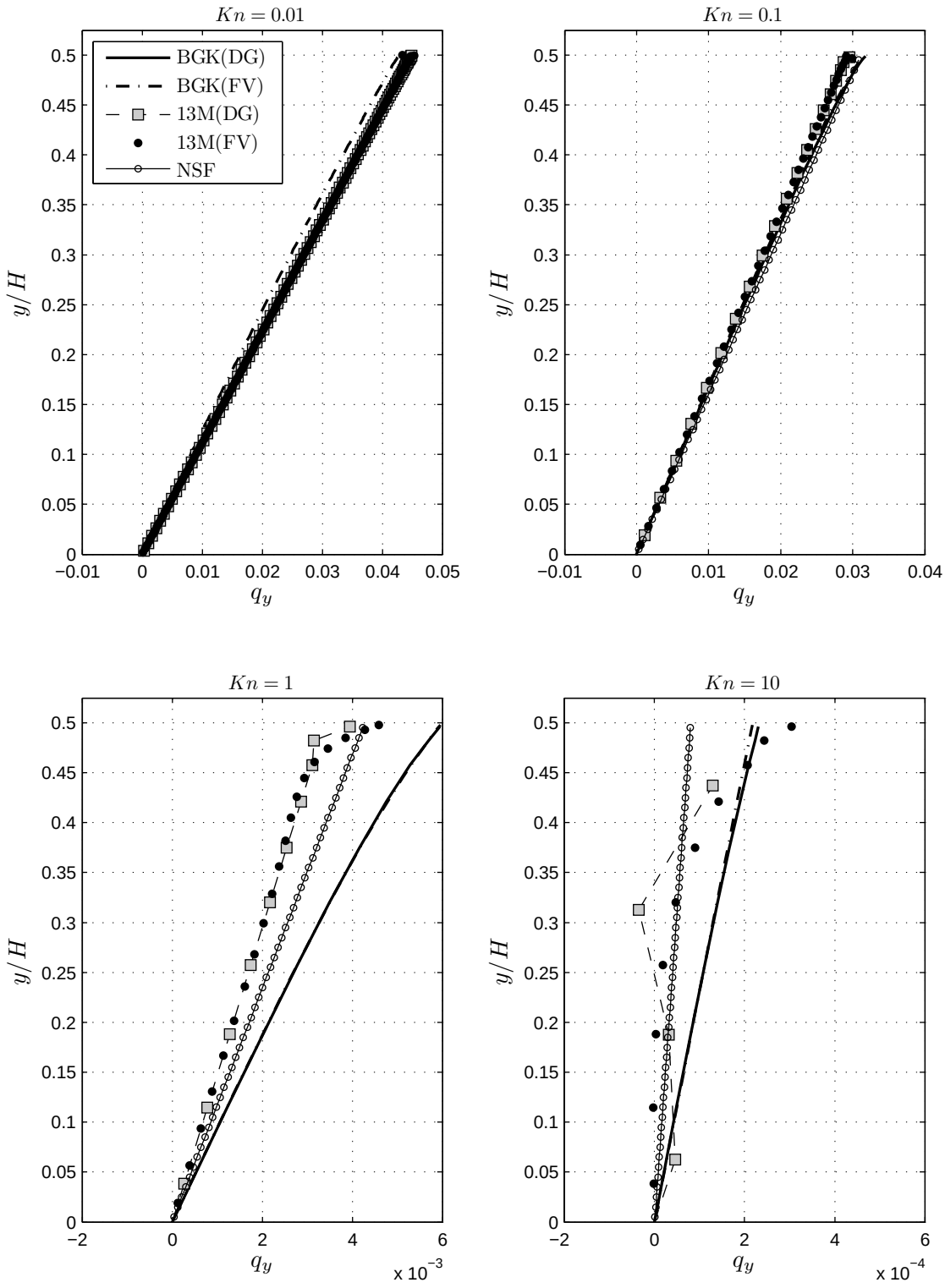

Figure 5.8: Couette solutions $q_y(y)$ for all Knudsen numbers with 1–C boundary condition, except for NSF-solutions, which are obtained with 1$^{\text{st}}$-order velocity-slip boundary condition.

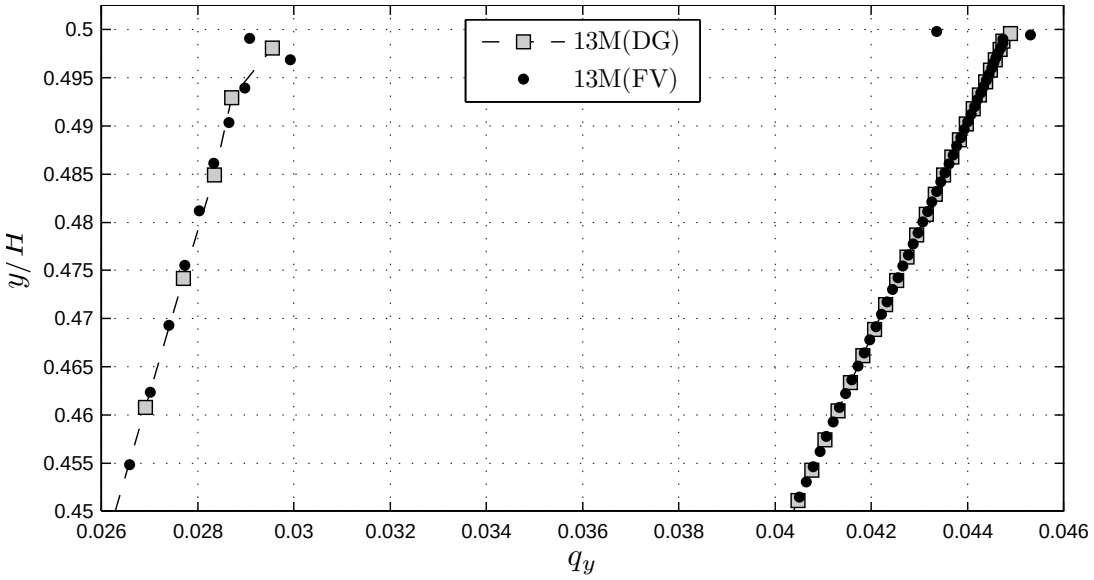

Figure 5.9: Couette solutions of $q_y(y)$ at $Kn = 0.01$ (right profile) and $Kn = 0.1$ (left profile), of the 13M system obtained with FV and DG discretizations with 1–C boundary condition.

either. Again the DG demonstrates its advantage, for its solutions do not have this behavior. These anomalies in FV discretization can be attributed to the reconstruction of the undivided gradients near the wall. As we use only a one-sided reconstruction for the boundary cell, the resulting quantities have no information of the wall's status, creating a solution mis-match at the boundary. It is then clear that grid refinement can not help to resolve the situation because we still use the one-sided reconstruction at the boundary.

5.1.3 Difference between 1–C and 2–C boundary conditions

It is important to mention that all numerical results presented in Figs. 5.4 to 5.9 are obtained with the 1–C boundary condition. Numerical experiments indicate that solutions of the BGK equation and the 13M system with the 2–C model are not meaningfully different. It turns out that this indifference stems from the nature of

incompressible laminar Couette flow:

$$\widetilde{T} = T^{\mathrm{w}}$$

$$\sqrt{\frac{R\widetilde{T}}{2\pi}}\frac{\widetilde{q}_y}{5\widetilde{p}R\widetilde{T}} \ll 1$$

$$\widetilde{P}_{yy} \simeq \widetilde{p}$$

From Table 4.4, with these assumptions, we obtain $C_1 \simeq 1$ and $C_2 \simeq 1$ for both solid-boundary models. The two models are indeed almost identical.

To study the possible difference, we simulate *static* Couette flow, i.e., $U = 0$, with different temperatures at the top and bottom walls to create a stronger vertical heat flux. The temperature of the top wall is kept at 350K, while the value at the bottom wall is still 300K. Solutions of the BGK equation and the 13M system, obtained only by the DG discretization, are presented in Fig. 5.10. The simulation is run at $Kn = 0.1$, which is a relatively high value, for which the 13M system approximate the BGK solution reasonably well.

There are significant differences between the 1–C and 2–C solutions of the BGK system. For this flow setting we expect the flow field to be essentially static, with the temperature increasing in the positive y-direction, while the density is decreasing in the same direction. We also expect a uniform profile of q_y. The solutions from the 1–C boundary condition confirms our expectations; with 2–C, only density and temperature behave as anticipated, while the results for vertical velocity and vertical heat flux are remarkably deviant. The profile of vertical velocity casts serious doubt on the validity of the 2–C boundary condition. Even though the non-penetration condition is enforced to assure that there is no vertical mass flux at the boundaries, u_y from 2–C has a clearly non-zero value at the top wall, -2.326×10^{-1} vs. -1.034×10^{-5} in the 1–C solution. The 2–C solution obviously is not yet steady; see further below.

Doing a grid-refinement study, we recognized that the 2–C requires a much finer

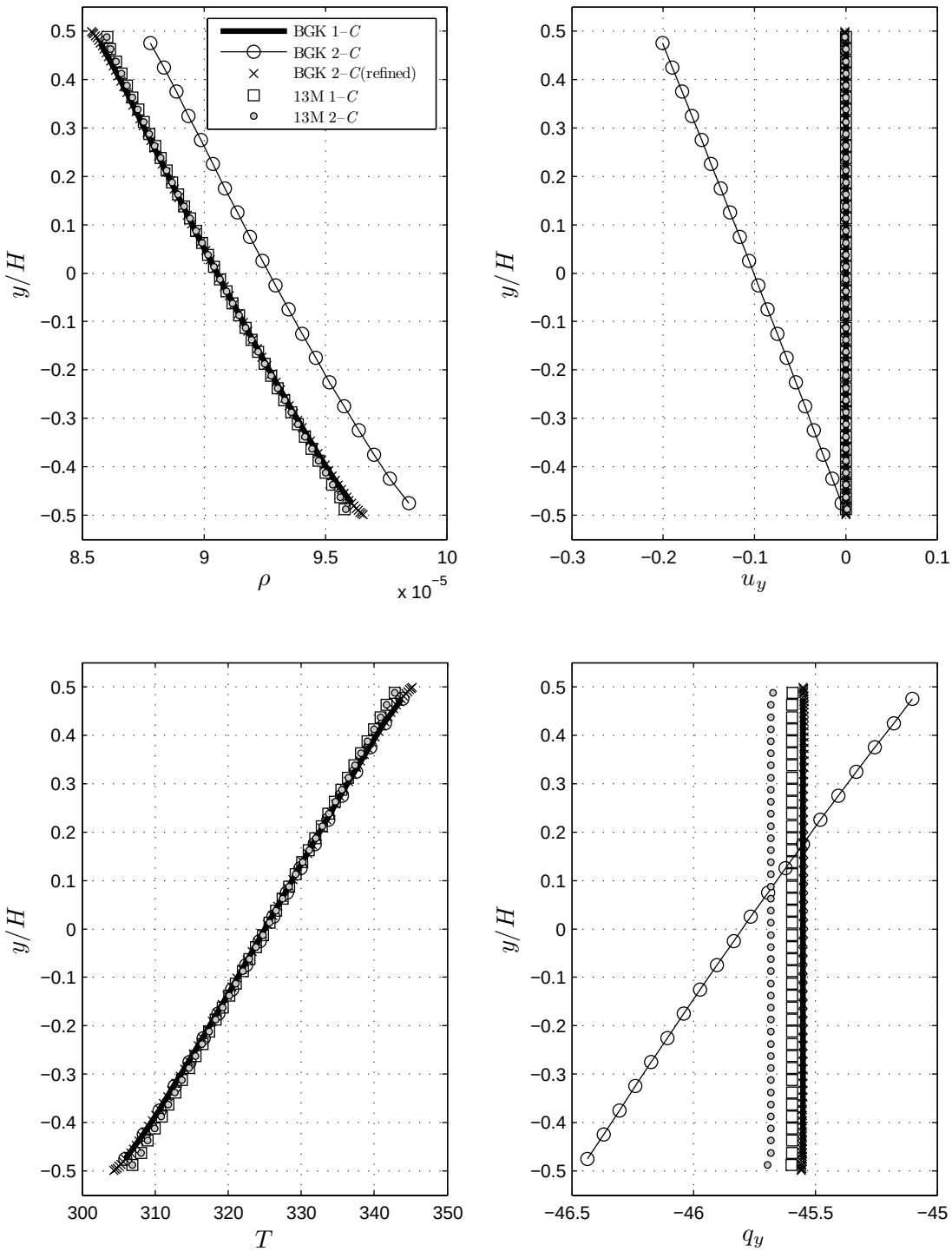

Figure 5.10: Results of static Couette flow where the top and bottom plates are kept at different temperature, with both 1–C and 2–C boundary conditions. The original grid of the BGK calculation is *uniform* 20-cell for both 1–C and 2–C models; the refined grid for 2–C model is *non-uniform* with 80 cells, in which $\Delta y_{\min}$ is approximately 25 times smaller than Δy of the uniform 20-cell grid.

grid to approach the quality of 1–C boundary condition, as shown in Fig. 5.10. We conjecture that this phenomenon is caused by the difference in calculating the flux at the boundary-interface when the 2–C boundary condition is used, and at all other interior interfaces. In the 2–C boundary condition, the wall's distribution function, from which we calculate the boundary-flux, is scaled by the *normalization* condition presented in Section 3.4.2. For the flux calculation at any interior interface, however, the distribution function is not normalized by the same condition, although we are at liberty to do so. Thus the calculation at the interior interfaces is fundamentally different from that at the boundary. This incompatibility also keeps the 2–C calculation unsteady, seemingly unable to converge to the low residual level achieved by simulations with the 1–C boundary condition.

We observed no fundamental difference between the 1–C and 2–C boundary conditions for the 13M system, with respect to both numerical accuracy and convergence. Both solutions conform to our expectations, and agree with the 1–C result of the BGK equation. Close inspection shows that the value of u_y at the top boundary cell of the 1–C and 2–C solutions are -6.756×10^{-5} and -1.077×10^{-3}, respectively. The difference in $u_y(H/2)$ is not as dramatic as for the BGK calculation, although the aforementioned inconsistency in normalization between wall-face and interfaces in the use of the 2–C boundary condition also exists in the 13M system. Since the 13M system contains much less information than the BGK equation, it is reasonable that the solution of the former is less sensitive than the latter to the normalization of the distribution function.

It is our opinion that the 2–C boundary condition is not yet mature. Further investigation into calculating the interface flux to be used in combination with this boundary-condition model is required. Specifically, the normalization of the distribution function implemented at the wall boundary may be required at any interface, if kinetic flux splitting is used. Whether this will lead to superior accuracy and

convergence remains to be seen.

5.1.4 Discontinuous Galerkin vs. Finite-Volume for discretization of the reduced BGK system

The advantage of DG over FV for the 13M system is clearly demonstrated in Section 5.1.2, as the former is able to produce solutions without wall-anomalies. The smoother profiles for u_x, q_x, and q_y obtained from the FV discretization appear to be a product of the associated higher numerical dissipation.

The DG phase-space discretization for the reduced BGK system has 16 times(!) more update equations than the FV discretization. The expense is much more than what we have to pay for using DG in the 13M system. The advantage of DG with regard to solutions in physical space was demonstrated previously by Fig. 5.6. The remaining question is whether using a DG discretization for velocity space is justified, because we are mostly interested in the macroscopic quantities, rarely in the details of the distribution function itself. Our motivation to discretize the velocity space by DG is that it more accurately preserves information about the Maxwellian distribution function in the calculation of the collision integral. As shown in Section 4.3.4, the calculation of the source-term volume integral, Eq. (4.80), preserved not just the cell-average but also the phase-space gradients of $\mathbf{\Phi}_{\mathrm{M}}$ in the computational cell (i, j, k, l). In contrast, Section 4.3.3 on FV-reconstruction shows that only the cell-average of $\mathbf{\Phi}_{\mathrm{M}}$ over the phase-space cell is preserved by the collision-integral calculation. When needed, phase-space gradients of $\mathbf{\Phi}_{\mathrm{M}}$ are calculated approximately by reconstruction using only cell-averages. By preserving accurate subcell information about $\mathbf{\Phi}_{\mathrm{M}}$, as with DG, the hope is to achieve conservation with a coarser grid. To test and compare the two discretizations we did two kinds of experiments, the first one a numerical projection-recovery exercise without added physics, the other one a simplified evolution by BGK.

Table 5.3: Relative error of the recovered temperature.

Grid	$\frac{\lvert T - T^{p1}\rvert}{T}$	
	FV	DG
4×4	1.602	5.317×10^{-1}
8×8	6.299×10^{-2}	7.211×10^{-3}
10×10	6.858×10^{-3}	5.241×10^{-4}
20×20	8.665×10^{-11}	1.760×10^{-12}
24×24	0	0
28×28	0	0
32×32	3.411×10^{-15}	3.411×10^{-15}
36×36	0	6.632×10^{-15}
40×40	0	3.411×10^{-15}
80×80	3.411×10^{-15}	0
160×160	3.411×10^{-15}	1.326×10^{-14}

First we take a Maxwellian distribution with zero bulk velocity and a temperature of 300K; the density is arbitrary. We take a coarse grid and discretize the distribution by projecting it onto a piecewise constant function (FV), after which gradients are computed by finite-differencing (reconstruction, see Section 4.2.2), or directly onto a piecewise linear basis (DG). From the resulting piecewise linear approximation (labeled $p1$) the macroscopic quantities density, velocity and temperature are recovered again, by taking the necessary zeroth, first and second moments in velocity space. These recovered quantities are not exactly equal to the values defining the original continuous Maxwellian. The error in the temperature is largest. We repeat the process on successively finer velocity grids; this leads to Table 5.3.

It is surprising to discover that the coarsest grid that is sufficient for conservation of the macroscopic quantities is 24×24, for *both* DG and FV methods. If indeed using DG in velocity space offers no accuracy advantage on these grids, it only makes the simulation unnecessarily expensive.

The advantage of DG and FV may therefore only exists for grids up to 20×20. To

investigate this, we do a second experiment on those grids. We test the two source-term discretizations in a Couette geometry in which the top and bottom walls remain static, and their temperatures are the same and kept constant. All flux calculations are omitted because we only want to test conservation under equilibrium conditions. Essentially, we try to solve the following equation,

$$\frac{\partial \mathbf{\Phi}}{\partial t} = -\frac{\mathbf{\Phi} - \mathbf{\Phi}_{\mathrm{M}}}{\tau},$$

by both FV and DG discretizations. It is unnecessary to discretize physical space as the solution would be universally uniform. The simulation is initialized by discretizing a Maxwellian distribution with zero bulk velocity and the value of the wall temperature, 300K, used throughout the gas. We start with a very coarse velocity grid and keep refining until we have conservation of mass, momentum and energy.

It turns out that none of the coarser grids (up to and including 20×20) yield sufficient accuracy for either FV or DG, although the time-derivative of temperature produced by DG is smaller than for FV. This translate into allowing a reduction of a factor 1.5–2 in the total number of velocity cells by DG with respect to FV while achieving the same temporal error. This does not justify the increased computational cost of using DG.

We conclude that the computation of gradients by reconstruction from cell averages, used in the FV method, is competitive with the independently computed gradients used in DG, for all grids where these methods are accurate enough in regard to conservation. The use of DG on the physical grid may still be advantageous, as shown earlier on Fig. 5.6.

It is worth to mention that DG discretization in velocity space is only $p1$, or piecewise linear. Since the distribution function is always smooth in those dimensions, it might be advantageous to use DG with $p2$ or higher-order representations as more

accurate information about the smooth Maxwellian distribution can be preserved. This option, however has not been explored in the current research project, for time-constraint reasons.

5.2 Numerical solutions of Poiseuille flow

In this section, we present solutions of Poiseuille flow obtained by methods described in Chapter IV. Most flow settings are the same as for the Couette-flow experiments. In view of the inaccuracy of the 13M solution at $Kn = 10$ shown in Section 5.1.2, Poiseuille flow is only simulated at $Kn = 0.01$, 0.1, and 1. To keep the flow field incompressible and laminar, we keep the temperature of the top and bottom plates the same. Both of them are static in Poiseuille flow; the flow field is driven by a pressure gradient. The value of the pressure gradient is chosen so that the value of the Mach number based on $u_x(0)$ is approximately 0.01. Similarly to Couette flow, solutions obtained from the 1–C and 2–C boundary conditions are practically the same, therefore only 1–C solutions are shown. For the NSF system, the second-order slip velocity by Sreekanth are used, as suggested by Tang et al. [63]. The temperature-jump condition does not matter because the temperature varies insignificantly.

5.2.1 Grid-convergence studies for Poiseuille flow

Unlike Couette flow, Poiseuille simulations by the BGK equation have to be executed as two-dimensional calculations. It is impossible to reduce them to quasi one-dimensional flows the way we derive the analytical NSF solutions (presented in Section 4.1.2). Contrary to the NSF system (4.1), the driving factor of Poiseuille flow, the pressure's x-gradient $\dfrac{\partial p}{\partial x}$, does not appear in expression of the BGK equation or its reduced system, Eq. (4.53).

In Poiseuille simulations, the channel length is finite and denoted by L. Pres-

sures at inlet and outlet are kept constant to create an unchanged pressure gradient throughout the simulations. Due to the finiteness in the x-dimension, it is necessary to formulate inflow and outflow conditions, in addition to solid-boundary conditions. For the BGK simulations, inflow/outflow boundary conditions have to supply information about the distribution function of all *positive-*v_x cells (inlet) and *negative-*v_x cells (outlet). This is rather inconceivable as we know nothing *a priori* about behavior of the distribution function; as best, we only have knowledge about macroscopic quantities at these locations. Therefore, we use the Grad13M distribution (2.30), which is the most non-equilibrium distribution available in this investigation, to generate the discrete values demanded by inflow/outflow conditions.

To use distribution function (2.30), we first need to estimate values of macroscopic quantities at the inlet/outlet. At the outlet, zero-x-gradient extrapolation is used to set the values. However, to satisfy the condition on the pressure drop, the obtained value of the pressure has to be substituted by a prescribed one; then value of the pressure tensor P_{ij} is modified accordingly,

$$P_{ij}|_{\text{outlet}} = \underbrace{p_{\text{outlet}}}_{\substack{\text{prescribed by given} \\ \text{pressure gradient}}} + \underbrace{p_{ij}}_{\substack{\text{calculated by zero-}x\text{-gradient extrapolation} \\ \text{from interior solutions}}} .$$

At the inlet, there are two ways to prescribe macroscopic quantities:

- They are computed from the interior solution also by zero-x-gradient extrapolation. Then, the prescribed value of inlet pressure is enforced in the same manner as the outlet pressure elaborated above. This configuration simulates the well-developed segment of Poiseuille flow, in which flow quantities do not vary significantly in the x-direction.

- The inlet flow is uniform in the y-direction, i. e., $\rho(y)$ and $u_x(y)$ are constant,

$P_{xy} = 0$, $q_x = q_y = 0$, p has the prescribed value of the inlet pressure, and $P_{xx} = P_{yy} = P_{zz} = p$. We intend to simulate both the boundary-layer-buildup and well-developed segments of Poiseuille flow.

In both options, there are regions at the inlet and outlet influenced by the inflow/outflow conditions, for which x-gradients of flow quantities are not negligible, unlike their behavior in the well-developed region. To have a valid comparison to the analytical NSF solutions, only numerical results in the latter region are used.

For Poiseuille simulations with the 13M system, inflow/outflow conditions have to supply only information about the macroscopic quantities. Therefore, formulations of the conditions for the BGK equation may and will be used, with omission of the last step of calculating the discrete distribution function from macroscopic quantities, assuming the former to have the Grad13M form.

In grid-convergence studies for Poiseuille simulations with the BGK equation, we employ the same procedure as used for Couette flow, explained in Section 5.1.1. The converged velocity-grid at $Kn = 0.1$ is 30×40, instead of just 16×40 as in Couette simulation. The rise in N_{v_x} is because flow quantities also vary in the x-direction, especially in regions effected by the inflow/outflow conditions. Our experience shows that the x-grid can be significantly coarser than the y-grid. A finer grid in x-dimension does not make a practical difference in the well-developed region; it only resolves the inflow/outflow regions better, in which we have no interest. We also observe that, for solutions in the well-developed region, refining y-grid is not rewarding. Solutions on the coarse grid lies on top of the finer-grid ones, similar to behavior demonstrated in Fig. 5.3 for Couette simulations.

As for Couette flow, we now turn to grid convergence for the Poiseuille experiments. Besides searching for the convergent phase-space grid, it is also necessary to determine the length of the channel, or rather its length/height ratio (L/H), that is sufficient for the well-developed region to exist. If it is too small, the whole channel

Table 5.4: Values of L/H for all Knudsen numbers of the Poiseuille simulations.

Kn	L/H
0.01	5
0.1	10
1	20
10	—

is occupied by regions which are under influence of the inflow/outflow conditions. At each Knudsen number, we start with a small value and keep increasing it until the well-developed region appears in the solution; the final values are shown in Table 5.4.

In simulations with the 13M system, studies were carried out to identify the convergent grid, which is only in physical space for this case. We use the L/H values determined previously from the BGK simulations as they are sufficient to also yield a well-developed region in the 13M solutions. We do not show results from the grid refinements, for they behave in the same manner as in the Couette simulations, presented previously in Fig. 5.1. All grids give approximately the same predictions for wall values; the profiles of u_x, q_x and q_y are oscillatory close to the wall and become worse on finer grids. Therefore, in Section 5.2.2, we show only results having the typical behavior but weaker oscillations.

As for Couette flow, we examined code efficiencies. Table 5.5 shows computational costs of simulations at $Kn = 0.1$, using the same personal computer as before for Couette calculations. Compared to those of the Couette simulations given in Table 5.1 (Section 5.1.1), a Poiseuille simulation with the BGK equation requires much more computer memory and runs significantly longer due to a much larger grid and longer convergence time. The 13M simulation uses just twice the amount of memory but runs significantly longer.

Table 5.5: Computational costs for Poiseuille-flow simulations at $Kn = 0.1$.

Physical model	Grid	Memory(KB)	Running time(s/h)
13M(DG)	25×40	5,448	1,989/0.553
BGK (DG)	25×40(phy.) 30×40(vel.)	1,266,752	—/373.722

5.2.2 Solutions for all Knudsen numbers

Figure 5.11 shows the results of u_x for all three Knudsen numbers. The NSF and 13M solutions again overestimate the amount of slip velocity, as in the solutions of Couette flow. The boundary condition for the 13M system gives a better prediction for the amount of slip compared to the NSF solution. However, the 13M system does not have enough physical diffusion to sustain a smooth relaxation to the velocity at mid-channel.

Distributions of the shear stress are shown in Fig. 5.12. Unlike for Couette flow, the solutions obtained from the NSF system and 13M system are almost on top of each other, and differ only slightly from the BGK solution.

The horizontal heat flux exhibits similar behavior as observed in the u_x profile. With regard to the vertical heat flux, the 13M system predicts the BGK solution quite well for $Kn = 0.01$ and 0.1, but not at 1.0. It is interesting that the NSF heat fluxes in Figs. 5.13 and 5.14 are totally different from those obtained from the BGK and 13M systems. A probable explanation is that simulations by the 13M and BGK are conducted as two-dimensional calculations, while the NSF system is first reduced to quasi one-dimensional problem before it is analytically solved. Therefore, to have a conclusive answer, it is better to numerically solve the NSF system on the same 2D configurations as the 13M and BGK. Unfortunately, due to a time constraint, we did not pursue this matter further.

In general, the 13M system has similar performance as shown previously in the

Couette simulations. The 13M solutions agree with the benchmark quite well for $Kn = 0.01$ and 0.1; at $Kn = 1$, its performance deteriorates quickly, but it is not less accurate than the NSF predictions. For all values of Kn, the 1–C solid-boundary condition of the 13M system approximates wall-values much better than the velocity-slip condition of the NSF system, but the inherent lack of physical diffusion prevents acquiring smoother and better profiles for u_x, q_x, and q_y.

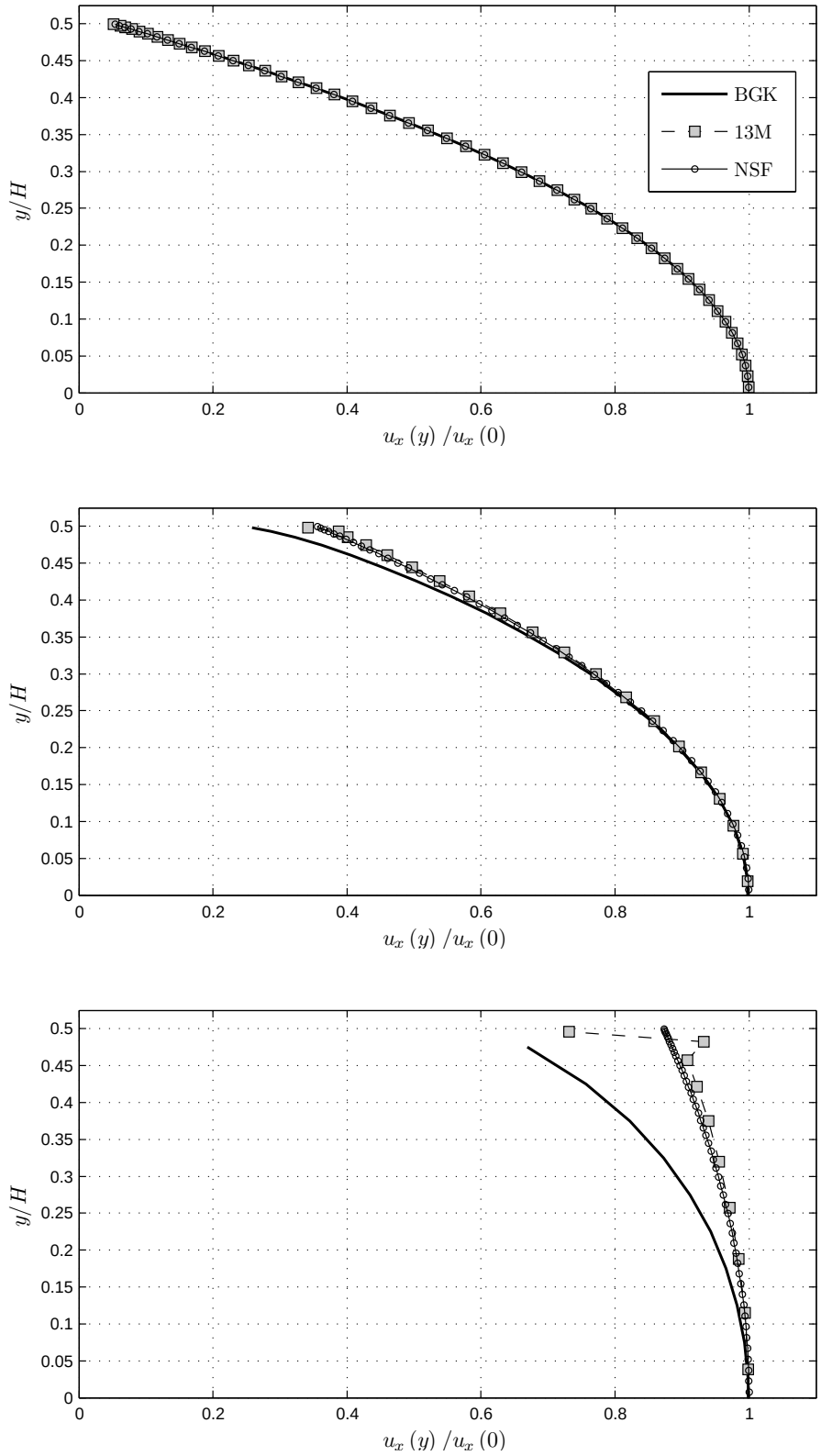

Figure 5.11: Normalized $u_x(y)$ of Poiseuille flow with 1–C boundary condition; Knudsen number is 0.01, 0.1, and 1 for the top, middle, and bottom plots respectively.

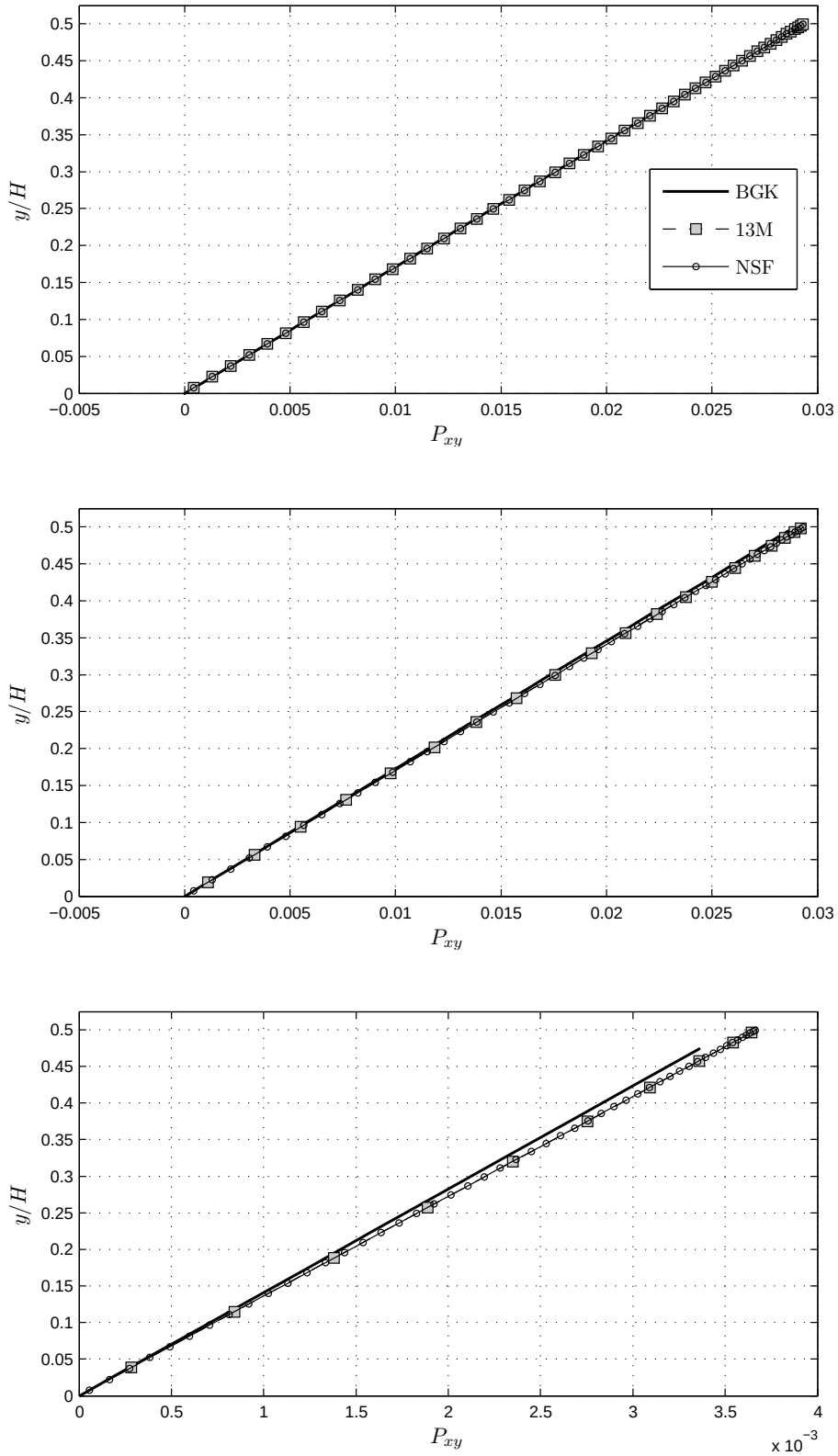

Figure 5.12: Solution of P_{xy} for Poiseuille flow with $1–C$ boundary condition; Knudsen number is 0.01, 0.1, and 1 for the top, middle, and bottom plots respectively.

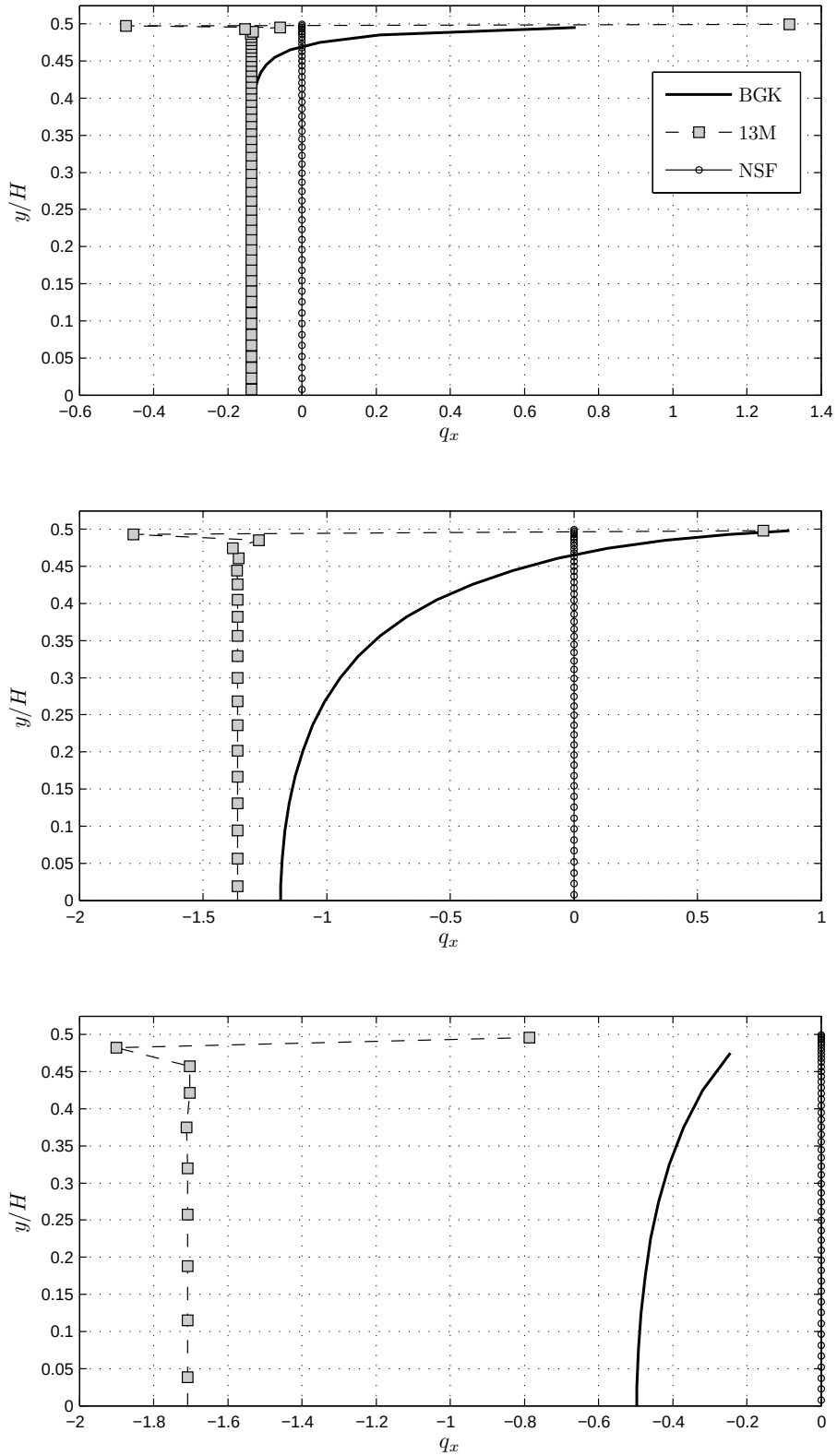

Figure 5.13: Solutions of $q_x(y)$ for Poiseuille flow with 1–C boundary condition; Knudsen number is 0.01, 0.1, and 1 for the top, middle, and bottom plots respectively.

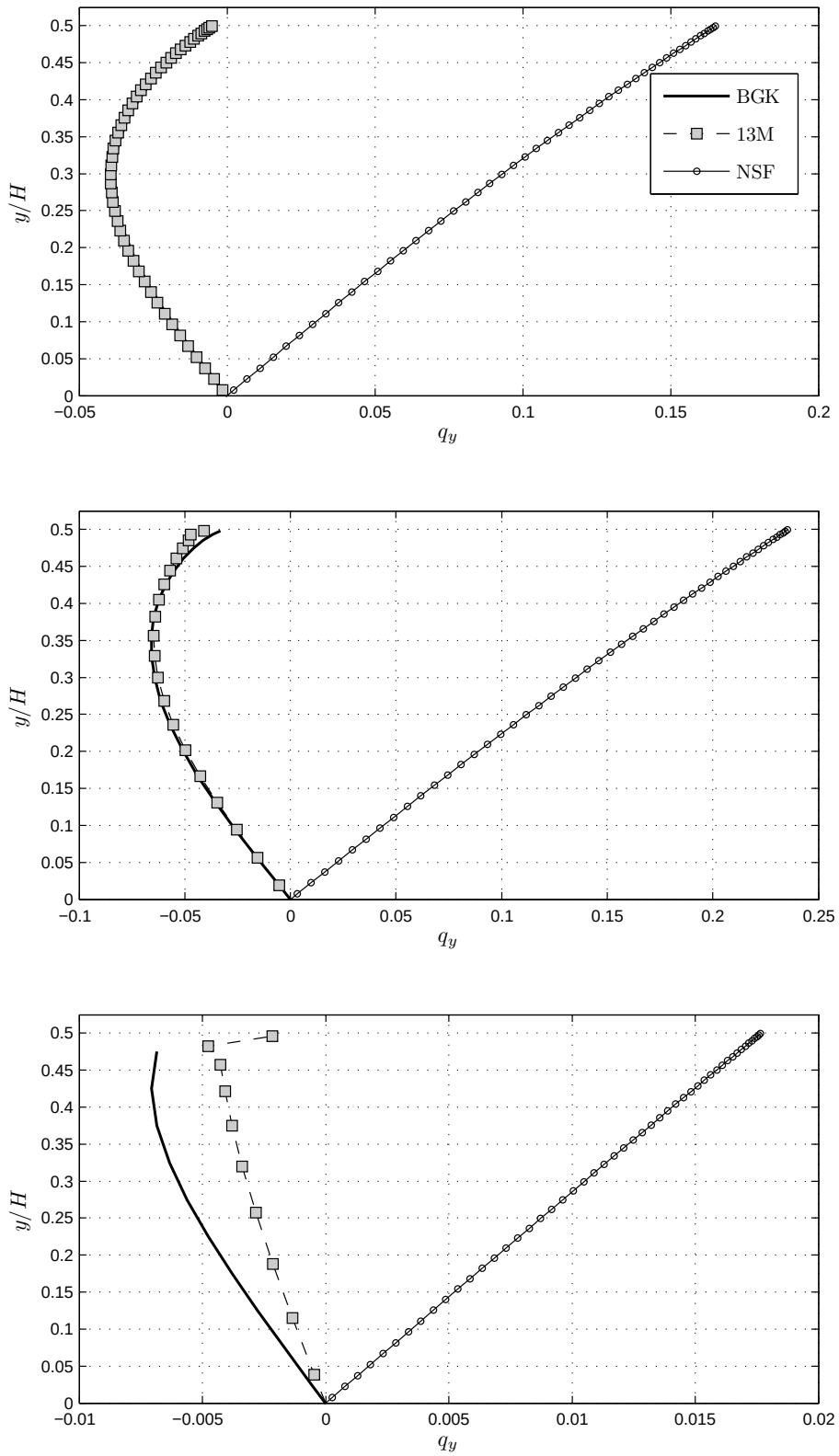

Figure 5.14: Solutions of $q_y(y)$ for Poiseuille flow with 1–C boundary condition; Knudsen number is 0.01, 0.1, and 1 for the top, middle, and bottom plots respectively.

CHAPTER VI

Concluding and looking forward

6.1 Conclusions

Hyperbolic-relaxation systems such as Grad's 13-moment (13M) system are derived by taking a number of velocity moments of the Boltzmann-BGK (BGK) equation. Such systems therefore contain less information about the fluid's evolution than the BGK equation, so it makes sense to use solutions of the latter equation to benchmark solutions of moment systems. In this dissertation we focused on developing physically plausible and unambiguous boundary conditions for moment systems. Such boundary conditions must be based on a microscopic view of the fluid-wall interaction; the conditions for the moment systems are conceptually the same as for the BGK equation. We formulated the 1–C condition based on non-penetration only, and the 2–C condition satisfying an additional normalization constraint. The chief effort in this dissertation is the validation of the 13M system by the BGK equation.

The nature of this validation has made the dissertation lopsided. No computational BGK code was available, and the development of the benchmark code was expected to take many times the effort of coding the 13M system. (And it did.) The main reason is that the BGK equation operates in phase-space, which includes up to 3 velocity coordinates. The development of a BGK code is laden with technical problems of data management under the constraint of parallelizability (by OpenMP);

still, production runs took days, slowing down the progress of the research. The BGK and 13M codes both existed with a Finite-Volume (FV) and a Discontinuous Galerkin (DG) option. In order to ensure that all our flow codes produce the correct physics, we spent great efforts in running grid-convergence studies for each one of them. This helped us make the most efficient grid selection for each Knudsen number.

We first discuss the results of our experiments relating to the physics of the flow, then we turn to discussing the differences between the two numerical discretization approaches.

Our first series of experiments, based on low-speed Couette flow with zero wall-temperature difference, was meant to examine the accuracy of the velocity slip of the 13M system. The benchmark BGK solution was obtained and also an incompressible Navier–Stokes–Fourier (NSF) solution, for which Maxwell's first-order condition provided the velocity slip. The Knudsen number ranged from 0.01 to 10. The 13M system consistently predicts a flow velocity at the wall that is closer to the BGK solution than NSF does. The 13M velocity profiles do show a difficulty with relaxing toward the mid-channel value. The profiles are not monotone and become increasingly oscillatory with increasing Kn. Similar behavior is seen in the profiles of q_x and q_y. We attribute this to a lack of inherent dissipation in the system. In this set of experiments it made no difference whether boundary condition $1\text{–}C$ or $2\text{–}C$ was used. Note that our total experience in DG is only with the piecewise-linear ($p1$) discretization; we find it impossible to guess how higher-order DG discretization would react to the $1\text{–}C$ condition. Finally, it was noticed that the NSF result for q_x is always zero, which is incorrect.

The next set of experiments was static Couette flow (zero wall speeds) with an appreciable wall-temperature difference. (For this flow an analytical NSF solution does not exist.) These experiments were needed to bring out the difference between the $1\text{–}C$ and $2\text{–}C$ conditions, which is sensitive to q_y. The 13M solution turned out to

be insensitive to the change in boundary condition, but the BGK calculations became slow to converge to the steady solutions. Where convergence was reached, the residual remained at a higher level than with 1–C. We suspect that the extra normalization condition imposed at the wall may actually have to be imposed at all interior cell-faces, for a consistent treatment. Since the 2–C condition is still problematic when combined with the BGK equation, and it does not seem to make a difference with regard to 1–C when used with the 13M system, it seems unnecessary to pursue the latter combination at this time.

The last series of experiments was based on a low-speed, pressure-driven Poiseuille flow with equal wall temperatures. This time we used a second-order slip condition to obtain the NSF solution. The earlier findings about the 13M slip velocity and the profile shapes were confirmed for this flow as well; also, the NSF results for velocity and shear stress were similar in quality to the Couette results. However, the NSF heat flux q_y was surprisingly inaccurate; it has the wrong sign.

We now turn to the comparison between the FV and DG discretization options in the code. Both versions were run for Couette flow; the runs for Poiseuille flow were all done with DG. In general, the solutions generated with DG were of a somewhat better quality than those of FV. In solving the 13M system, two differences stand out:

- Away from the wall the DG results relax to the constant or linear solution in the channel more rapidly than the FV results; the latter seem smeared out and oscillate over a longer distance. We suspect this is caused by the numerical dissipation in FV being stronger than in DG, but did not gather supporting evidence.

- At the wall the FV solutions for P_{xy} and q_y exhibit anomalous excursions, which we trace back to the one-sided reconstruction used in the cell abutting the wall. This anomaly scales with the mesh width, just like oscillations around numerical

shock wave.

When solving the BGK equation with FV we observe the same wall anomaly as with the 13M system, but only in the results for P_{xy}. The amplitude of the anomalous excursions is very small. A surprising finding was that using piecewise linear DG in velocity space was not superior to using FV with gradients reconstructed from cell averages. On coarse grids DG in velocity space does have better accuracy than FV, but this accuracy is not high enough to preserve a steady state. On finer grids both perform adequately, but the FV code runs an order of magnitude faster than the DG code. Thus, it is not efficient to use DG in velocity space. In physical space, though, DG is still preferable, if only because it does not suffer from the wall anomaly mentioned above.

To conclude the section, we turn to the important question of the utility of the 13M system. Our experiments show that all wall quantities (u_x, P_{xy}, q_x, q_y) compare reasonably well with the values produced by the BGK equation, up to and including $Kn = 1$. In contrast, the NSF system with a velocity-slip condition yields only a reasonable value for P_{xy}. On the other hand, the profiles of u_x, q_x and q_y away from the wall as computed by 13M do not match the smoothness of the BGK solutions, particularly for $Kn \leq 1$. We therefore recommend the use of the 13M system in applications where it is especially important to have accurate wall values, and the solutions away from the wall are less important. The description is suited for subsonic and transonic flows, at low to moderate Knudsen numbers.

6.2 Looking forward

In retrospect it seems obvious that we should have used the 1–C boundary condition also in combination with the Navier–Stokes–Fourier system, rather than the macroscopic first- and second-order velocity-slip conditions. This, however, would

necessitate the development of a full-blown NSF code (FV as well as DG), as an analytic solution appears not feasible. This did not fit into the scope of our doctoral project. For future research we may have to develop an NSF code anyway, so we plan to develop the equivalent of the 1–C condition for use with the NSF equation and experiment with it. This might improve the capability of NSF to predict flows with not-so-small Knudsen number.

Another possibility of extending the present work is to experiment with a BGK code that uses the FV discretization in velocity space and DG in physical space. This will combine the accuracy of DG with the efficiency of FV.

We may also consider applying the fully Discontinuous Galerkin BGK code to more violent flows like flow with a shock wave where the distribution function deviates strongly from a Maxwellian. In this case, a DG discretization in velocity space, especially when using higher-order polynomials, may become efficient.

Finally, we are considering to improve the 1–C boundary condition by including information from cells further away from the wall. We hope this may improve the solution profiles away from the wall.

APPENDICES

APPENDIX A

The half-velocity-space integrals of the Maxwellian distribution function in two-dimensional physical space

The Maxwellian distribution function has the following general form

$$f_{\mathrm{M}}(\mathbf{v}) = \frac{\rho}{(2\pi RT)^{3/2}} \exp\left[-\frac{(\mathbf{v}-\mathbf{u})^2}{2RT}\right].$$

The velocity vector is $\mathbf{u} = (u_x, u_y, 0)$. In the following expressions, the "+" and "−" indicate the result for the *positive* half-velocity-space $(0 \to +\infty)$ and *negative* half-velocity-space $(-\infty \to 0)$, respectively.

A.1 Half-v_x-space integrals

These are results of the half-v_x-space integrals of the Maxwellian distribution function:

$$\iint_{-\infty}^{+\infty} \left(\int_{0(-\infty)}^{+\infty(0)} \mathbf{W}(\mathbf{v})\, f_{\mathrm{M}}(\mathbf{v})\, \mathrm{d}v_x \right) \mathrm{d}v_y\, \mathrm{d}v_z$$
$$= \frac{1}{2} \left[1 \pm \mathrm{erf}\left(\frac{u_x}{\sqrt{2RT}} \right) \right] \mathbf{ErfTerm} \pm \sqrt{\frac{RT}{2\pi}} \exp\left[-\frac{u_x^2}{2RT} \right] \mathbf{ExpTerm}; \quad \text{(A.1)}$$

the expressions for **ErfTerm** and **ExpTerm** are shown in Table A.1.

Table A.1: The values of **ErfTerm** and **ExpTerm** in the half-v_x-space integrals, Eq. (A.1), of the Maxwellian distribution function.

$\mathbf{W}(\mathbf{v})$	**ErfTerm**	**ExpTerm**
1	ρ	0
v_x	ρu_x	ρ
$v_x v_x$	$\rho u_x^2 + p$	ρu_x
$v_x v_y$	$\rho u_x u_y$	ρu_y
$v_x v_x^2$	$u_x \left(\rho u_x^2 + 3p\right)$	$\rho u_x^2 + 2p$
$v_x v_y^2$	$u_x \left(\rho u_y^2 + p\right)$	$\rho u_y^2 + p$
$v_x v_z^2$	$u_x p$	p
$v_x v_x v_y$	$u_y \left(\rho u_x^2 + p\right)$	$\rho u_x u_y$
$v_x v_x \mathbf{v}^2$	$\rho u_x^2 \mathbf{u}^2 + 5pRT + p\left(7u_x^2 + \mathbf{u}^2\right)$	$u_x \left(\rho \mathbf{u}^2 + 7p\right)$
$v_x v_y \mathbf{v}^2$	$u_x u_y \left(\rho \mathbf{u}^2 + 7p\right)$	$u_y \left(\rho \mathbf{u}^2 + 6p\right)$

A.2 Half-v_y-space integrals

These are results of the half-v_y-space integrals of the Maxwellian distribution function:

$$\iint_{-\infty}^{+\infty} \left(\int_{0(-\infty)}^{+\infty(0)} \mathbf{W}(\mathbf{v})\, f_{\mathrm{M}}(\mathbf{v})\, \mathrm{d}v_y \right) \mathrm{d}v_x\, \mathrm{d}v_z$$
$$= \frac{1}{2} \left[1 \pm \mathrm{erf}\left(\frac{u_y}{\sqrt{2RT}} \right) \right] \mathbf{ErfTerm} \pm \sqrt{\frac{RT}{2\pi}} \exp\left[-\frac{u_y^2}{2RT} \right] \mathbf{ExpTerm}; \quad \text{(A.2)}$$

the expressions for **ErfTerm** and **ExpTerm** are shown in Table A.2.

Table A.2: The values of **ErfTerm** and **ExpTerm** in the half-v_y-space integrals, Eq. (A.2) of the Maxwellian distribution function.

$\mathbf{W}(\mathbf{v})$	**ErfTerm**	**ExpTerm**
1	ρ	0
v_y	ρu_y	ρ
$v_y v_x$	$\rho u_x u_y$	ρu_x
$v_y v_y$	$\rho u_y^2 + p$	ρu_y
$v_y v_x^2$	$u_y \left(\rho u_x^2 + p \right)$	$\rho u_x^2 + p$
$v_y v_y^2$	$u_y \left(\rho u_y^2 + 3p \right)$	$\rho u_y^2 + 2p$
$v_y v_z^2$	$u_y p$	p
$v_y v_x v_y$	$u_x \left(\rho u_y^2 + p \right)$	$\rho u_x u_y$
$v_y v_x \mathbf{v}^2$	$u_x u_y \left(\rho \mathbf{u}^2 + 7p \right)$	$u_x \left(\rho \mathbf{u}^2 + 6p \right)$
$v_y v_y \mathbf{v}^2$	$\rho u_y^2 \mathbf{u}^2 + 5pRT + p \left(7u_y^2 + \mathbf{u}^2 \right)$	$u_y \left(\rho \mathbf{u}^2 + 7p \right)$

APPENDIX B

The half-velocity-space integrals of Grad's 13-moment distribution function in two-dimensional physical space

Grad's 13-moment distribution function has the following general form

$$f_{\text{Grad13M}}(\mathbf{v}) = \frac{\rho}{(2\pi RT)^{3/2}} \exp\left[-\frac{(\mathbf{v}-\mathbf{u})^2}{2RT}\right] \times \left[1 + \frac{P_{ij} - p\delta_{ij}}{2pRT}(v_i - u_i)(v_j - u_j) + \frac{q_k(v_k - u_k)}{pRT}\left(\frac{(\mathbf{v}-\mathbf{u})^2}{5RT} - 1\right)\right].$$

In 2-D flow:

- the velocity vector $\mathbf{u} = (u_x, u_y, 0)$,
- the pressure tensor $\mathbf{P} = \begin{bmatrix} P_{xx} & P_{xy} & 0 \\ P_{xy} & P_{yy} & 0 \\ 0 & 0 & P_{zz} \end{bmatrix}$,
- the heat-flux vector $\mathbf{q} = (q_x, q_y, 0)$.

In the following expressions, the "+" and "−" indicate the result for the *positive* half-velocity-space $(0 \to +\infty)$ and *negative* half-velocity-space $(-\infty \to 0)$, respectively.

B.1 Half-v_x-space integrals

These are results of the half-v_x-space integrals of the Grad13M distribution function:

$$\iint_{-\infty}^{+\infty} \left(\int_{0(-\infty)}^{+\infty(0)} \mathbf{W}(\mathbf{v})\, f_{\text{Grad13M}}(\mathbf{v})\, \mathrm{d}v_x \right) \mathrm{d}v_y\, \mathrm{d}v_z$$
$$= \frac{1}{2}\left[1 \pm \operatorname{erf}\left(\frac{u_x}{\sqrt{2RT}}\right)\right] \mathbf{ErfTerm} \pm \sqrt{\frac{RT}{2\pi}} \exp\left[-\frac{u_x^2}{2RT}\right] \mathbf{ExpTerm}; \quad \text{(B.1)}$$

the expressions for **ErfTerm** and **ExpTerm** are shown in Table B.1.

B.2 Half-v_y-space integrals

These are results of the half-v_y-space integrals of the Grad13M distribution function:

$$\iint_{-\infty}^{+\infty} \left(\int_{0(-\infty)}^{+\infty(0)} \mathbf{W}(\mathbf{v})\, f_{\text{Grad13M}}(\mathbf{v})\, \mathrm{d}v_y \right) \mathrm{d}v_x\, \mathrm{d}v_z$$
$$= \frac{1}{2}\left[1 \pm \operatorname{erf}\left(\frac{u_y}{\sqrt{2RT}}\right)\right] \mathbf{ErfTerm} \pm \sqrt{\frac{RT}{2\pi}} \exp\left[-\frac{u_y^2}{2RT}\right] \mathbf{ExpTerm}; \quad \text{(B.2)}$$

the expressions for **ErfTerm** and **ExpTerm** are shown in Table B.2.

Table B.1: The values of **ErfTerm** and **ExpTerm** in the half-v_x-space integrals, Eq. (B.1), of the distribution function f_{Grad13M}.

$\mathbf{W}(\mathbf{v})$	**ErfTerm**	**ExpTerm**
1	ρ	$\frac{\rho u_x}{2RT}\left(1-\frac{P_{xx}}{p}\right)+\frac{q_x}{5\left(RT\right)^2}\left(\frac{u_x^2}{RT}-1\right)$
$v_x\left(1\right)$	ρu_x	$\frac{\rho}{2}\left(1+\frac{P_{xx}}{p}-\frac{2u_xq_x}{5pRT}\right)$
$v_x\left(v_x\right)$	$\rho u_x^2+P_{xx}$	$\rho u_x+\frac{2q_x}{5RT}$
$v_x\left(v_y\right)$	$\rho u_xu_y+P_{xy}$	$\frac{\rho u_y}{2}\left(1+\frac{P_{xx}}{p}-\frac{2u_xq_x}{5pRT}\right)+\frac{q_y}{5RT}$
$v_x\left(v_x^2\right)$	$u_x\left(\rho u_x^2+3P_{xx}\right)+\frac{6q_x}{5}$	$\rho u_x^2+3P_{xx}-p$
$v_x\left(v_y^2\right)$	$u_x\left(\rho u_y^2+P_{yy}\right)+2u_yP_{xy}+\frac{2q_x}{5}$	$\frac{\rho u_y^2}{2}\left(1+\frac{P_{xx}}{p}-\frac{2u_xq_x}{5pRT}\right)-\frac{u_xq_x-2u_yq_y}{5RT}+\frac{P_{xx}+2P_{yy}-p}{2}$
$v_x\left(v_z^2\right)$	$u_xP_{zz}+\frac{2q_x}{5}$	$\frac{5p-P_{xx}-2P_{yy}}{2}-\frac{u_xq_x}{5RT}$
$v_x\left(v_xv_y\right)$	$u_y\left(\rho u_x^2+P_{xx}\right)+2u_xP_{xy}+\frac{2q_y}{5}$	$\rho u_xu_y+2P_{xy}+\frac{2u_yq_x}{5RT}$
$v_x\left(v_x\mathbf{v}^2\right)$	$u_x^2\left(\rho\mathbf{u}^2+4P_{xx}+3p\right)+RT\left(7P_{xx}-2p\right)+\cdots$ $+\mathbf{u}^2P_{xx}+4u_xu_yP_{xy}+4\left(8u_xq_x+u_yq_y\right)/5$	$u_x\left(\rho\mathbf{u}^2+2p+5P_{xx}\right)+4u_yP_{xy}+\frac{2q_x}{5}\left(18+\frac{u_y^2}{RT}\right)$
$v_x\left(v_y\mathbf{v}^2\right)$	$u_xu_y\left(\rho\mathbf{u}^2+2P_{xx}+2P_{yy}+3p\right)+\cdots$ $+3\mathbf{u}^2P_{xy}+7RTP_{xy}+\frac{14}{5}\left(u_xq_y+u_yq_x\right)$	$\frac{\rho u_y^3}{2}\left(1+\frac{P_{xx}}{p}-\frac{2u_xq_x}{5pRT}\right)+u_xu_y\left(\rho u_x-\frac{4q_x}{5RT}\right)+\cdots$ $+3u_xP_{xy}+2u_y\left(2P_{xx}+P_{yy}\right)+\frac{q_y}{5}\left(18+\frac{3u_y^2}{RT}\right)$

Table B.2: The values of **ErfTerm** and **ExpTerm** in the half-v_y-space integrals, Eq. (B.2), of the distribution function f_{Grad13M}.

$\mathbf{W}(\mathbf{v})$	**ErfTerm**	**ExpTerm**
1	ρ	$\frac{\rho u_y}{2RT}\left(1-\frac{P_{yy}}{p}\right)+\frac{q_y}{5\left(RT\right)^2}\left(\frac{u_y^2}{RT}-1\right)$
$v_y\left(1\right)$	ρu_y	$\frac{\rho}{2}\left(1+\frac{P_{yy}}{p}-\frac{2u_yq_y}{5pRT}\right)$
$v_y\left(v_x\right)$	$\rho u_xu_y+P_{xy}$	$\frac{\rho u_x}{2}\left(1+\frac{P_{yy}}{p}-\frac{2u_yq_y}{5pRT}\right)+\frac{q_x}{5RT}$
$v_y\left(v_y\right)$	$\rho u_y^2+P_{yy}$	$\rho u_y+\frac{2q_y}{5RT}$
$v_y\left(v_x^2\right)$	$u_y\left(\rho u_x^2+P_{xx}\right)+2u_xP_{xy}+\frac{2q_y}{5}$	$\frac{\rho u_x^2}{2}\left(1+\frac{P_{yy}}{p}-\frac{2u_yq_y}{5pRT}\right)+\frac{2u_xq_x-u_yq_y}{5RT}+\frac{2P_{xx}+P_{yy}-p}{2}$
$v_y\left(v_y^2\right)$	$u_y\left(\rho u_y^2+3P_{yy}\right)+\frac{6q_y}{5}$	$\rho u_y^2+3P_{yy}-p$
$v_y\left(v_z^2\right)$	$u_yP_{zz}+\frac{2q_y}{5}$	$\frac{5p-2P_{xx}-P_{yy}}{2}-\frac{u_yq_y}{5RT}$
$v_y\left(v_xv_y\right)$	$u_x\left(\rho u_y^2+P_{yy}\right)+2u_yP_{xy}+\frac{2q_x}{5}$	$\rho u_xu_y+2P_{xy}+\frac{2u_xq_y}{5RT}$
$v_y\left(v_x\mathbf{v}^2\right)$	$u_xu_y\left(\rho\mathbf{u}^2+2P_{xx}+2P_{yy}+3p\right)+\cdots$ $+3\mathbf{u}^2P_{xy}+7RTP_{xy}+\frac{14}{5}\left(u_xq_y+u_yq_x\right)$	$\frac{\rho u_x^3}{2}\left(1+\frac{P_{yy}}{p}-\frac{2u_yq_y}{5pRT}\right)+u_xu_y\left(\rho u_y-\frac{4q_y}{5RT}\right)+\cdots$ $+2u_x\left(P_{xx}+2P_{yy}\right)+3u_yP_{xy}+\frac{q_x}{5}\left(18+\frac{3u_x^2}{RT}\right)$
$v_y\left(v_y\mathbf{v}^2\right)$	$u_y^2\left(\rho\mathbf{u}^2+4P_{yy}+3p\right)+RT\left(7P_{yy}-2p\right)+\cdots$ $+\mathbf{u}^2P_{yy}+4u_xu_yP_{xy}+4\left(u_xq_x+8u_yq_y\right)/5$	$u_y\left(\rho\mathbf{u}^2+2p+5P_{yy}\right)+4u_xP_{xy}+\frac{2q_y}{5}\left(18+\frac{u_x^2}{RT}\right)$

BIBLIOGRAPHY

BIBLIOGRAPHY

[1] M. Al-Ghoul and B. C. Eu. Generalized hydrodynamics and shock waves. *Physical Review E*, 56(3):2981–2992, 1997. 2.3.2

[2] H. Alsmeyer. Density profiles in argon and nitrogen shock waves measured by the absorption of an electron beam. *Journal of Fluid Mechanics*, 74(APR6): 497–513, 1976. 2.3.2

[3] V. V. Aristov. *Direct methods for solving the Boltzmann equation and study of nonequilibrium flows*. Fluid mechanics and its applications. Kluwer Academic Publishers, Dprdrecht ; Boston, 2001. 4.3.2

[4] J. Au and Wolf Weiss. Shock wave structure calculations with extended thermodynamics of many moments. In Vincenzo Ciancio, Andrea Donato, Francesco Oliveri, and Salvatore Rionero, editors, *10th Conference on Waves and Stability in Continuous Media*, page 9, Vulcano (Eolie Islands), Italy, 2001. World Scientific. 2.3.2

[5] P. L. Bhatnagar, E. P. Gross, and M. Krook. A model for collision processes in gases. I. Small amplitude processes in charged and neutral one-component systems. *Physical Review*, 94(3):511–525, 1954. I, 2.1.2

[6] G. A. Bird. Aspects of the structure of strong shock waves. *The Physics of Fluids*, 13(5):1172–1177, 1970. 2.3.2

[7] G. A. Bird. *Molecular Gas Dynamics and the Direct Simulation of Gas Flows*. Oxford Science Publications, 1994. 1.1.1, 1.1, 2.1, 2.1.1, 2.3.2, 3.1.3, 3.1.3

[8] Shawn Lee Brown. *Approximate Riemann Solvers for Moment Models of Dilute Gases*. PhD thesis, University of Michigan, 1996. URLs http://aerospace.engin.umich.edu/cfd/publications.htm or http://proquest.umi.com.proxy.lib.umich.edu/pqdweb?did=742527941&sid=1&Fmt=2&clientId=17822&RQT=309&VName=PQD (authentication may be required). I, I, 1.1, 1.2, 2.1.2, 2.3.2, 4.2.4

[9] John C. Butcher. *Numerical Methods for Ordinary Differential Equations*. John Wiley & Sons, Hoboken, NJ, second edition, 2008. 4.2

[10] D. S. Butler and W. M. Anderson. Shock structure calculations by an orthogonal expansion method. In C. L. Brundin, editor, *The fifth international symposium*

on Rarefied Gas Dynamics, volume 1 of *Advances in Applied Mechanics*, page 731. Academic Press, 1967. 2.3.2

[11] C. Cercignani and Adelia Daneri. Flow of a rarefied gas between two parallel plates. *Journal of Applied Physics*, 34(12):3509, 1963. 4.1

[12] Carlo Cercignani. *Theory and application of the Boltzmann equation*. Elsevier, New York, 1975. 2.1.2, 2.1.2, 3.1.1, 3.1.2, 3.1.3

[13] Sydney Chapman and T. G. Cowling. *The mathematical theory of non-uniform gases*. Cambridge University Press, third edition, 1970. 1.1.3, b

[14] C. K. Chu. Kinetic-theoretic description of formation of a shock wave. *Physics of Fluids*, 8(1):12–22, 1965. 4.3.1

[15] C. K. Chu. Kinetic-theoretic description of shock wave formation. II. *Physics of Fluids*, 8(8):1450–1455, 1965. 4.3.1

[16] Bernardo Cockburn and Chi-Wang Shu. Runge–Kutta discontinuous Galerkin methods for convection-dominated problems. *Journal of Scientific Computing*, 16(3):173–261, 2001. 4.2.1, 4.2

[17] W. J. Coirier and K. G. Powell. Solution-adaptive cartesian cell approach for viscous and inviscid flows. *AIAA Journal*, 34(5):938–945, 1996. 1.1.2

[18] R.G. Deissler. An analysis of second-order slip flow and temperature-jump boundary conditions for rarefied gases. *International Journal of Heat and Mass Transfer*, 7(6):681–694, 1964. 4.1

[19] B. C. Eu. *Kinetic theory and irreversible thermodynamics*. J. Wiley, New York, 1992. 2.3.2

[20] B. C. Eu. Boltzmann entropy, relative entropy, and related quantities in thermodynamic space. *The Journal of Chemical Physics*, 102(18):7169–7179, 1995. 2.3.2

[21] B. C. Eu. Form of uncompensated heat giving rise to a pfaffian differential form in thermodynamic space. *Physical Review E*, 51(1):768–771, 1995. 2.3.2

[22] S. Gottlieb, C. W. Shu, and E. Tadmor. Strong stability-preserving high-order time discretization methods. *SIAM Review*, 43(1):89–112, 2001. 4.2.1

[23] Harold Grad. On the kinetic theory of rarefied gases. *Communications on Pure and Applied Mathematics*, 2(4):331–407, 1949. I, 1.1.2, 2.1, a, 2.2, 3.2, 3.3.1

[24] Harold Grad. Note on N-dimensional Hermite polynomials. *Communications on Pure and Applied Mathematics*, 2(4):325–330, 1949. 2.2

[25] Harold Grad. The profile of a steady plane shock wave. *Communications on Pure and Applied Mathematics*, 5(3):257–300, 1952. 1.1.2, 2.3.2, 4.2.5

[26] Nicolas G. Hadjiconstantinou. Comment on Cercignani's second-order slip coefficient. *Physics of Fluids*, 15(8):2352–2354, 2003. 4.1

[27] Amiram Harten, Peter D. Lax, and Bram Van Leer. On upstream differencing and Godunov-type schemes for hyperbolic conservations laws. *SIAM Review*, 25 (1):35–61, 1983. 4.2.4, 4.2.4

[28] Jeffrey Alan Hittinger. *Foundations for the Generalization of the Godunov Method to Hyperbolic Systems with Stiff Relaxation Source Terms*. PhD thesis, University of Michigan, 2000. URL http://aerospace.engin.umich.edu/cfd/publications.htm or http://proquest.umi.com.proxy.lib.umich.edu/pqdweb?did=727820211&Fmt=7&clientId=17822&RQT=309&VName=PQD (authentication may be required). I, 2.3.1

[29] Lowell H. Holway. Existence of kinetic theory solutions to the shock structure problem. *Physics of Fluids*, 7(6):911–913, 1964. 2.3.2

[30] Lowell H. Holway. New statistical models for kinetic theory: methods of construction. *Physics of Fluids*, 9(9):1658–1673, 1966. 2.1.2

[31] Y. T. Hsia and G. A. Domoto. An experimental investigation of molecular rarefaction effects in gas lubricated bearings at ultra-low clearances. *Journal of Lubrication Technology-Transactions of the Asme*, 105(1):120–130, 1983. 4.1

[32] George Karniadakis, Ali Beskok, and Narayan Aluru. *Microflows and Nanoflows*. Interdisciplinary Applied Mathematics. Springer, 2005. 3.4.1, 4.1, 4.1

[33] Earle H. Kennard. *Kinetic theory of gases, with an introduction to statistical mechanics*. International series in physics. McGraw-Hill Book Company, Inc., New York, first edition, 1938. 4.1

[34] Loc Khieu and Bram van Leer. Solid-boundary treatments for moment equations. In *20th AIAA Computational Fluid Dynamics Conference*. AIAA, 2011. 3.2

[35] Loc Khieu, Yoshifumi Suzuki, and Bram van Leer. An analysis of a space-time discontinuous-Galerkin method for moment equations and its solid-boundary treament. In *19th AIAA Computational Fluid Dynamics Conference*. AIAA, 2009. 3.2

[36] Mikhail N. Kogan. *Rarefied Gas Dynamics*. Plenum Press, New York, 1969. 2.1, 2.1.2, 2.1.3, 3.1.1, 3.1.1, 3.1.3, 3.1.3, 3.1.3, 3.1.4

[37] Randall J. LeVeque. *Finite Difference Methods for Ordinary and Partial Differential Equations*. Society for Industrial and Applied Mathematics, Philadelphia, PA, 2007. doi: DOI:10.1137/1.9780898717839. 4.2.1

[38] C. D. Levermore. Moment closure hierarchies for kinetic theories. *Journal of Statistical Physics*, 83(5-6):1021–1065, 1996. 2.1.2, 2.2.1

[39] H. W. Liepmann, R. Narasimha, and M. T. Chahine. Structure of a plane shock layer. *Physics of Fluids*, 5(11):1313–1324, 1962. 2.3.2

[40] J. Clerk Maxwell. On stresses in rarefied gases arising from inequalities of temperature. *Philosophical Transactions of the Royal Society of London*, 170:231–256, 1879. 3.1.1

[41] L. Mieussens. Discrete-velocity models and numerical schemes for the Boltzmann-BGK equation in plane and axisymmetric geometries. *Journal of Computational Physics*, 162(2):429–466, 2000. 4.3.3

[42] L. Mieussens. Discrete velocity model and implicit scheme for the BGK equation of rarefied gas dynamics. *Mathematical Models and Methods in Applied Sciences*, 10(8):1121–1149, 2000. 4.3.3

[43] H. M. Mott-Smith. The solution of the Boltzmann equation for a shock wave. *Physical Review*, 82(6):885–892, 1951. 2.3.2

[44] S. Nocilla. On the interaction between stream and body in free-molecular flow. In L. Talbot, editor, *Rarefied Gas Dynamics*, pages 169–208, New York, 1961. Academic Press. 3.1.4

[45] S. Nocilla. The surface re-emission law in free molecule flow. In J. A. Laurmann, editor, *Rarefied gas dynamics*, volume 1, pages 327–346, New York, 1963. Academic Press. 3.1.4

[46] Young Gie Ohr. Improvement of the Grad 13 moment method for strong shock waves. *Physics of Fluids*, 13(7):2105–2114, 2001. 2.3.2

[47] D. I. Pullin. Direct simulation methods for compressible inviscid ideal-gas flow. *Journal of Computational Physics*, 34(2):231–244, 1980. 4.2.4

[48] P. L. Roe. Approximate Riemann solvers, parameter vectors, and difference schemes. *Journal of Computational Physics*, 43(2):357–372, 1981. 4.2.4

[49] Tommaso Ruggeri. Breakdown of shock-wave-structure solutions. *Physical Review E*, 47(6):4135–4140, 1993. 2.3.2

[50] R. H. Sanders and Kevin H. Prendergast. The possible relation of the 3-kiloparsec arm to explosions in the galactic nucleus. *Astrophysical Journal*, 188:489–500, 1974. 4.2.4

[51] R. Schamberg. *The Fundamental Differential Equations and the Boundary Conditions for High Speed Slip-Flow, and Their Application to Several Specific Problems*. PhD thesis, 1947. 4.1

[52] B. Schmidt. Electron beam density measurements in shock waves in argon. *Journal of Fluid Mechanics*, 39:361–373, 1969. 2.3.2

[53] E. M. Shakhov. Generalization of the Krook kinetic relaxation equation. *Fluid Dynamics*, 3(5):95–96, 1968. 2.1.2

[54] Ching Shen. *Rarefied Gas Dynamics*. Heat and Mass Transfer. Springer, 1st edition, 2005. 3.1.3

[55] Chi-Wang Shu and Stanley Osher. Efficient implementation of essentially non-oscillatory shock-capturing schemes. *Journal of Computational Physics*, 77(2): 439–471, 1988. 4.2.1

[56] A. K. Sreekanth. Slip flow through long circular tubes. In Leon Trilling and Harold Y. Wachman, editors, *Rarefied gas dynamics*, volume 1, pages 667–680, New York, 1969. Academic Press. 4.1, 5.2

[57] H. Struchtrup and M. Torrilhon. Regularization of Grad's 13 moment equations: derivation and linear analysis. *Physics of Fluids*, 15(9):2668–2680, 2003. 2.3.2

[58] Henning Struchtrup. *Macroscopic Transport Equations for Rarefied Gas Flows: Approximation Methods in Kinetic Theory*. Interaction of Mechanics and Mathematics. Springer, 1st edition, 2005. 1.1.2, 2.1.2, c, 2.3.2, 2.3.2, 3.4.1

[59] Henning Struchtrup. Failures of the Burnett and Super-Burnett equations in steady state processes. *Continuum Mechanics and Thermodynamics*, 17(1):43–50, 2005. 1.1.3

[60] Yoshifumi Suzuki. *Discontinuous Galerkin Methods for Extended Hydrodynamics*. PhD thesis, The University of Michigan, 2008. URLs http://aerospace.engin.umich.edu/cfd/publications.htm or http://hdl.handle.net/2027.42/58411 (authentication may be required). I, 1.1.2, 4.2, 4.2.1

[61] Yoshifumi Suzuki and Bram Van Leer. Application of the 10-moment model to MEMS flows. 43rd AIAA Aerospace Sciences Meeting and Exhibit - Meeting Papers, pages 1087–1099. American Institute of Aeronautics and Astronautics Inc., Reston, VA 20191, United States, 2005. 1.1.2

[62] Yoshifumi Suzuki, Loc Khieu, and Bram van Leer. CFD by first order PDEs. *Continuum Mechanics and Thermodynamics*, 21(6):445–465, 2009. 3.2

[63] G. H. Tang, Y. L. He, and W. Q. Tao. Comparison of gas slip models with solutions of linearized Boltzmann equation and direct simulation of Monte Carlo method. *International Journal of Modern Physics C*, 18(2):203–216, 2007. 5.2

[64] M. Torrilhon and H. Struchtrup. Regularized 13-moment equations: shock structure calculations and comparison to Burnett models. *Journal of Fluid Mechanics*, 513:171–198, 2004. 2.1, 2.3.2, 2.3.2

[65] Bram Van Leer. Upwind and high-resolution methods for compressible flow: from donor cell to residual-distribution schemes. *Communications in Computational Physics*, 1(2):192–206, 2006. 4.2

[66] Walter G. Vincenti and Charles H. Kruger. *Introduction to Physical Gas Dynamics*. Krieger Pub Co, Malabar, Florida, 1965. 2.1, 2.1.2, 2.1.2, 2.1.2, 2.1.3

[67] W. Weiss. Continuous shock structure in extended thermodynamics. *Physical Review E*, 52(6):R5760–5763, 1995. 1.1.2, 2.3.2

[68] W. Weiss. Comments on "Existence of kinetic theory solutions to the shock structure problem" [phys. fluids 7, 911 (1964)]. *Physics of Fluids*, 8(6):1689–1690, 1996. 2.3.2

[69] Frank M. White. *Viscous Fluid Flow*. McGraw-Hill series in mechanical engineering. McGraw-Hill, New York, 2nd edition, 1991. 2.1.1, 2.1.1, 4.2.5